



UNIVERSITÀ DEGLI STUDI DI MESSINA  
DIPARTIMENTO DI SCIENZE MATEMATICHE E INFORMATICHE,  
SCIENZE FISICHE E SCIENZE DELLA TERRA  
DOTTORATO DI RICERCA IN FISICA  
XXXVII Ciclo

---

**Design and preliminary set-up of an experimental  
apparatus for continuous measurement of soil – gas  
pressure fluctuations in active seismogenic  
environments**

Settore Scientifico Disciplinare – SSD  
GEOS-04/A – GEOFISICA DELLA TERRA SOLIDA

Tesi di Dottorato di:  
**Dott. Sebastiano Ettore Spoto**

Supervisor:  
**Chiar.ma Prof.ssa Debora Presti**

Co – Supervisors:  
**Chiar.mo Prof. Francesco Parello**  
**Chiar.mo Dott. Salvatore Giammanco**

Coordinatrice  
**Chiar.ma Prof.ssa Vincenza Crupi**

**Anno Accademico 2023/2024**





**Design and preliminary set-up of an experimental  
apparatus for continuous measurement of soil – gas  
pressure fluctuations in active seismogenic  
environments**

Doctoral dissertation presented by

**Sebastiano Ettore Spoto**

*(Student ID n. 533190)*

In candidacy for the degree of Doctor of Philosophy in  
Physics at University of Messina

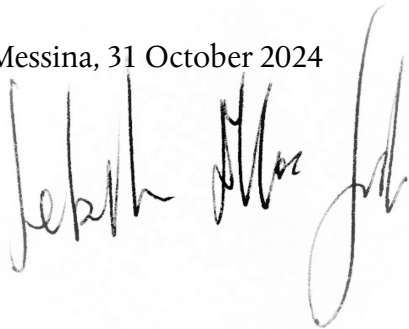
Messina, 31 October 2024



I hereby declare that this thesis is an original report of my research, has been written by me, and has not been submitted for any previous degree. The experimental work is almost entirely my own work; the collaborative contributions have been indicated clearly and acknowledged. Due references have been provided on all supporting literatures and resources.

I also hereby declare that I have no conflict of interest of any form pertaining to the proposed thesis.

Messina, 31 October 2024

A handwritten signature in black ink, appearing to read 'Jehann Mar J...', is written over a faint, circular watermark. The signature is fluid and cursive.

I respectfully dedicate this thesis to the cherished memory of my late father, Paolo Spoto, whose unwavering commitment to my education and intellectual development was exemplified through his remarkable sacrifices. His invaluable guidance has significantly contributed to the cultivation of my independent thoughts and ideas. I express my heartfelt gratitude for his enduring belief in my abilities.

Intellego ac tueor

## ACKNOWLEDGEMENTS

---

Here we are: time for gratitude.

I want to express my gratitude to several people who have supported me during my doctoral thesis. First and foremost, I would like to thank my doctoral thesis supervisor, Professor Debora Presti, of the “*Dipartimento di Scienze Matematiche e Informatiche, Scienze Fisiche e Scienze della Terra*” at the “*Università degli Studi di Messina*,” for supporting my thesis. Her patience, motivation, and suggestions have been invaluable to me.

I would like to express my special appreciation and thanks to my co-supervisor, Professor Francesco Parello, of the “*Dipartimento di Scienze della Terra e del Mare*” at the “*Università degli Studi di Palermo*.” He has been a tremendous mentor for me. I would like to thank him for encouraging my research and for allowing me to grow as a research scientist. His advices and guidance on both research and my career have been invaluable and instrumental.

I would also like to thank my co-supervisor, Dr. Salvatore Giammanco, of the National Institute of Geophysics and Volcanology (Etnean Observatory), for his supervision and tremendous suggestions.

I could not have wished for better supervisors for my doctoral thesis. If I have seen further, it is by standing on the shoulders of Giants.

My sincere thanks also go to Dr. Roberto Di Martino and Dr. Roberto Schifano. Without their precious support, this research would not have



been possible. Special thanks go to Prof. Barbara Orecchio for supporting my thesis and for her suggestions.

I want to acknowledge Prof. Vincenza Crupi for the precious time spent solving the administrative questions as coordinator of the PhD program in Physics.

I would like to thank the reviewers for their thoughtful comments and efforts towards improving my doctoral thesis.

I want to thank my family members and friends: Francesca, Amalia, Salvo, Lidia, Valentina, Gianluca, Simone, Vincenzo, Loredana, Eileen, Gianfranco, Mario, Roberta, and Federica. Thanks for the affection and laughs; they spiritually supported me throughout writing this thesis and my life in general. I thank them for their understanding of the time I have spent on this thesis, sometimes at the expense of time with them. I know I can count on them, even if they are far away, and time becomes a worse enemy while getting older.

Last but not least: I would like to thank my beloved dogs and cat: Poseidone Pixel, Pablo, Pékin Noir (aka Peppino), Penthésilée Sakura, Prometheus Jupiter, Penelope Al Frida Naonao, Psyche Sofia Elena Clio, Phoebe Urania Mafalda Artemide, Proto Pulsar Plutino Seth, and Devon Drake (the cat). I record my deep sense of gratitude to them for listening quietly to my complaints and offering their quiet companionship and occasional noisy distractions.

## ABSTRACT

---

A new experimental apparatus has been designed to measure pressure fluctuations in soil – gas movements. The experimental apparatus builds on existing theoretical solutions for analyzing spherical air flux in soil and allows for consistent measurement every 0.2 seconds. Using this method, tests to measure gas pressure fluctuations in both laboratory and field settings were conducted, showing a high sensitivity to even slight variations of pressure and micro-cycles. Data analyses suggests that this experimental apparatus significantly improves the capability to understand and comprehend degassing processes in seismogenic and volcanic environments, as well as the meteorological phenomena involved.

**Keywords:** soil – gas pressure fluctuations; Darcy’s Law, permeability, seismogenic environments, Mount Etna.

## LIST OF FIGURES

---

Figure 3.1 – Schematic illustration of the prototype apparatus used in the laboratory.	25
Figure 3.1 – Cross – section of capillary tubes.	26
Figure 3.3 – Data Logger.	27
Figure 3.4 – Cumulative grain size distribution curve.	34
Figure 3.5 – Schematic illustration of the field prototype apparatus.	36
Figure 4.1 – Diagram “ $\delta P$ vs $t$ ” at 0.1 l/min.	41
Figure 4.2 – Diagram “ $\delta P$ vs $t$ ” at 0.2 l/min.	42
Figure 4.3 – Diagram “ $\delta P$ vs $t$ ” at 0.3 l/min.	43
Figure 4.4 – Diagram “ $\delta P$ vs $t$ ” at 0.4 l/min.	44
Figure 4.5 – Diagram “ $\delta P$ vs $t$ ” at 0.5 l/min.	45
Figure 4.6 – Diagram “ $\delta P$ vs $t$ ” at 0.8 l/min.	46
Figure 4.7 – Diagram “ $\delta P$ vs $t$ ” at 1.0 l/min.	47
Figure 4.8 – Diagram “ $\delta P$ vs $t$ ” at 2.0 l/min.	48
Figure 4.9 – Diagram “ $\delta P$ vs $t$ ” at 5.0 l/min.	49
Figure 4.10 – Diagram “ $\delta P$ vs $t$ ” at 10.0 l/min.	50
Figure 4.11 – Diagram shows the time ( $t^{ss}_{120}$ , $t^{ss}_{75}$ , and their difference $dt^{ss}$ ) taken to reach the steady state against the air flux ( $\phi_{air}$ )	53
Figure 4.12 – Diagram “ $\delta P$ vs $\phi_{air}$ ”.	55
Figure 4.13 – Diagram “ $\Delta_{(120-75)}$ vs $\phi_{air}$ ”.	56

Figure 4.14 – Diagram “ $\delta P$ vs $t$ ” for the experiment related to the increase/decrease of the air flux ( $\phi_{\text{air}}$ ) in the system.	66
Figure 5.1 – Diagram $[\text{CO}_2]$ vs Depth at $t_0$ .	70
Figure 5.2 – Diagram $[\text{CO}_2]$ vs Depth at $t_1$ .	70
Figure 5.3 – Diagram $[\text{CO}_2]$ vs Depth at $t_2$ .	71
Figure 5.4 – Diagram $[\text{CO}_2]$ vs Depth at $t_3$ .	71
Figure 5.5 – Diagram $[\text{CO}_2]$ vs Depth at $t_4$ .	72
Figure 5.6 – Diagram $[\text{CO}_2]$ vs Depth at $t_5$ .	72
Figure 5.7 – Diagram $[\text{CO}_2]$ vs Depth at $t_6$ .	73
Figure 5.8 – Diagram $[\text{CO}_2]$ vs Depth at $t_7$ .	73
Figure 5.9 – Diagram $[\text{CO}_2]$ vs Depth at $t_8$ .	74
Figure 5.10 – Diagram $[\text{CO}_2]$ vs Depth at $t_9$ .	74
Figure 5.11 – Diagram $[\text{CO}_2]$ vs Depth at $t_{10}$ .	75
Figure 5.12 – Diagram $[\text{CO}_2]$ vs Depth at $t_{11}$ .	75
Figure 5.13 – Diagram $[\text{CO}_2]$ vs Depth at $t_{12}$ .	76
Figure 5.14 – Diagram $[\text{CO}_2]$ vs Depth at $t_{13}$ .	76
Figure 5.15 – Diagram $[\text{CO}_2]$ vs Depth at $t_{14}$ .	78
Figure 5.16 – Diagram $[\text{CO}_2]$ vs Depth at $t_{15}$ .	78
Figure 5.17 – Diagram “[ $\text{CO}_2$ ] vs $t$ ”.	80
Figure 5.18 – Double diagram $[\text{CO}_2]/[\text{He}]$ vs depth	80
Figure 5.18 – Diagram “ $\delta P$ vs $t$ ” relationships from $t_0$ to $t_{15}$	81
Figure 6.1 – FEA installation .	84
Figure 6.2 – Location of FEA on Mount Etna	84

Figure 6.3 – Field measurements conducted on August 30, 2024.	91
Figure 6.4 – Field measurements conducted on August 31, 2024.	93
Figure 6.5 – Field measurements conducted on September 2, 2024.	94
Figure 6.6 – Particular of the field measurements conducted on August 30, 2024.	96
Figure 7.1 – Connectors of the differential pressure sensors ( $\Delta$ 6F-PH0505AD3).	99
Figure 7.2 – Location of FEA on Mount Etna.	103
Figure 7.3 – Field measurements conducted on September 10, 2024.	105
Figure 7.4 – Field measurements conducted on September 10, 2024, time span 0-175 seconds.	108
Figure 7.5 – Field measurements conducted on September 10, 2024, time span 400-500 seconds.	109
Figure 7.6 – Field measurements conducted on September 10, 2024, time span 625-750 seconds.	111
Figure 7.7 – Field measurements conducted on September 10, 2024. The time series data includes $\Delta_{(70-25)}$ calculated a), and $\Delta_{(70-25)}$ measured.	113

## LIST OF TABLES

---

Table 3.1 – Grain – size parameters.	35
Table 4.1 – Values of the time ( $t^{ss}_{120}$ , $t^{ss}_{75}$ , and their difference $\delta t^{ss}$ ) taken to reach the steady state based on the different air fluxes (air) used.	51
Table 4.2 – Reynolds numbers obtained at different air fluxes ( $\phi_{air}$ ).	54
Table 4.3 – Outlet CO <sub>2</sub> fluxes ( $\phi_{CO_2}$ ) measured.	57
Table 4.4 – Values of the intrinsic permeability of the IEA.	63
Table 4.5 – Values of the intrinsic permeability of the FEA.	63
Table 5.1 – Concentration of CO <sub>2</sub> determined in spectroscopy.	68
Table 5.2 – Concentrations of CO <sub>2</sub> and He determined in gas chromatography.	79

## TABLE OF CONTENTS

---

Acknowledgements	i
Abstract	iii
List of Figures	iv
List of Tables	vii
Table of contents	viii
Chapter 1 – Introduction	1
Chapter 2 – Notes on the gas migration mechanisms	11
Chapter 3 – Experimental apparatus	24
Chapter 4 – Data analysis	38
Chapter 5 – Geochemical observations on data analysis	67
Chapter 6 – Field applications	83
Chapter 7 – Mitigating the effects of wind on the measurements of soil – gas pressure fluctuations	98
Chapter 8 – Conclusions	116
References	120

# CHAPTER 1

## INTRODUCTION

---

### Introduction

Prior to delving into the subject matter of this doctoral thesis, the purpose of this chapter is to furnish an introductory overview of the dissertation. The primary goal is to provide insight into the background and objectives of the research project, as well as to delineate the structure and methodology of the thesis.

Previous studies have conclusively demonstrated that substantial quantities of gases, comprising helium (He) (Sano *et al.*, 1998; Umeda, Asamori and Kusano, 2013; Buttitta *et al.*, 2020; Semenov, Lopatin and Chechelnitsky, 2020; Caracausi *et al.*, 2022), radon (Rn) (Hauksson and Goddard, 1981; Planinić, Radolić and Vuković, 2004; Ghosh, Deb and Sengupta, 2009; Ali Yallm *et al.*, 2012; Woith, 2015; Attanasio and Maravalle, 2016; Barkat *et al.*, 2017; Fu *et al.*, 2017; Iwata *et al.*, 2018; Kim *et al.*, 2018; Alam *et al.*, 2020; Haider *et al.*, 2021; Muto *et al.*, 2021; Vimercati *et al.*, 2021; Stylianos and Alexandra, 2023; Huang *et al.*, 2024), carbon dioxide (CO<sub>2</sub>) (G. Chiodini *et al.*, 2004; Frondini *et al.*, 2019; Chiodini *et al.*, 2020; Collignon *et al.*, 2021; Li Vigni *et al.*, 2022), methane (CH<sub>4</sub>) (Wang *et al.*, 2013, 2023; Geersen *et al.*, 2016; Meng and Zhang, 2021), hydrogen (H<sub>2</sub>) (Zgonnik, 2020; Zhang *et al.*, 2020; Zhong



*et al.*, 2021; Li *et al.*, 2023; Y. H. Jiang *et al.*, 2023), and carbon monoxide (CO) (Singh *et al.*, 2010; Cui *et al.*, 2024), are emitted from active fault zones prior to, during, and following major seismic events. These emissions have been documented through terrestrial field measurements and satellite-based remote sensing (Singh *et al.*, 2010). It is widely acknowledged that seismic activity has the potential to induce the release of soil gases sourced from a variety of origins, including volcanic, chemical, and biological processes (Conti, Picozza and Sotgiu, 2021; Freund *et al.*, 2021). Notably, volcanic gases are discharged from magma during its ascent to the Earth's surface due to pressure alleviation (Giammanco, Gurrieri and Valenza, 1999; Bruno *et al.*, 2001; Favara *et al.*, 2001; Giammanco *et al.*, 2010, 2013; Vaupotič, Žvab and Giammanco, 2010; Neri, Giammanco, *et al.*, 2011; Maucourant *et al.*, 2014; Neri *et al.*, 2016; Chicco, Giammanco and Mandrone, 2020; Terray *et al.*, 2020; Ristuccia, Bonfanti and Giammanco, 2021; Sortino *et al.*, 2022; Giammanco, Bonfanti and Neri, 2023) and are also liberated through geothermal and fault systems activated by seismic occurrences (Giammanco, Gurrieri and Valenza, 1997, 1999; Giovanni Chiodini *et al.*, 2004; Carapezza *et al.*, 2011; Neri, Giammanco, *et al.*, 2011; Allard *et al.*, 2014; Kyriakopoulos, 2017; Chen *et al.*, 2019; Neri, Giammanco and Leonardi, 2019; Gudjónsdóttir *et al.*, 2020; Inguaggiato *et al.*, 2023).

There is significant interest in the emission of various gases from the Earth associated with seismic activities, particularly earthquakes (Cicerone, Ebel and Britton, 2009). The variety of proposed models aimed at reconciling observed gas exhalations with physical mechanisms driven by seismicity can be classified as follows(Thomas, 1988): 1) emissions induced by ultrasonic vibrations; 2) alterations in solubility resulting from pressure changes; 3) pore collapses; 4) formation and development of new pores; and 5) subsurface fluid mixing.

In accordance with the vibrational model, gas releases may be induced or facilitated by ultrasonic vibrations of rocks. Although this mechanism has undergone testing in laboratory settings and during artificial explosions in seismic explorations, the power density of natural seismic spectra at high frequencies may not be adequate to fully elucidate the seismo-associated exhalations. Notably, releases induced by seismicity surpass those induced by explosions in intensity and can transpire subsequent to, rather than preceding, rupture events (Cicerone, Ebel and Britton, 2009).

It has been posited that gas emissions could be provoked by solubility variations resulting from an escalation of fluid pressure during the earthquake preparation phase. However, the efficacy of this mechanism is uncertain due to the considerable pressure increase

required to be transferred to the fluid phase (Cicerone, Ebel and Britton, 2009).

An alternative suggestion pertains to the collapse of pore volume due to an augmentation of stress in the incoming earthquake region, purported to induce gas release in groundwater (Cicerone, Ebel and Britton, 2009). While this phenomenon has been observed in selected laboratory tests, its credibility is undermined by the typical effect of high stress values on porous rocks, which tends to increase pore volume. Furthermore, the observed periodicity in gas release intensity does not align logically with the irreversible compression of pores (Cicerone, Ebel and Britton, 2009).

A more viable prospect involves the phenomenon of rock dilatancy, which has the potential to escalate rock porosity by significant percentages, thereby facilitating gas release from the rocks and augmenting the reaction ratio with groundwaters through the expansion of microscopic surfaces (Cicerone, Ebel and Britton, 2009). Nonetheless, discernible increases in pore volume have primarily been observed near the rock failure strength, implying that the purported mechanism may only be effective within the limited volume of the seismic fault undergoing the rupture process, whereas gas releases have been discerned at considerable distances from the epicenter (Cicerone, Ebel and Britton, 2009).

The observed exhalation phenomena are likely attributed to the occurrence of cracking resulting from corrosion and low-stress subsidence, compounded by elevated fluid content. It is postulated that a synergistic interplay of ground fluids and chemical constituents from distinct aquifer systems constitutes the most potent mechanism for inducing fluctuations, both positive and negative, in gas exhalation (Cicerone, Ebel and Britton, 2009). This supposition encompasses the discernible correlation with temperature fluctuations, occasionally concurrent with radon exhalations. Within this framework, the implicated mechanism could plausibly feature in the generation of low-frequency electromagnetic emissions through electrokinetic processes. All extant physical models positing to explicate gas exhalations share the premise that rapid and non-linear rock-related processes along seismic faults, encompassing deformation, fluctuations in fluid flow, and variances in pore volume, underlie the anomalous deviations in observed parameters (Cicerone, Ebel and Britton, 2009).

Gas migration associated with seismic events occurs within heterogeneous geological environments where spreading and mixing processes are commonplace. The system's complexity is primarily attributed to fractures, such as cracks, joints, and faults, which compromise the mechanical integrity of the Earth's materials, serving as high-speed conduits for fluid flow in the subsurface and modifying

permeability. Fractures seldom exist independently in the subsurface, as the deformation of brittle bodies often yields multiple breaks, giving rise to intricate multi-scale fracture and fault patterns that influence mechanical properties and fluid conduction in low-permeability media. Consequently, the processes of gas migration and displacement take place in fractured and porous media, subject to complex physical phenomena (Zimmerman and Paluszny, 2023).

The intensity of gas emissions varies significantly among different species, such as methane, argon, carbon monoxide, dioxide, and helium. Some gases, like hydrogen and chlorine, show increased levels, while others, including methane and nitrogen, show decreased levels before earthquakes (Conti, Picozza and Sotgiu, 2021). Currently, there is a lack of quantitative estimation of the correlation between anomalous gas releases and seismic events, as well as the temporal and spatial distance between them. More conclusive evidence is needed to ascertain the reliability of this hypothesis. While the comprehension of these processes holds potential for earthquake prediction, it is crucial to investigate them within the framework of essential geophysics and chemical physics, rather than attempting to anticipate future events (Conti, Picozza and Sotgiu, 2021).

The movement of gases towards the Earth's surface eludes conventional seismological detection. In contrast, geochemical

methodologies offer the capability to delineate the specific chemical constituents implicated in seismogenic processes. Nonetheless, this necessitates the utilization of costly and highly sensitive analytical instrumentations, protracted and expensive laboratory analysis procedures, and presents a restricted capacity to encompass large investigative domains in the immediate prelude and aftermath of seismic occurrences.

Based on the foregoing premises, this doctoral thesis aims to create a prototype aimed at achieving a level of data acquisition continuity akin to that found in seismology. Simultaneously, this system is intended to function as a complement to traditional geochemical surveillance methods, thereby enhancing the comprehension of gas migration mechanisms. Thus, the key challenges and fundamental issues related to gas migration were elucidated through the detection of gas propagation effects, independent of their chemical compositions. The central research inquiries in this thesis are:

- Is it feasible to develop and design a gas detection prototype that operates continuously and possesses data acquisition frequencies comparable to those utilized in the field of seismology?
- Is it feasible to develop a high-performing gas detection prototype utilizing cost-effective materials?

- Can a prototype be developed to provide instantaneous information on gas migration in comparison to conventional geochemical surveillance methods?

Limited research studies on the abovementioned inquiries are available in literature to date. Consequently, this thesis addresses the challenge of data scarcity by conducting multiple experimental stages to gain comprehensive insights into pressure fluctuations resulting from gas migration and the associated gas flux relationships. The primary objective of this doctoral thesis was to advance the current state of knowledge regarding data acquisition pertaining to gas propagation in active seismogenic environments. This was achieved through the development of a prototype using cost-effective components. It is plausible to assert that this apparatus could serve as the cornerstone of a monitoring network in regions currently lacking such infrastructure. Furthermore, upon deeper examination, this apparatus exhibits potential for application across various sectors of civil society.

The thesis is structured as follows:

**Chapter 2 – notes on the gas migration mechanisms** : This section presents essential concepts crucial for comprehending the research. It succinctly outlines the fundamental aspects of gas

migration processes, encompassing advection/diffusion and the Dusty Gas Model.

**Chapter 3 – experimental apparatus** : This chapter presents the description and rationale of the experimental prototype employed to simulate a natural degassing system in both indoor and outdoor experiments.

**Chapter 4 – data analysis** : This chapter formally addresses the main challenges of the thesis by detailing the results obtained in the method for measuring gas pressure fluctuations.

**Chapter 5 – geochemical observations on data analysis** : This section provides geochemical observations to assess the effectiveness of the method for measuring gas pressure fluctuations.

**Chapter 6 – field applications** : This chapter outlines the outcomes of utilizing the experimental prototype to measure gas pressure fluctuations in outdoor experiments.

**Chapter 7 – mitigating the effects of wind on the measurements of soil – gas pressure fluctuations** : This chapter outlines the outcomes of mitigating the effects of wind on the field measurements of soil – gas pressure fluctuations.



**Chapter 8 – conclusions:** This final chapter summarizes the thesis, draws conclusions, and offers potential ideas for extending the presented research work in the future.

## CHAPTER 2

### NOTES ON THE GAS MIGRATION MECHANISMS

---

#### Introduction

The main objective of this chapter is to offer a comprehensive overview of the theories developed to elucidate the intricate process of gas transport through porous media. This form of transport plays a crucial role in a wide range of Earth Sciences applications, including the monitoring of earthquakes (G. Chiodini *et al.*, 2004; Frondini *et al.*, 2019; Chiodini *et al.*, 2020), assessing gas-related hazards (Madonia *et al.*, 2022; Carapezza *et al.*, 2023; Di Martino and Gurrieri, 2023), conducting geochemical explorations of active faults (Sun *et al.*, 2021; Liu *et al.*, 2023; Zhang *et al.*, 2024), exploring hydrocarbon reserves (Zimmerman and Paluszny, 2023), identifying hydrocarbon-bearing reservoirs (Zimmerman and Paluszny, 2023), as well as the surveillance and monitoring of volcanic activities (Giammanco *et al.*, 2007; Viveiros *et al.*, 2008; Allard *et al.*, 2014; Cardellini *et al.*, 2017; Gurrieri *et al.*, 2023).

Gas transportation through porous media involves two main components: advective and diffusive (Ho and Webb, 2010). This chapter will start by examining each of these components separately, and then it will be delved into the combined mechanisms.

When studying gas-phase advection in porous media, Darcy's law is commonly relied upon. This law simply states that the gas Darcy velocity ( $u_g$ ) is directly proportional to the gas-phase pressure gradient ( $\nabla P_g$ ) and the gas-phase permeability ( $k_g$ ). Mathematically, Darcy's law can be expressed as (Ho and Webb, 2010):

$$\bar{u}_g = -\frac{k_g}{\mu_g} (\nabla P_g - \rho_g \bar{g})$$

where  $\mu_g$  is the gas-phase viscosity and  $\bar{g}$  is the gravitational constant.

In terms of mass flux, the equation is:

$$\bar{F}_g = \rho_g \bar{u}_g = -\frac{k_g}{\mu_g} \rho_g (\nabla P_g - \rho_g \bar{g})$$

Neglecting gravity and rearranging

$$\nabla P_g = -\frac{\mu_g}{k_g} \bar{u}_g$$

It is helpful to note that the Darcy velocity,  $u_g$ , is not a physical velocity. Instead, it is a superficial velocity based on the entire cross-section of the flow, not just the fluid flow cross-section. The Darcy velocity is related to the pore velocity,  $V_g$ , through the porosity,  $\phi$ , or

$$V_g = \frac{u_g}{\phi}$$

The gas-phase permeability, denoted as to  $k_g$ , represents a proportionality constant typically determined through

experimental methods utilizing units of length. It is noteworthy that the gas-phase permeability may exhibit slight variations when compared to the liquid-phase permeability due to fluid influence.

It is essential to note that Darcy's law is applicable to low-velocity flow, which commonly occurs in porous media flow, and to areas without boundary shear flow, such as those located away from walls. In cases where wall shear is significant, the Brinkman extension<sup>1</sup> can be applied. In numerous situations, inclusion of the boundary shear term is unnecessary. Its impact is only significant in a region near the boundary, with a thickness approximately equal to the square root of the gas permeability.

For turbulent flow conditions, the Forchheimer equation<sup>2</sup> is the

---

<sup>1</sup> The Brinkman extension to Darcy's law equation includes the effect of wall or boundary shear on the flow velocity, or

$$\nabla P_g = -\frac{\mu_g}{k_g} \bar{u}_g + \tilde{\mu} \nabla^2 \bar{u}_g$$

where gravity has been ignored for clarity. The first term on the right-hand side (RHS) is immediately recognizable as the Darcy expression, while the second term is a shear stress term such as would be required by a boundary wall no-slip condition (Ho and Webb, 2010). The coefficient  $\tilde{\mu}$  is an effective viscosity at the wall, which in general is not equal to the gas viscosity,  $\mu_g$ .

<sup>2</sup> At low pore velocities, Darcy's law works quite well. However, as the pore velocities increase, the flow becomes turbulent, the flow resistance becomes non-linear, and the Forchheimer equation is more appropriate. The Forchheimer equation is

$$\nabla P_g = -\frac{\mu_g}{k_g} \bar{u}_g - c_F k_g^{-1/2} \rho_g |\bar{u}_g| \bar{u}_g$$

most suitable approach.

Gas advection flow through porous media can be conceptualized as the passage of gas through numerous capillary tubes. For larger capillary tubes, the gas molecular mean free path is much smaller than the radius, resulting in continuum flow. As the capillary tubes diminish in size, the gas molecular mean free path reaches a comparable scale, leading to the significance of diffusion, particularly the free molecule or Knudsen diffusion (Bear, 1972; Ho and Webb, 2010). Knudsen's empirical investigation of low permeability effects on gas flow in capillaries revealed that the mass flux decreases as the average pressure is reduced according to Darcy's law. However, Knudsen discovered that at low pressures, the mass flux reaches a minimum and then increases with decreasing pressure due to slip, where the fluid velocity at the wall is not zero owing to free-molecule flow (Bear, 1972; Ho and Webb, 2010).

Diffusion in porous media encompasses continuum, or ordinary, diffusion and free-molecule diffusion. The former involves the relative motion of different gas species, while the latter, also

---

where  $c_f$  is a constant and gravity has been ignored. The first term on the RHS is again immediately recognizable as Darcy's law. The second term on the RHS is a non-linear flow resistance term (Ho and Webb, 2010).

known as Knudsen diffusion, occurs when the mean free path of gas molecules is of a similar order as the pore diameter of the porous media (Ho and Webb, 2010). As the pore size dwindles further, configurational diffusion is encountered, where the gas molecule size is comparable to the pore diameter (Ho and Webb, 2010). Numerous models have been employed to quantify gas diffusion processes in porous media. While some are adapted from clear fluid models, others are specifically developed for porous media applications, incorporating Molecular and Knudsen diffusion in their formulations (Ho and Webb, 2010).

Fick's law and the Stefan-Maxwell equation represent prominent approaches to calculating gas diffusion. Fick's law, although strictly applicable to clear fluids, has been widely extended to porous media by introducing a porous media factor for adaptability. The Stefan-Maxwell equation expands Fick's law for multicomponent mixtures. Despite attempts to define effective diffusion parameters accommodating the presence of porous media, the fundamental transport equations remain unaltered (Bear, 1972).

Fick's law comprises two principles: Fick's first law delineates the diffusive flux of a gas component in relation to the

concentration gradient under steady-state conditions, while Fick's second law pertains to the unsteady diffusive flux and the concentration gradient. These laws were originally conceived for clear fluids (Bear, 1972).

In the context of clear fluids, Fick's first law describes the relationship between mole or mass flux and the diffusion coefficient multiplied by the gradient of the mole or mass concentration within a binary system. Specifically, the mole flux formulation for component A in a one-dimensional clear fluid (without a porous medium) can be expressed as (Bear, 1972; Ho and Webb, 2010):

$$J_A^M = -cD_{AB,CF}\nabla\chi_A$$

where  $c$  denotes the concentration of the gas,  $D_{AB,CF}$ , represents the diffusion coefficient in a clear fluid, and  $\chi_A$  is the mole fraction of component A. It is imperative to note that the mole flux equation is relative to the molar-average velocity rather than stationary coordinates. Consequently, the mole flux equation relative to stationary coordinates for a binary system is defined as (Ho and Webb, 2010):

$$N_A^D - \chi_A(N_A^D - N_B^D) = -cD_{AB,CF}\nabla\chi_A$$

where  $N$  is relative to stationary coordinates. The second term on the left-hand side (LHS) is the molar-average velocity. The mass flux form relative to stationary coordinates is (Ho and Webb, 2010):

$$F_A - \omega_A(F_A - F_B) = -\rho_g D_{AB,CF} \nabla \omega_A$$

where  $F$  is the mass flux and  $\omega_A$  is the mass fraction of component A.

In the context of porous media, the application of Fick's first law often involves modification through the incorporation of a porous media factor,  $\beta$ , or

$$D_{AB}^* = \beta D_{AB,CF}$$

The term  $\beta$  is defined as

$$\beta = \phi S_g \tau$$

where  $D_{AB}^*$  denotes the effective diffusion coefficient for the AB gas system in a porous media,  $D_{AB,CF}$  denotes the effective diffusion coefficient of the AB gas system in a clear fluid,  $\phi$  is the porosity,  $S_g$  is the gas saturation, and  $\tau$  is the tortuosity. The tortuosity factor is discussed in further detail below. Similar to the clear fluid equation, the mole flux through a porous media relative to stationary coordinates is given by (Ho and Webb, 2010):

$$F_A - \omega_A(F_A - F_B) = -\beta \rho_g D_{AB,CF} \nabla \omega_A = -\rho_g D_{AB}^* \nabla \omega_A$$



Inclusion of the  $\beta$  term takes into account the effective area for gas flow in the pores ( $\phi S_g$ ) and the porous media tortuosity ( $\tau$ ). The diffusion coefficient  $D_{AB,CF}$ , can be estimated from correlations as discussed in literature (Bear, 1972; Ho and Webb, 2010).

The tortuosity factor, denoted as  $\tau$ , is defined within this application as the quotient of the length of the “tortuous” path in a porous medium divided by a direct linear distance. The evaluation of the tortuosity factor pertains to diffusion, excluding advection. For clear fluids, the tortuosity equals 1.0 (Ho and Webb, 2010).

The tortuosity correlation is given by (Ho and Webb, 2010):

$$\tau = \phi^{1/3} S_g^{7/3}$$

which can be rewritten as:

$$\tau = \tau_0 \tau_{S_g} = \phi^{1/3} S_g^{7/3}$$

where  $\tau_0$  denotes the tortuosity due to the structure of the porous medium and  $\tau_{S_g}$  denotes the tortuosity due to the partial saturation.

The definition and measurement of effective path length are often more intricate than they initially appear, which has resulted in the emergence of numerous tortuosity concepts over time (Holzer *et al.*, 2023). Different types of tortuosity can yield significantly different

values when applied to the same microstructure. However, these variations and the proliferation of concepts are frequently inadequately addressed in relevant academic papers and conference presentations (Holzer *et al.*, 2023). A contributing factor to this insufficient depiction of tortuosity is the absence of a suitable nomenclature for its various types. Moreover, many researchers in this domain may not fully comprehend the inherent differences among the various tortuosity types (Holzer *et al.*, 2023). This lack of awareness can lead to confusion in scientific discourse and result in misinterpretation of the acquired data. Consequently, the primary challenges in this field are to enhance awareness within the scientific community regarding the systematic differences between tortuosity types and to propose a coherent classification scheme and nomenclature. Such an initiative would facilitate more precise descriptions and promote clearer scientific discussions on the subject (Holzer *et al.*, 2023).

Fick's second law of diffusion pertains to the time-dependent change in concentration of clear fluids (Ho and Webb, 2010):

$$\frac{\delta c_A}{\delta t} = D_{AB} \nabla^2 c_A$$

This law is strictly applicable only under conditions where the molar average velocity is zero or in the case of equimolar counter

diffusion. Notably, this equation bears resemblance to the heat conduction equation.

Fick's first law of diffusion, as aforementioned, is specifically pertinent to binary gases owing to the direct correlation between the gradients of the two gases. Consequently, a singular gradient suffices for specification. Conversely, in the case of multicomponent gases, the determination of multiple gradients becomes requisite. In an ideal mixture, manipulation of the component mass flux equations yields the Stefan-Maxwell equation, suitable for stationary coordinates within a clear fluid (Ho and Webb, 2010).

$$\nabla x_i = \sum_{j=1}^n \frac{1}{cD_{ij}} (x_i N_j - x_j N_i)$$

Notably, in a two-component system, the Stefan-Maxwell equations converge to Fick's first law.

In the 1800s, Thomas Graham made significant discoveries regarding gas diffusion in porous media, elucidating crucial relationships that govern the diffusive fluxes of binary mixtures in a porous medium. Graham's law of effusion applies to Knudsen diffusion as experimentally discovered by Graham, or

$$-\frac{N_1^K}{N_2^K} = \left(\frac{m_2}{m_1}\right)^{1/2}$$

For ordinary diffusion (no advection), Graham's law of diffusion applies as experimentally discovered by Graham (1833) or

$$-\frac{N_1^D}{N_2^D} = \left(\frac{m_2}{m_1}\right)^{1/2}$$

Even though the ratios are identical (Ho and Webb, 2010), each equation applies to a different diffusion regime. In terms of a mass flux ratio, these equations become (Ho and Webb, 2010):

$$-\frac{F_1^K}{F_2^K} = \left(\frac{m_1}{m_2}\right)^{1/2}$$

$$-\frac{F_1^D}{F_2^D} = \left(\frac{m_1}{m_2}\right)^{1/2}$$

Notably, Graham's laws, after their initial elucidation, submerged into obscurity only to be independently resurrected in the 1950s and 1960s. They hold as fundamental relationships governing gas diffusion in porous media and significantly influenced the development of the Dusty Gas Model.

The interaction between advection and diffusion in porous media is of considerable significance. Consider two distinct volumes interconnected by a tube containing a light gas and a heavy gas. Due to the higher molecule velocity, the diffusion of the light gas surpasses that of the heavy gas. This differential diffusion results in a directional

flow of molecules towards the heavy gas volume, leading to an elevation in pressure within this volume and a subsequent decrease in pressure within the light gas volume. Consequently, the pressure differential induces advection from the heavy gas volume to the light gas volume. Evidently, diffusion plays a direct role in causing advection. It is noteworthy that only under conditions involving equimolar gases will diffusion not culminate in advection (Ho and Webb, 2010).

The coupling of advection and diffusion mechanisms has been rigorously formalized through the development of the Dusty Gas Model (DGM). The DGM represents an extension of the gas transport equations, incorporating the influence of porous media as a "dusty gas" component within the gas mixture. This "dusty gas" is postulated to comprise stationary large molecules that are considered a constituent of the gas mixture. The DGM applies the principles of kinetic theory to this dusty-gas mixture. A salient feature of the DGM is its amalgamation of diffusion (ordinary and Knudsen) and advection. The combination of ordinary and Knudsen diffusion involves the inclusion of momentum transfer based on kinetic-theory considerations (Ho and Webb, 2010).

Furthermore, diffusive fluxes (inclusive of ordinary and Knudsen components) are integrated with advective fluxes based on the

Chapman-Enskog kinetic theory. The DGM is presently the most widely utilized model for a mechanistic approach to integrating gas advection and diffusion in porous media. By disregarding thermal diffusion, typically negligible, the DGM can be formulated in relation to either the diffusive molar flux (ND) or the total molar flux (NT) with respect to fixed coordinates (Ho and Webb, 2010). These two expressions are:

$$\sum_{\substack{j=1 \\ j \neq i}}^n \frac{x_i N_j^D - x_j N_i^D}{D_{ij}^*} - \frac{N_i^D}{D_{ik}} = \frac{\nabla P_i}{RT} = \frac{P \nabla x_i}{RT} - \frac{x_i \nabla P}{RT}$$

$$\sum_{\substack{j=1 \\ j \neq i}}^n \frac{x_i N_j^T - x_j N_i^T}{D_{ij}^*} - \frac{N_i^T}{D_{ik}} = \frac{P \nabla x_i}{RT} + \left(1 + \frac{k_l P}{\mu D_{ik}}\right) \frac{x_i \nabla P}{RT}$$

where  $D_{ik}$  is the Knudsen diffusion coefficient. The second equation incorporates advective flux on both sides, with the first term on the left-hand side accounting for molecule-molecule interactions based on the Stefan – Maxwell equations. The second term on the LHS considers molecule-particle (Knudsen diffusion) interactions, while the right-hand side denotes the driving force for diffusion and advection, encompassing concentration and pressure gradients (Ho and Webb, 2010).

## CHAPTER 3

### EXPERIMENTAL APPARATUS

---

During the course of this doctoral research, an experimental apparatus was developed to simulate a natural degassing system. This apparatus was designed to facilitate tests involving the continuous measurement of soil-gas pressure fluctuations in simulated active seismogenic environments. The schematic diagram presented in Figure 3.1 illustrates the experimental apparatus, hereinafter referred to as "IEA – Indoor Experimental Apparatus".

The IEA is composed of a PVC cylinder with dimensions of 150 cm in height and 31.5 cm in internal diameter (*cross-section area of 0.078 m<sup>2</sup>*), containing ground basalt (192.00 Kg of ground basalt of different grain size has been used) filling up to a depth of 135 cm leaving a 15 cm empty chamber at the bottom, hereinafter referred to as “feed chamber”. This feed chamber is linked to the gas injection system, which will be described subsequently. The uppermost section of the IEA (*the level  $\emptyset$  in the experimental apparatus*) is intentionally left exposed to replicate natural outgassing conditions, while the lowermost part is hermetically sealed. A stainless-steel mesh wire

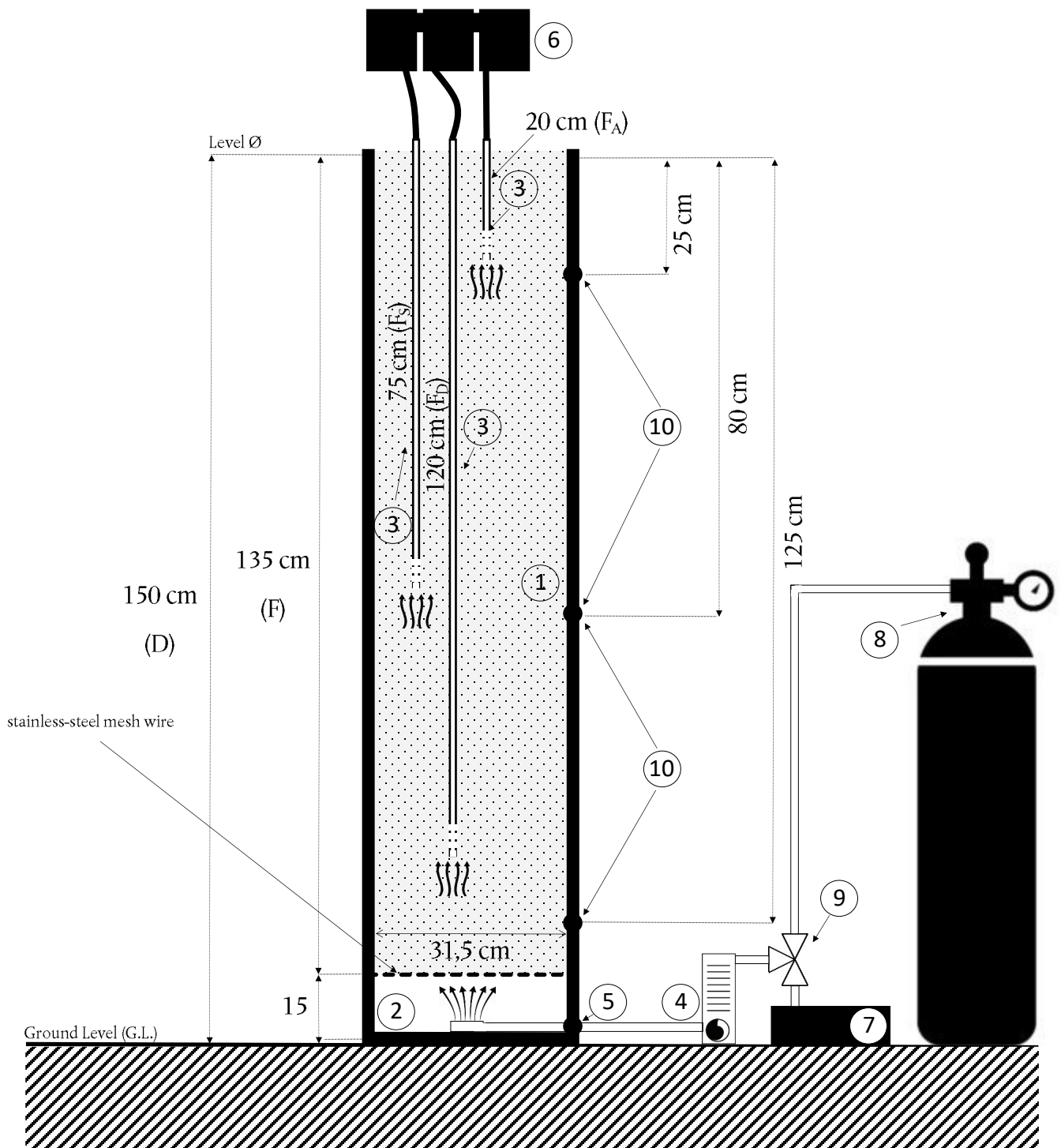


Figure 3.1 – Schematic illustration of the prototype apparatus used in the laboratory. This consists of: PVC cylinder ①, feed chamber ②, capillary tubes ③, fluxmeter ④, injection valve ⑤, data logger ⑥, air pump ⑦, gas tank ⑧, switch valve ⑨, sampling valves ⑩.



(Mesh 200) has been employed to separate the feed chamber of the cylinder from the section housing ground basalt. Three sampling valves were laterally installed on the PVC cylinder at depths of 25 cm, 80 cm, and 125 cm. Two straight copper capillary tubes, each with a length of 120 cm and 75 cm, were vertically inserted into the cylinder section housing ground basalt. Another straight copper capillary tube (length of 20 cm) is used as an auxiliary tube. The outer diameter of the tubes is 6.35 mm (1/4 inch) and the inner diameter is 4.75 mm (Figure 3.2). The lower ends of these capillary tubes are positioned at depths of 120 cm, 75 cm, and 20 cm (the auxiliary tube), respectively.

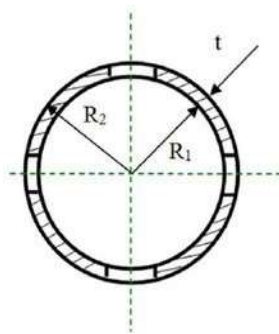


Figure 3.2 – Cross – section of capillary tubes. Outer radius ( $R_2$ ), internal radius ( $R_1$ ), thickness ( $t$ ).

Each of the capillary tubes are connected to a data logger (Figure 3.3) using silicone tubes. The data logger consists of:

- a compact, high – accuracy differential pressure sensor D6F-PH0505AD3 (Omron Electronics) with a differential pressure range of  $\pm 50$  Pa. with an absolute accuracy of  $\pm 0.01$  Pa.

- an interface BME280 (Bosch) Temperature, Humidity and Pressure Sensor. It measures relative humidity, temperature, barometric pressure. Temperatures ranging from  $-40^{\circ}\text{C}$  to  $85^{\circ}\text{C}$ . Over the temperature range of 0 to  $65^{\circ}\text{C}$ , the accuracy is  $\pm 1.0^{\circ}\text{C}$ ; outside of that range, the accuracy drops to  $\pm 1.5^{\circ}\text{C}$ . Relative humidity over a range of 0 to 100% with an accuracy of  $\pm 3\%$ . Barometric pressure ranging between 300 Pa to 1100 hPa with an absolute accuracy of  $\pm 0.1$  hPa.



Figure 3.3 – Data Logger.

- A D1 mini (WeMos) wireless 802.11 (Wifi) microcontroller development board. It is developed around the very popular ESP8266 wireless microcontroller.

Silicone tubes connect the capillary tubes to the differential pressure sensors D6F-PH0505AD3, resulting in a recording of any

pressure change. The difference between the gas pressure in the "IEA" and the barometric pressure (denoted as " $\delta P$ ") is continuously calculated at depths of 120 cm ( $\delta P_{120}$ ) and 75 cm ( $\delta P_{75}$ ) to obtain the corresponding differential pressure. The system configuration allows for a constant sampling frequency of 0.2 seconds.

A switch valve controls the injection system of the "IEA". This valve is used to choose the type of gas source that is injected. The gas can come from either (i) a tank containing a gas mixture with a specific concentration, regulated by a two-stage high-pressure gas regulator, or (ii) an air pump (Resun<sup>®</sup>, model ACO – 001) with a maximum output flow of 25 l/min. The gas enters the feed chamber of the "IEA" through an injection valve connected to the injection system by a silicone tube. A flowmeter is installed before the gas reaches the injection valve to control the gas inflow. Four different air flowmeters (purchased from Key Instruments) have been used for this research: 0.1 – 0.5 l/min; 0.1 – 1.0 l/min; 0.5 – 5.0 l/min; 1.0 – 10.0 l/min.

To accomplish the objectives of this doctoral research, each individual component comprising "IEA" was procured from readily available market products at remarkably low costs. For instance, copper capillary tubes were sourced from air conditioning systems used in residential constructions. The PVC cylinder was procured from

materials commonly utilized for conveying wastewater. Valves and assorted components were sourced from plumbing fixtures.

The investigation of gas flow in the unsaturated zone is a crucial research area that spans multiple disciplines, as previously discussed. In this context, the atmospheric pressure at the ground surface and the water table sets the upper and lower boundary conditions for gas flow phenomena. Typically, these boundary conditions are assumed to be constant and independent of time for easier mathematical analysis. (Baehr and Hult, 1991; Baehr and Joss, 1995; Falta, 1996; You and Zhan, 2012).

Gas movement in the unsaturated zone is affected by changes in atmospheric pressure at the ground surface and fluctuations in the water table, particularly in coastal regions where daily tides can result in significant water table variations (You and Zhan, 2012).

In general, atmospheric pressure fluctuations can be categorized into two distinct types (Neeper, 2003). The first type encompasses diurnal changes, which result from the heating and cooling effects induced by solar and terrestrial influences. The sinusoidal function is a prevalent mathematical representation for modeling this type of diurnal atmospheric pressure fluctuation (Neeper, 2003). The second type involves the sporadic passage of cold or warm fronts, capable of generating atmospheric pressure variations of up to 20–30 mbar within

a 24-hour period (Massmann and Farrier, 1992). In scholarly works, this form of atmospheric pressure fluctuation is at times characterized by a first-order linear function (Massmann and Farrier, 1992; You and Zhan, 2012).

The fluctuation of the water table is subject to influence from a multitude of factors, encompassing seasonal changes in precipitation, melt-freeze dynamics, evapotranspiration, cyclic pumping of nearby wells, alterations in stream stage, seismic activity, land use, climate variations, and oceanic tides (Turk, 1975; You and Zhan, 2012). Elevated temperatures lead to reduced surface tension and increased air volume within capillary pores, causing water to descend to the phreatic surface, resulting in a rise in the water level, and vice versa. This effect exhibits a time lag dependent on the depth of the water table. Furthermore, diurnal barometric cycles induced by solar heating and cooling can prompt the expansion or contraction of air volume within the capillary fringe, consequently causing fluctuations in water levels in shallow aquifers (You and Zhan, 2012). Additionally, water levels are found to fluctuate in response to plant water usage, which is regulated on a daily basis by global irradiance and seasonally by both global irradiance and temperature. However, if the primary source of plant water is the unsaturated zone, water table fluctuation will be significantly reduced. In non-coastal locations, water levels may not fluctuate in a given

aquifer setting (e.g., a deep-water table), and any fluctuations are typically limited to a few centimeters in amplitude. However, in coastal areas, water table fluctuations occur regularly due to diurnal and semi-diurnal tidal effects.

The influence of atmospheric pressure and water table fluctuations on subsurface gas pressure change and mass transport is generally insubstantial in comparison to that induced by well extraction or injection (You and Zhan, 2012). However, it is crucial to note that pressure fluctuation can significantly augment the rate of vapor-phase contaminant transport in fractured media and serves as a vital driving force for removing vapor-phase contaminants from the unsaturated zone without requiring active pumping, particularly in the context of passive soil vapor extraction. Notably, the high-frequency and often high-amplitude water table fluctuation in coastal areas play an influential role in gas flow in the unsaturated zone and can result in dome-shaped heave features. Furthermore, the amplification of the magnitude and frequency of water table fluctuations non-linearly increases the advective flux of volatile organic compounds (VOCs) in the subsurface (Choi and Smith, 2005).

Some aspects mentioned above were carefully considered when developing the experimental apparatus. Employing a cylinder containing a material of known permeability under anhydrous

conditions tries to solve the issues associated with vertical and lateral permeability variations. These variations significantly impact gas transport mechanisms and are often unaccounted for soil – gas measurements. Moreover, isolating the cylinder from the surrounding soil mitigates potential problems concerning water percolation. Additionally, continuous monitoring of barometric pressure is considered in the experimental apparatus. The measurements obtained by the differential pressure sensor ( $\delta P$ ) are “normalized” to the barometric pressure.

It is also pertinent to delineate the theoretical assumptions that the system must adhere to:

- 1) The air behavior shall follow the ideal gas law:

$$PV = nRT \text{ [eq.3.1]}$$

where  $P$  is the barometric pressure ( $Pa$ );  $V$  is the volume of air ( $m^3$ );  $n$  is the mole of air ( $mol$ );  $R$  is the ideal gas constant ( $8.314 J K^{-1} mol^{-1}$ ); and  $T$  is the temperature of air ( $K$ ).  $n$  is determined as follows:

$$n = \frac{m_{air}}{M_{air}} \text{ [eq.3.2]}$$

where  $m_{air}$  is the air mass ( $kg$ ); and  $M_{air}$  is the molar mass of air ( $0.029 kg/mol$ ). Accordingly, the air density can be determined by substituting [eq. 3.2] into [eq. 3.1]:

$$\rho_{air} = \frac{P}{R_{air}T}$$

where  $\rho_{air}$  is the air density ( $kg/m^3$ ); and  $R_{air}$  is a constant of 287  $J K^{-1} kg^{-1}$ .

2. The air flux is isothermal.
3. The air flux is laminar. Hence, Darcy's law can be applied to describe the air flux in the "IEA".
4. The "IEA" system shall be in anhydrous condition.
5. The permeability of the "IEA" system shall be precisely defined and remain consistent over time.
6. The ground basalt used to fill the "IEA" shall be considered isotropic and shall have a uniform distribution of particle sizes. The material used to fill the "IEA" comprises clasts of grounded volcanic rock with a diameter smaller than 3 mm. This material underwent appropriate treatment and was dried in an oven until it attained a consistent weight. Subsequently, the material was homogenized using quarter technique to procure a representative sample. The obtained sample was then subjected to particle – size analysis (the same procedure was used to fill the "IEA") through dry sieving, employing a set of 7 certified ASTM (American Society for Testing Materials) series sieves (4,00 mm, 2,00 mm, 1,00 mm, 0,500 mm, 0,250 mm, 0,125 mm, 0,063 mm).



The standard procedures utilized for the particle – size analysis are the following: UNI EN ISO 17892-4:2017, ASTM D421-85(2007), ASTM D 422—63 (2007), ASTM D1140-71, ASTM D 2217-85. Particle – size analysis was conducted using mechanical sieving (Retsch Vibratory Sieve Shaker AS 200 control) in dry sieving techniques. The retained material on each sieve was weighed using an analytical balance. Though data processing it was possible to determinate the cumulative grain size distribution curve (and cumulative frequency curve) (Figure 3.4). Statistical parameters were derived from the cumulative grain size distribution curve by graphically estimating percentiles.

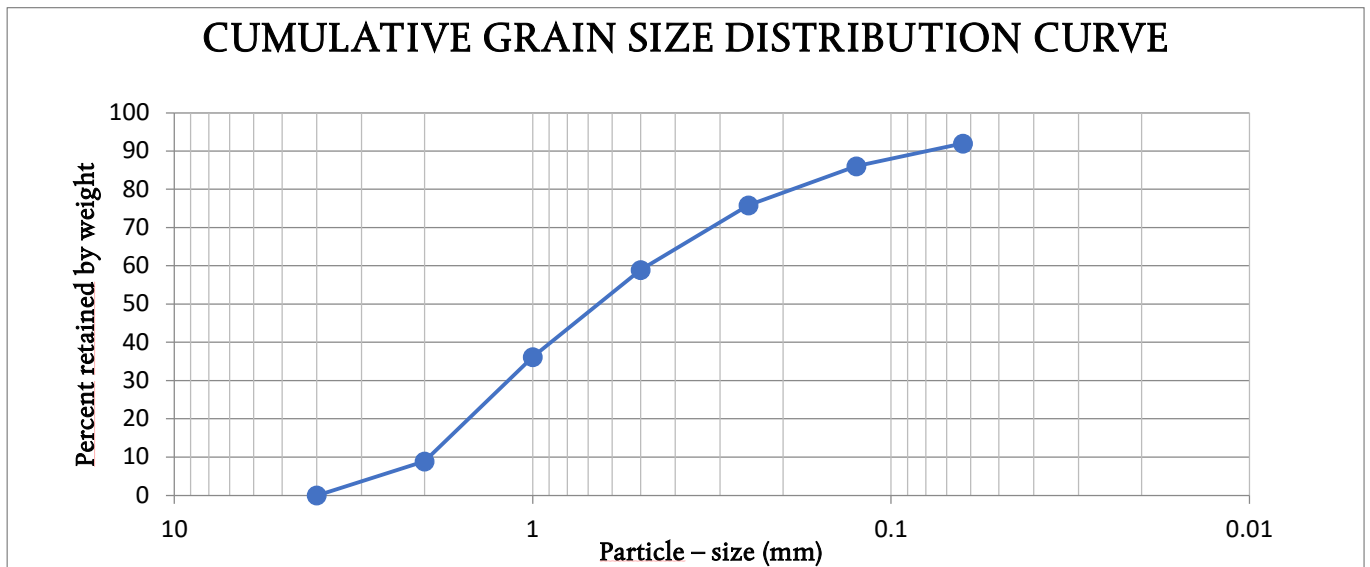


Figure 3.4 – Cumulative grain size distribution curve.

These percentiles denote the dimensions corresponding to seven percentage values (5 %, 16 %, 25 %, 50 %, 75 %, 84 %, 95 %) on the

cumulative grain size distribution curve. They effectively summarize, with a degree of approximation, the granulometric distribution of the sediment. Though the analysis of the percentiles the statistical parameters in Table 3.1 were calculated.

Parameter	Result	Note
D50	0.7 mm	
Kurtosis (K)	1 (mesokurtic)	$K = \frac{\varphi_{95} - \varphi_{05}}{2.44(\varphi_{75} - \varphi_{25})}$
Skewness (S <sub>k</sub> )	0.3 (positive skewed)	$S_k = \frac{\varphi_{84} + \varphi_{16} - 2\varphi_{50}}{2(\varphi_{84} - \varphi_{16})} + \frac{\varphi_{05} + \varphi_{95} - 2\varphi_{50}}{2(\varphi_{95} - \varphi_{05})}$
Classification	Muddy Sand	

Table 3.1 – Grain – size parameters.

To identify potential transport of heavy gases and to verify the safety of the work environment, measurements of radon activity concentration in the grounded basalt were performed using a DurrIDGE RAD7 radon meter (<http://www.durrIDGE.com/>). The RAD7 measures concentrations of both <sup>222</sup>Rn (radon) and <sup>220</sup>Rn (thoron) by exclusively collecting radon and then counting the alphas emitted by the decay of their respective daughter nuclides <sup>218</sup>Po (t<sup>1/2</sup> = 3.04 min) and <sup>216</sup>Po (t<sup>1/2</sup> = 0.145 sec). The values of radon levels are almost negligible due to their falling below the instrumental detection limits.

Following a series of laboratory experiments (see chapters 4 and 5), an experimental apparatus for conducting field measurements was designed. The schematic diagram presented in Figure 3.5 illustrates the experimental apparatus for field experimental measurements, referred

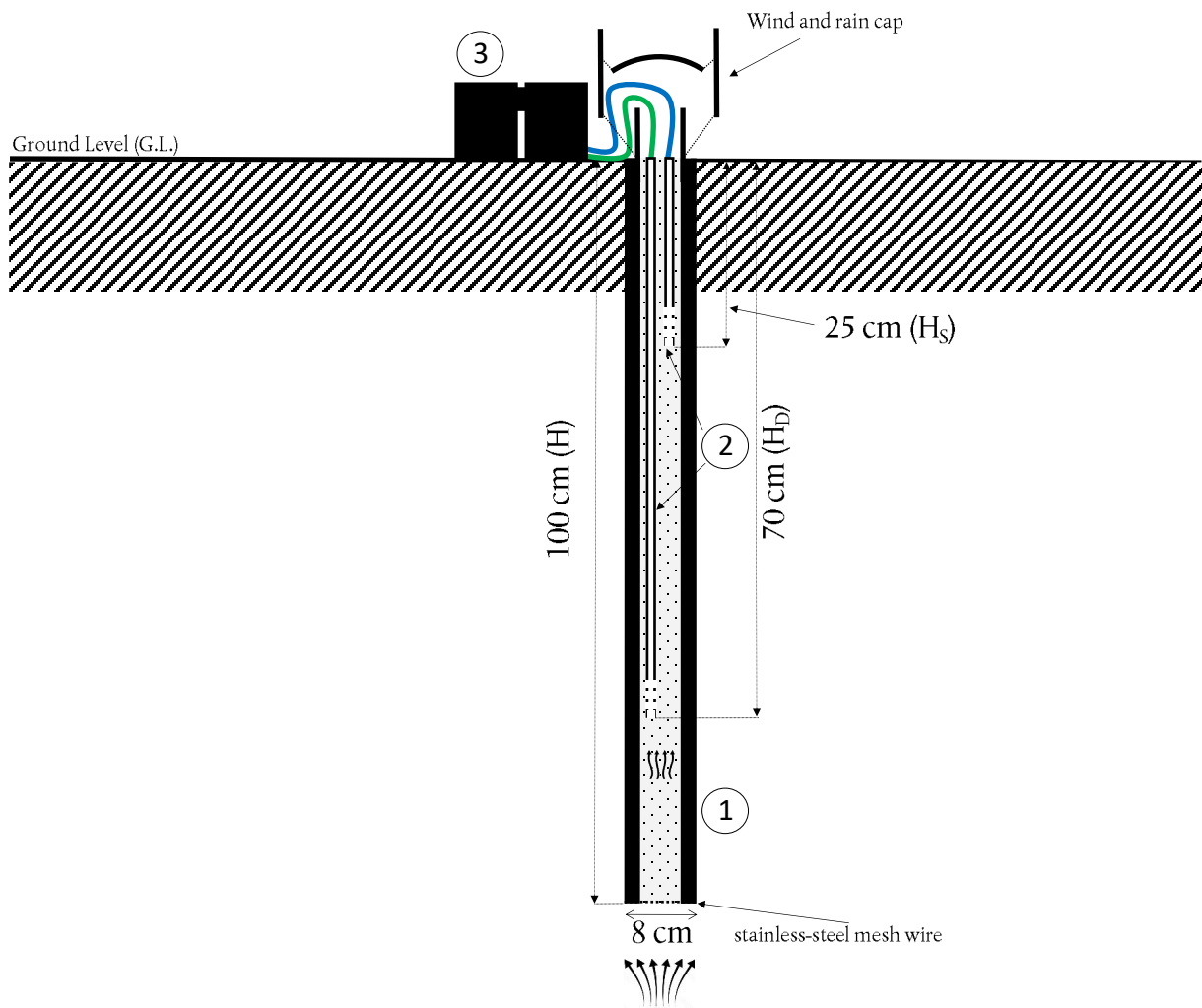


Figure 3.5 – Schematic illustration of the field prototype apparatus. This consists of: stainless-steel cylinder ①, capillary tubes ②, data logger s ③.

to as "FEA – Field Experimental Apparatus". This apparatus is composed of a stainless-steel cylinder with dimensions of 100 cm in height and 8 cm in internal diameter (*cross-section area of 0.005 m<sup>2</sup>*), containing the same ground basalt utilized in the "IEA". The stainless-steel cylinder is entirely filled up. The uppermost section of the "FEA" (*the level  $\emptyset$  in the field experimental apparatus*) is left exposed, while the lowermost part is closed with a stainless-steel mesh wire (Mesh 200). Two straight copper capillary tubes, each with a length of 70 cm and 25 cm, were vertically inserted into the cylinder section housing ground basalt. The outer diameter of the tubes is 6.35 mm (1/4 inch) and the inner diameter is 4.75 mm (Figure 3.2). The lower ends of these capillary tubes are positioned at depths of 70 cm, and 25 cm respectively. Each of the capillary tubes are connected to a data logger using silicone tubes. The data logger is the same as that utilized in the "IEA".

## CHAPTER 4

### DATA ANALYSIS

---

In order to examine the behavior of the indoor experimental apparatus “IEA” in line with the objectives of this doctoral thesis, the verification of the IEA's operational status under the application of gas fluxes was conducted.

To simulate a real soil gas regimen, air was pumped into the feed chamber at a constant and known air flux ( $\phi_{air}$ ). The range of explored air fluxes was as follows: 0.1 l/min, 0.2 l/min, 0.3 l/min, 0.4 l/min, 0.5 l/min, 0.8 l/min, 1.0 l/min, 2.0 l/min, 5.0 l/min, and 10.0 l/min. The imposed fluxes are within the range of CO<sub>2</sub> fluxes normally encountered in active volcanic and seismogenic areas (Chiodini *et al.*, 1998; Giammanco, Gurrieri and Valenza, 1998; Gerlach *et al.*, 2001; Finizola *et al.*, 2002; M. Camarda, Gurrieri and Valenza, 2006; Sergio Calabrese *et al.*, 2021b, 2021a).

During the conducted tests, monitoring of pressure fluctuation values, consistently recorded at a sampling frequency of 0.2 seconds, was facilitated using the differential pressure sensors, resulting in the acquisition of the following parameters:

- $\delta P_{120}$ : denotes the differential pressure ( $P_{120} - P_{\text{atm}}$ ) between the pressure recorded at a depth of 120 cm ( $P_{120}$ ) and the barometric pressure ( $P_{\text{atm}}$ ).
- $\delta P_{75}$ : denotes the differential pressure ( $P_{75} - P_{\text{atm}}$ ) between the pressure recorded at a depth of 75 cm ( $P_{75}$ ) and the barometric pressure ( $P_{\text{atm}}$ ).

Concurrently, the BME280 sensors continuously record the values of temperature and barometric pressure. The measurements captured by the various sensors are taken synchronously.

Through the process of data analysis, the parameter  $\Delta_{(120-75)}$  is determined as the difference between the measured values of  $\delta P_{120}$  and  $\delta P_{75}$ :

$$\Delta_{(120-75)} = \delta P_{120} - \delta P_{75}$$

All data pertaining to the investigated air fluxes in the IEA can be found in Zenodo open repository (DOI: 10.5281/zenodo.14016285).

Figures 4.1 to 4.10 show the diagrams “ $\delta P$  vs  $t$ ” and “ $\Delta_{(120-75)}$  vs  $t$ ”. The diagrams illustrate a consistent pattern where both  $\delta P_{120}$  and  $\delta P_{75}$  initially exhibit a transient phase, characterized by an increasing trend over time. Subsequently, a second phase is observed, wherein both  $\delta P_{120}$  and  $\delta P_{75}$  maintain a constant value as time progresses. This indicates that the system has reached a steady state.

The IEA records zero values across all differential pressure sensors when the air pump is in the off state. In the diagrams presented in Figures 4.1 to 4.10, the coordinate point (0, 0) signifies the activation of the air pump.

Upon careful examination of Figures 4.1 to 4.10, it is important to elucidate how the parameters (e.g.,  $\delta P_{120}$ ,  $\delta P_{75}$ , and  $\Delta_{(120-75)}$ ) sampled at 100-second can effectively represent the characteristics of the steady-state system.

In all the experiments presented in this doctoral thesis, it is clear that the differential pressure sensors have a reaction time of less than one second. This demonstrates the high sensitivity of the differential pressure sensors. Table 4.1 shows the values of the time ( $t^{ss}_{120}$ ,  $t^{ss}_{75}$ , and their difference  $\delta t^{ss}$ ) taken to reach the steady state based on the different air fluxes ( $\phi_{air}$ ) used.

The diagrams depicted in Figure 4.11 illustrate the relationship between  $t^{ss}_{120}$ ,  $t^{ss}_{75}$ , and  $\delta t^{ss}$  with respect to air flux ( $\phi_{air}$ ). It is noteworthy that the performance characteristics at air flux of 5.0 l/min and 10.0 l/min exhibit a distinct trend compared to lower air fluxes ( $\phi_{air}$ ).

The different path between air fluxes ( $\phi_{air}$ ) of 5.0 l/min and 10.0 l/min, compared to lower air fluxes ( $\phi_{air}$ ), may be ascribed to the presence of turbulence within the air flux.

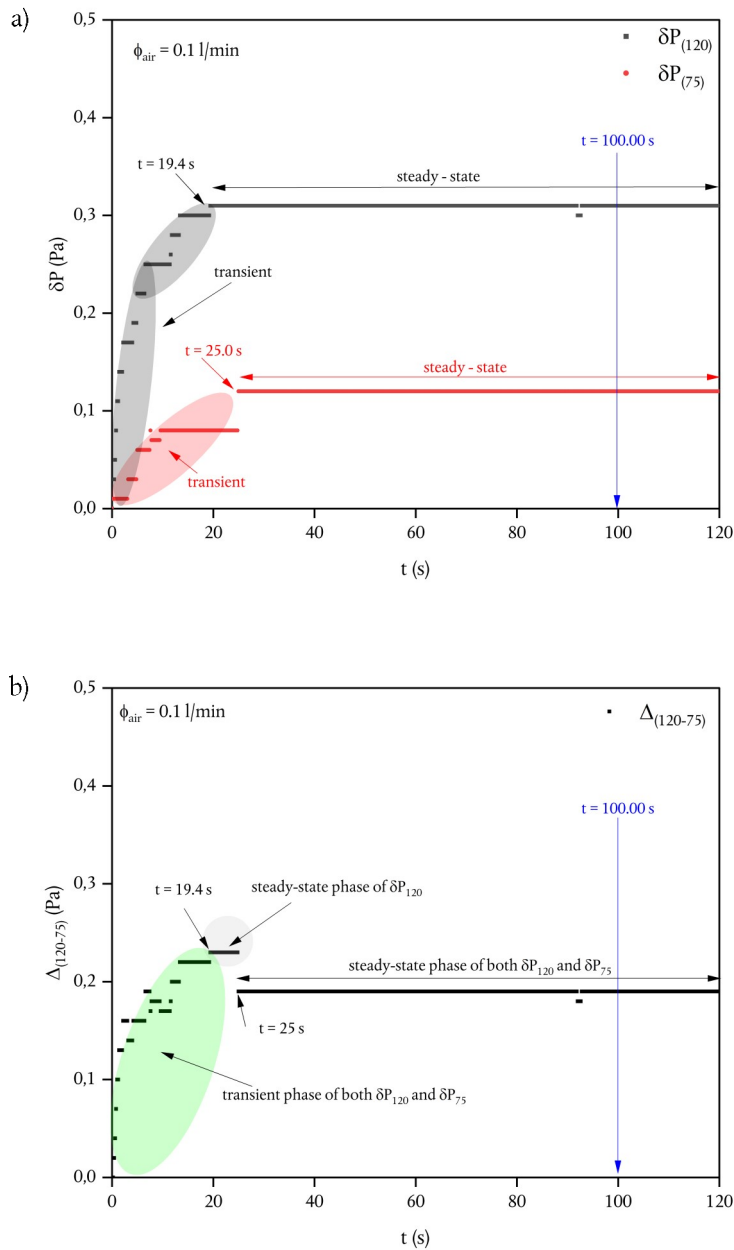


**Figure 4.1**— Diagram “ $\delta P$  vs  $t$ ” a). The grey-colored area signifies the transient state of the air flux at a depth of 120 cm. The red-colored area signifies the transient state of the air flux at a depth of 75 cm. Diagram “ $\Delta_{(120-75)}$  vs  $t$ ” b). The green-colored area represents the transient state of air flux for both depths. - The grey-colored area represents the air flux that reached a steady state at a depth of 120 cm but is still in a transient state at the depth of 75 cm. The air flux utilized for this diagram was 0.1 l/min. For a detailed explanation, please refer to the accompanying text.



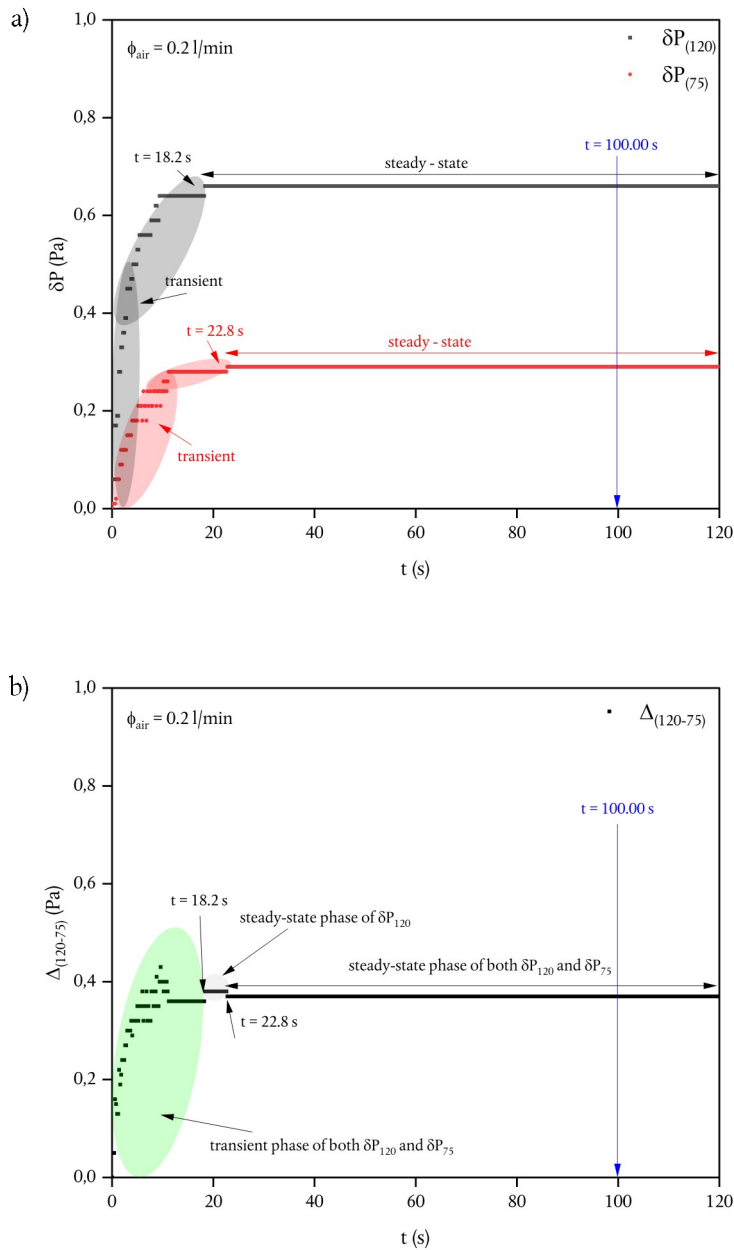


**Figure 4.2**— Diagram “ $\delta P$  vs  $t$ ” a). The grey-colored area signifies the transient state of the air flux at a depth of 120 cm. The red-colored area signifies the transient state of the air flux at a depth of 75 cm. Diagram “ $\Delta_{(120-75)}$  vs  $t$ ” b). The green-colored area represents the transient state of air flux for both depths. - The grey-colored area represents the air flux that reached a steady state at a depth of 120 cm but is still in a transient state at the depth of 75 cm. The air flux utilized for this diagram was 0.2 l/min. For a detailed explanation, please refer to the accompanying text.

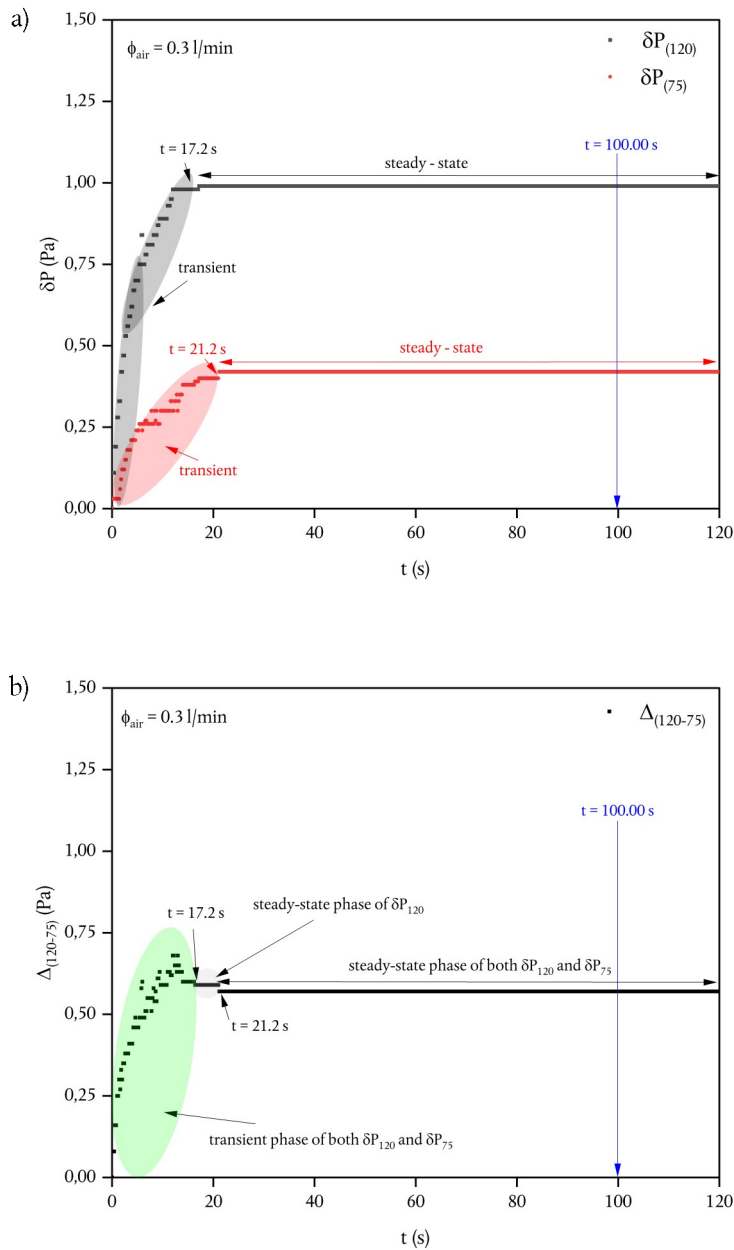


**Figure 4.3**— Diagram “ $\delta P$  vs  $t$ ” a). The grey-colored area signifies the transient state of the air flux at a depth of 120 cm. The red-colored area signifies the transient state of the air flux at a depth of 75 cm. Diagram “ $\Delta_{(120-75)}$  vs  $t$ ” b). The green-colored area represents the transient state of air flux for both depths. - The grey-colored area represents the air flux that reached a steady state at a depth of 120 cm but is still in a transient state at the depth of 75 cm. The air flux utilized for this diagram was 0.3 l/min. For a detailed explanation, please refer to the accompanying text.

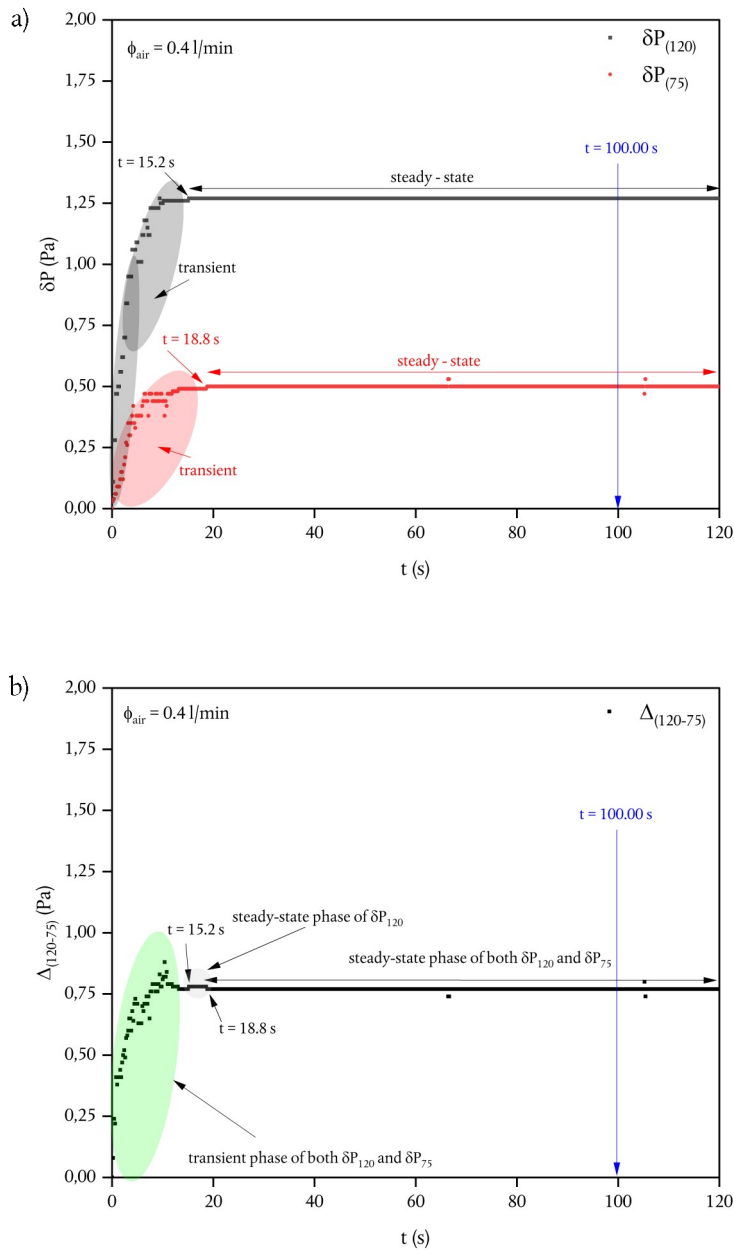


**Figure 4.4**— Diagram “ $\delta P$  vs  $t$ ” a). The grey-colored area signifies the transient state of the air flux at a depth of 120 cm. The red-colored area signifies the transient state of the air flux at a depth of 75 cm. Diagram “ $\Delta_{(120-75)}$  vs  $t$ ” b). The green-colored area represents the transient state of air flux for both depths. - The grey-colored area represents the air flux that reached a steady state at a depth of 120 cm but is still in a transient state at the depth of 75 cm. The air flux utilized for this diagram was 0.4 l/min. For a detailed explanation, please refer to the accompanying text.

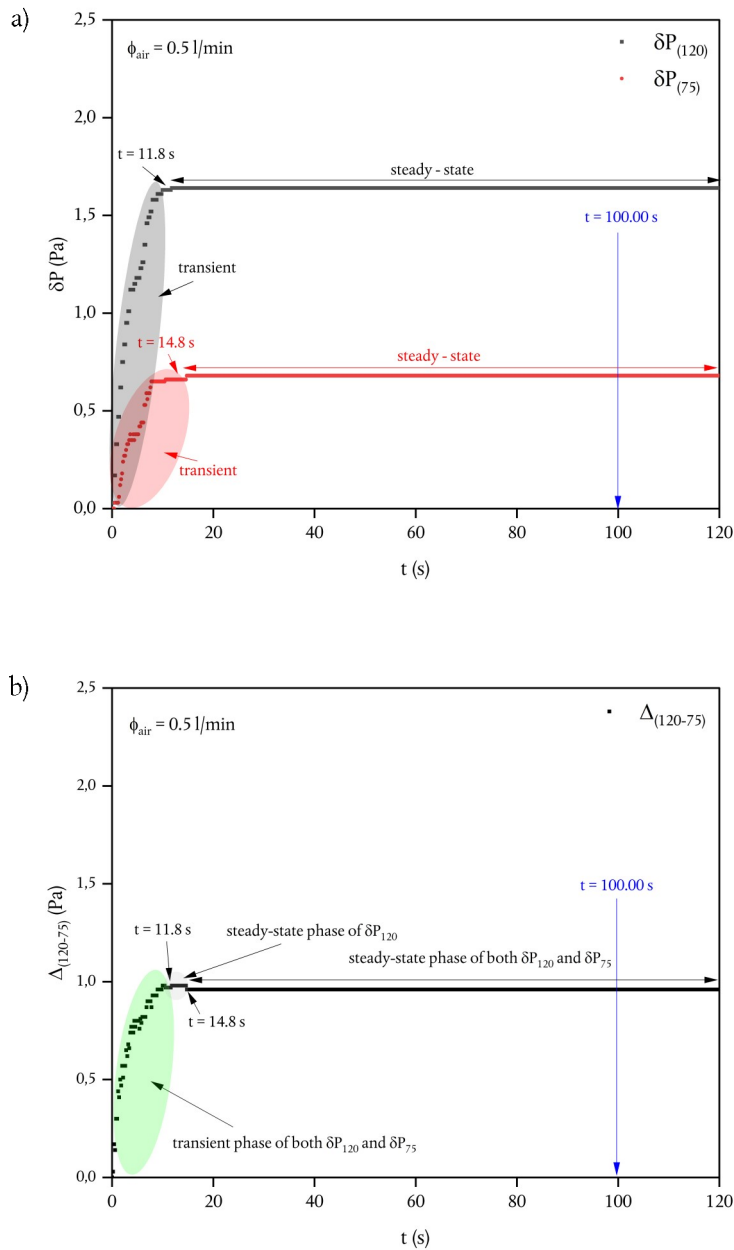


**Figure 4.5**— Diagram “ $\delta P$  vs  $t$ ” a). The grey-colored area signifies the transient state of the air flux at a depth of 120 cm. The red-colored area signifies the transient state of the air flux at a depth of 75 cm. Diagram “ $\Delta_{(120-75)}$  vs  $t$ ” b). The green-colored area represents the transient state of air flux for both depths. - The grey-colored area represents the air flux that reached a steady state at a depth of 120 cm but is still in a transient state at the depth of 75 cm. The air flux utilized for this diagram was 0.5 l/min. For a detailed explanation, please refer to the accompanying text.

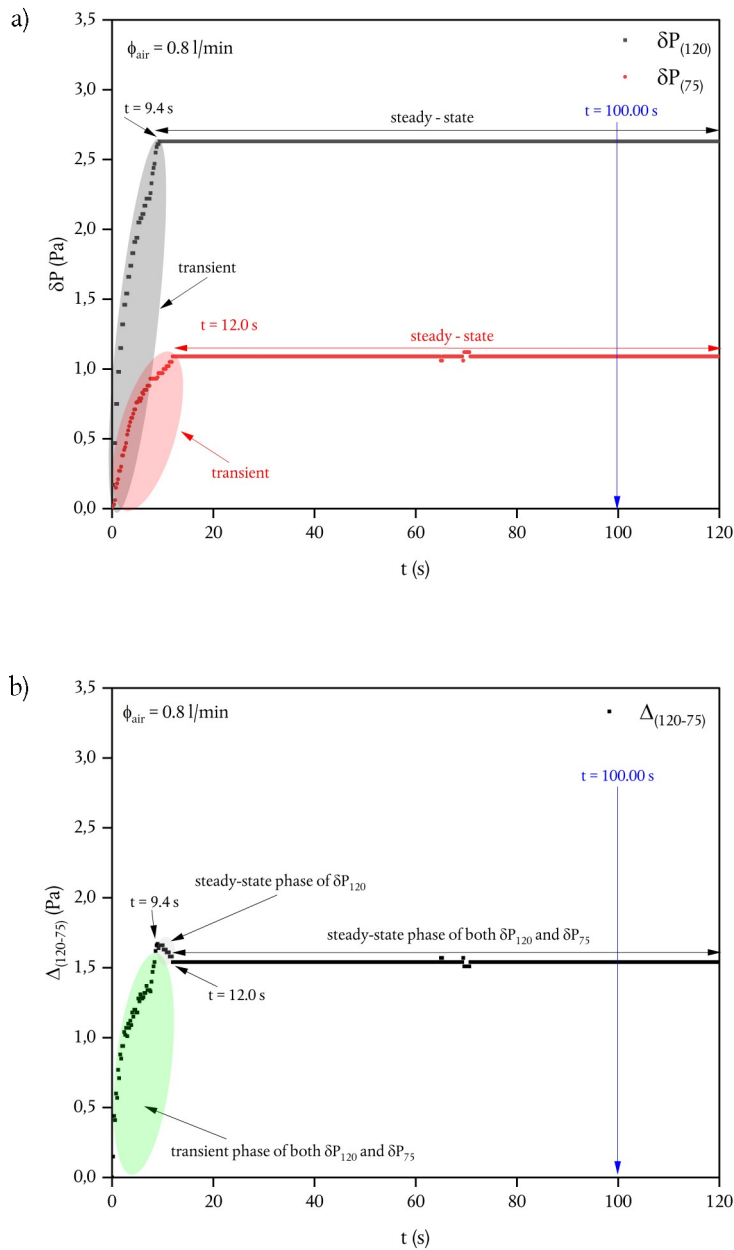


**Figure 4.6**— Diagram “ $\delta P$  vs  $t$ ” a). The grey-colored area signifies the transient state of the air flux at a depth of 120 cm. The red-colored area signifies the transient state of the air flux at a depth of 75 cm. Diagram “ $\Delta_{(120-75)}$  vs  $t$ ” b). The green-colored area represents the transient state of air flux for both depths. - The grey-colored area represents the air flux that reached a steady state at a depth of 120 cm but is still in a transient state at the depth of 75 cm. The air flux utilized for this diagram was 0.8 l/min. For a detailed explanation, please refer to the accompanying text.

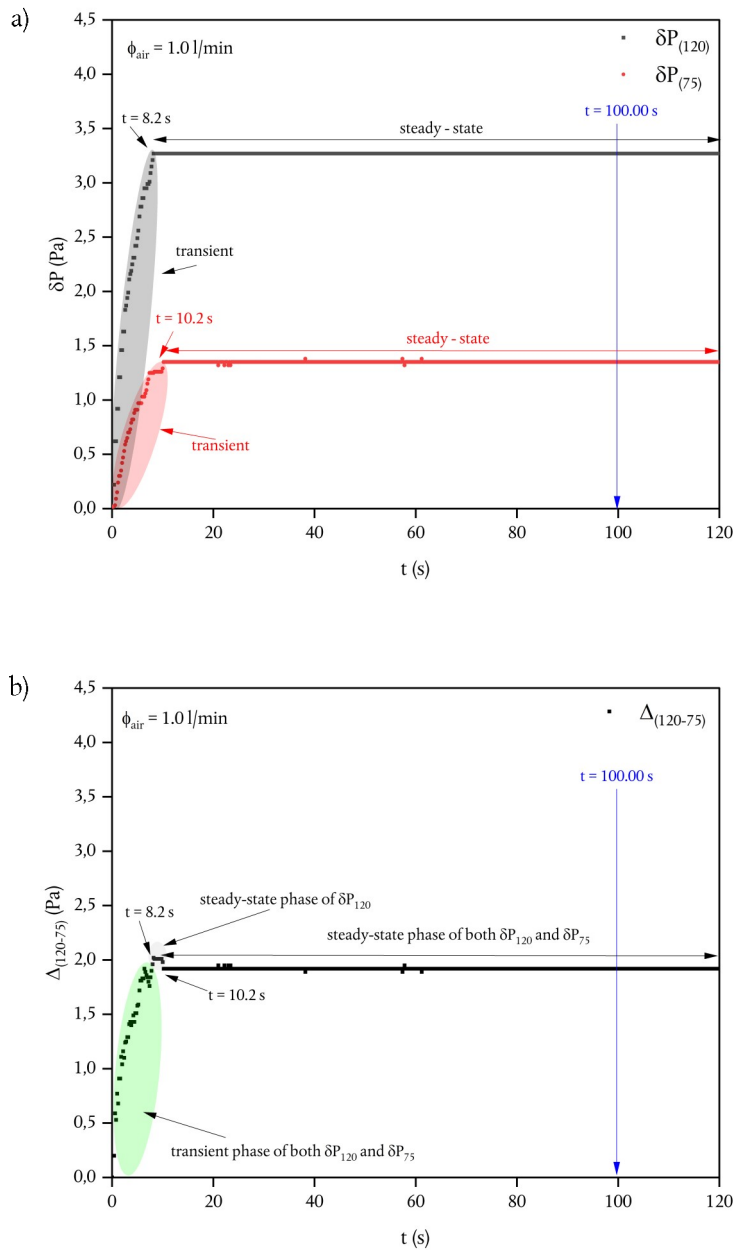


**Figure 4.7**— Diagram “ $\delta P$  vs  $t$ ” a). The grey-colored area signifies the transient state of the air flux at a depth of 120 cm. The red-colored area signifies the transient state of the air flux at a depth of 75 cm. Diagram “ $\Delta_{(120-75)}$  vs  $t$ ” b). The green-colored area represents the transient state of air flux for both depths. - The grey-colored area represents the air flux that reached a steady state at a depth of 120 cm but is still in a transient state at the depth of 75 cm. The air flux utilized for this diagram was 1.0 l/min. For a detailed explanation, please refer to the accompanying text.

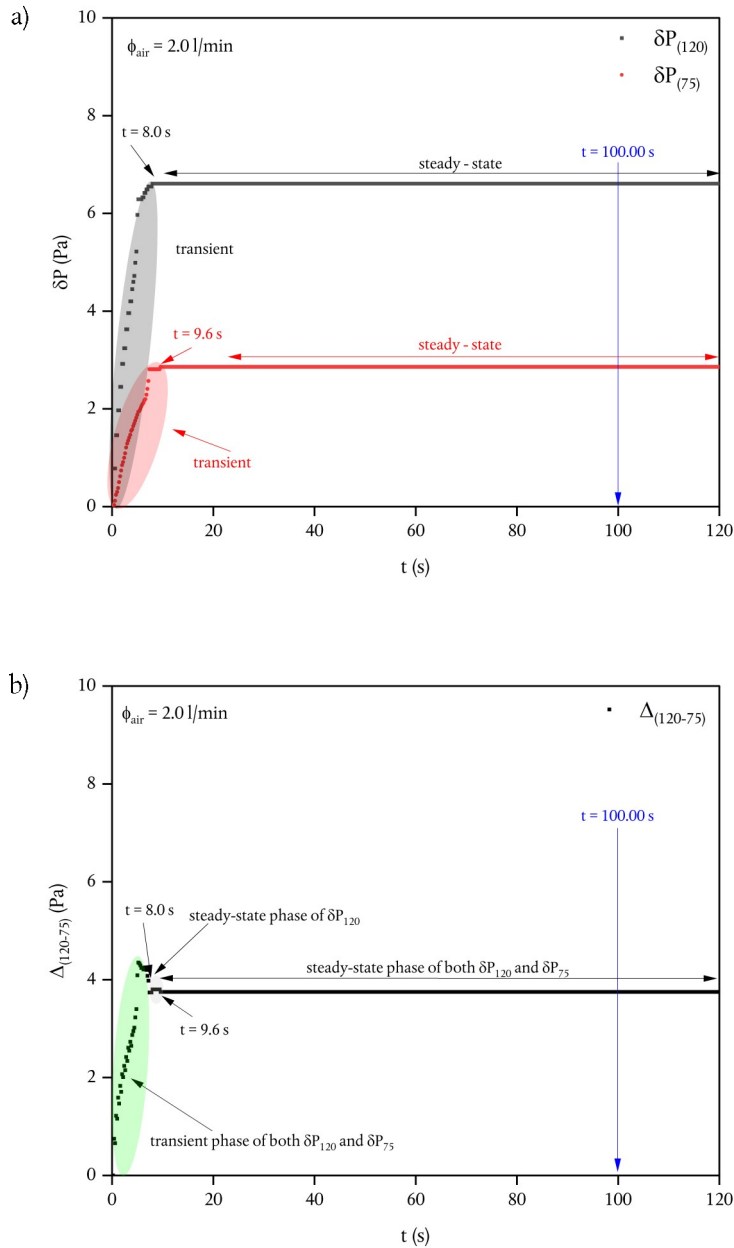


**Figure 4.8**— Diagram “ $\delta P$  vs  $t$ ” a). The grey-colored area signifies the transient state of the air flux at a depth of 120 cm. The red-colored area signifies the transient state of the air flux at a depth of 75 cm. Diagram “ $\Delta_{(120-75)}$  vs  $t$ ” b). The green-colored area represents the transient state of air flux for both depths. - The grey-colored area represents the air flux that reached a steady state at a depth of 120 cm but is still in a transient state at the depth of 75 cm. The air flux utilized for this diagram was 2.0 l/min. For a detailed explanation, please refer to the accompanying text.

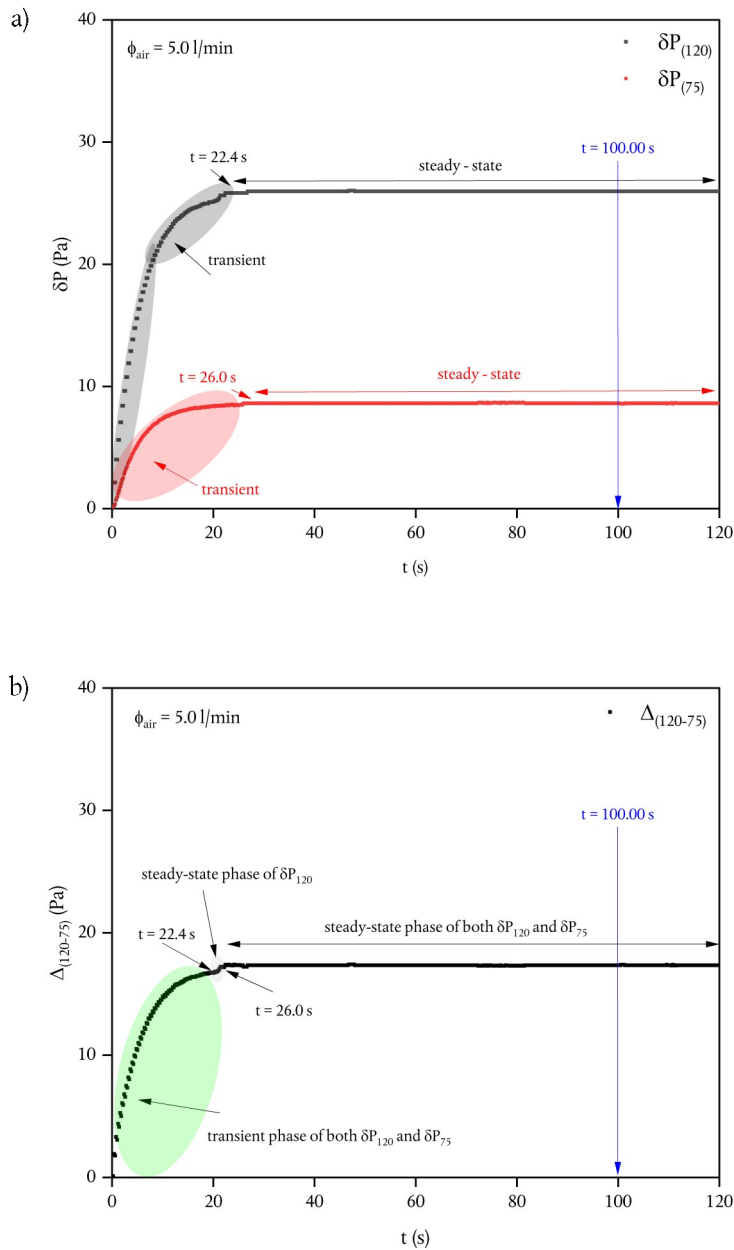


**Figure 4.9**— Diagram “ $\delta P$  vs  $t$ ” a). The grey-colored area signifies the transient state of the air flux at a depth of 120 cm. The red-colored area signifies the transient state of the air flux at a depth of 75 cm. Diagram “ $\Delta_{(120-75)}$  vs  $t$ ” b). The green-colored area represents the transient state of air flux for both depths. - The grey-colored area represents the air flux that reached a steady state at a depth of 120 cm but is still in a transient state at the depth of 75 cm. The air flux utilized for this diagram was 5.0 l/min. For a detailed explanation, please refer to the accompanying text.



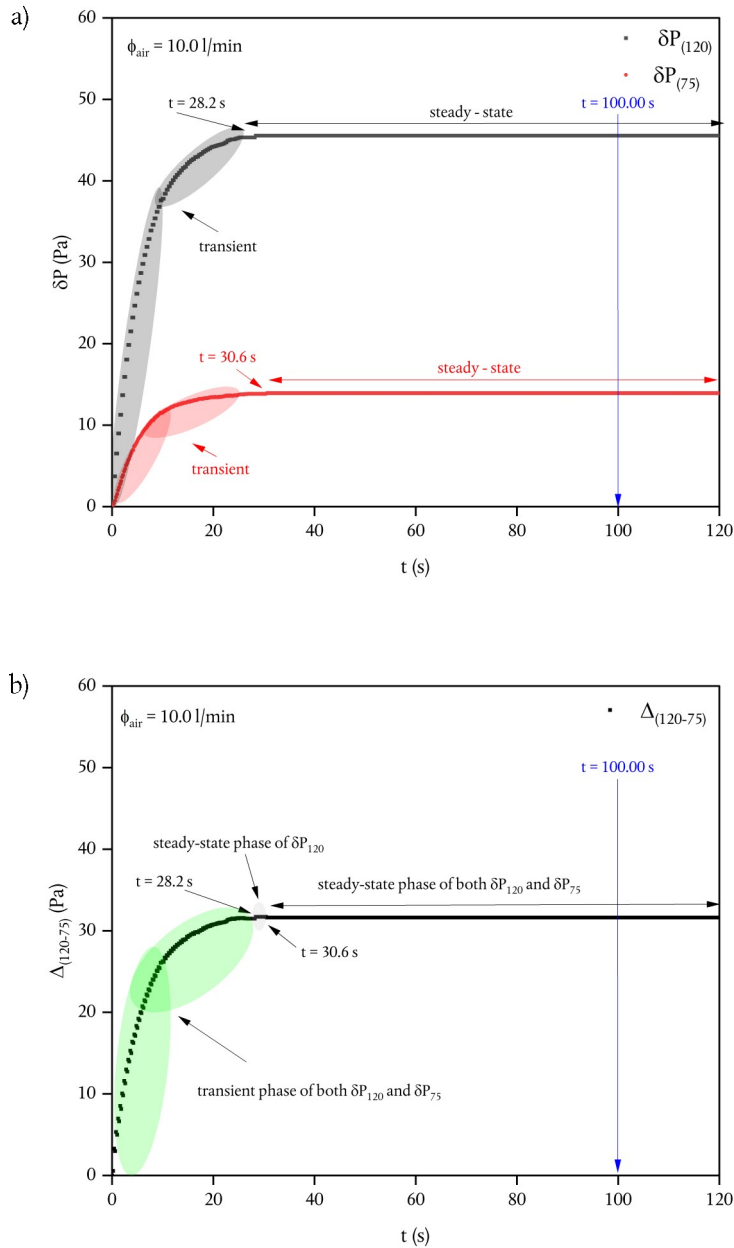


**Figure 4.10**— Diagram “ $\delta P$  vs  $t$ ” a). The grey-colored area signifies the transient state of the air flux at a depth of 120 cm. The red-colored area signifies the transient state of the air flux at a depth of 75 cm. Diagram “ $\Delta_{(120-75)}$  vs  $t$ ” b). The green-colored area represents the transient state of air flux for both depths. - The grey-colored area represents the air flux that reached a steady state at a depth of 120 cm but is still in a transient state at the depth of 75 cm. The air flux utilized for this diagram was 10.0 l/min. For a detailed explanation, please refer to the accompanying text.

$\phi_{air}$	$t^{ss}_{120}$	$t^{ss}_{75}$	$\delta t^{ss}$
l/min	s	s	s
0.1	19.4	25.0	5.6
0.2	18.2	22.8	4.6
0.3	17.2	21.2	4.0
0.4	15.2	18.8	3.6
0.5	11.8	14.8	3.0
0.8	9.4	12.0	2.6
1.0	8.2	10.2	2.0
2.0	8.0	9.6	1.6
5.0	22.4	26.0	3.6
10.0	28.2	30.6	2.4

Table 4.1 – Values of the time ( $t^{ss}_{120}$ ,  $t^{ss}_{75}$ , and their difference  $\delta t^{ss}$ ) taken to reach the steady state based on the different air fluxes ( $\phi_{air}$ ) used.

To ascertain whether the air flux ( $\phi_{air}$ ) is in the laminar regime, the Reynolds number (i.e., the ratio of inertial to viscous forces;  $R_e$ ) can be determined as per the methodology outlined by (Rouf *et al.*, 2016):

$$R_e = \frac{\phi_{air} D50 \rho_{air}}{A \mu_{air}}$$

where  $\frac{\phi_{air}}{A}$  is the Darcian velocity of air (m/s) calculated at the end of the injection valve ( $d=4$  cm); D50 is the average grain diameter of the porous matrix (m), which is indicative of the pore size. This refers to the size of grain diameter such that 50% of the particles by mass are smaller than that size (Knappett and Craig, 2012), based on the particle size distribution curve;  $\rho_{air}$  and  $\mu_{air}$  are the air density ( $\text{kg/m}^3$ ) and the air dynamic viscosity (Pa s), respectively, calculated at a temperature of 35.0 °C.

$Re \leq 1$  denotes that the air flux ( $\phi_{air}$ ) is laminar (Bear, 1972). Table 4.2 shows the values of the calculated  $Re$ .

The values of  $Re$  in table 4.2 indicate that air flux ( $\phi_{air}$ ) of 5.0 l/min and 10.0 l/min are in turbulent regimen. This observation may be extended to the air flux ( $\phi_{air}$ ) of 2.0 l/min, as depicted in Figure 4.11 b, where evident behavior at the limit between laminar and turbulent is observed.

Experimental observations generally substantiate the fact that, beyond a certain distance of flux, a laminar boundary layer undergoes a transition to turbulence. This phenomenon manifests across diverse fluid types and scales. This transition results in the establishment of a continuous turbulent flux; however, this occurs only at a significant distance from the system inlet. Intermediate flux experiences intermittent shifts between laminar and turbulent states, characterized by irregular intervals of transition (Kambe, 2007; Jain, Paradkar and Chitre, 2023).

The air flux ( $\phi_{air}$ ) of 2.0 l/min can be described as exhibiting transitional behavior, demonstrating characteristics that lie between laminar and turbulent fluxes. Figure 4.11 illustrates a boundary behavior, while Figures 4.12 and 4.13 depict a linear trend toward lower

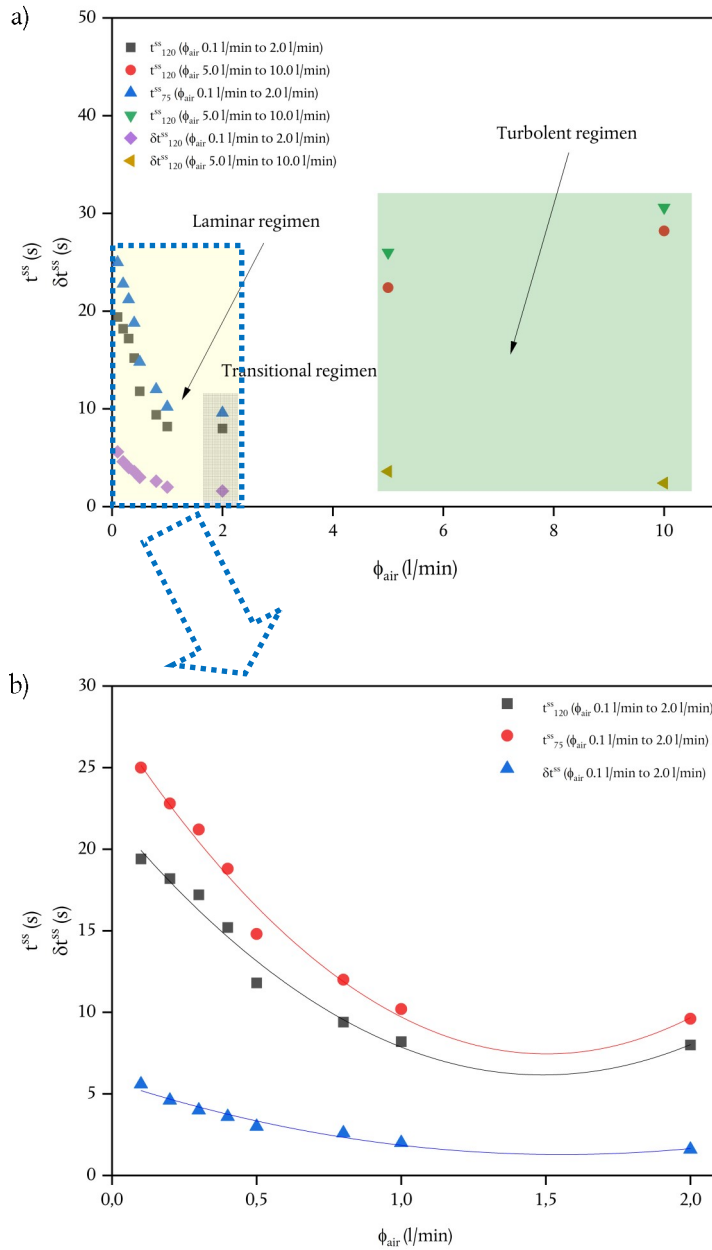


**Figure 4.11**— Diagrams show the time ( $t_{120}^{ss}$ ,  $t_{75}^{ss}$ , and their difference  $\delta t^{ss}$ ) taken to reach the steady state against the air flux ( $\phi_{air}$ ) a). Close-up of the time ( $t_{120}^{ss}$ ,  $t_{75}^{ss}$ , and their difference  $\delta t^{ss}$ ) taken to reach the steady state against the air flux ( $\phi_{air}$ ) based on the different air fluxes ( $\phi_{air}$ ) from 0.1 l/min to 2.0 l/min b). The yellow-colored area in a) represents the air fluxes ( $\phi_{air}$ ) in laminar regimen. The green-colored area in a) represents the air fluxes ( $\phi_{air}$ ) in turbulent regimen. The squared area within the yellow-colored area in a) represents the air fluxes ( $\phi_{air}$ ) in transitional regimen. For a detailed explanation, please refer to the accompanying text.

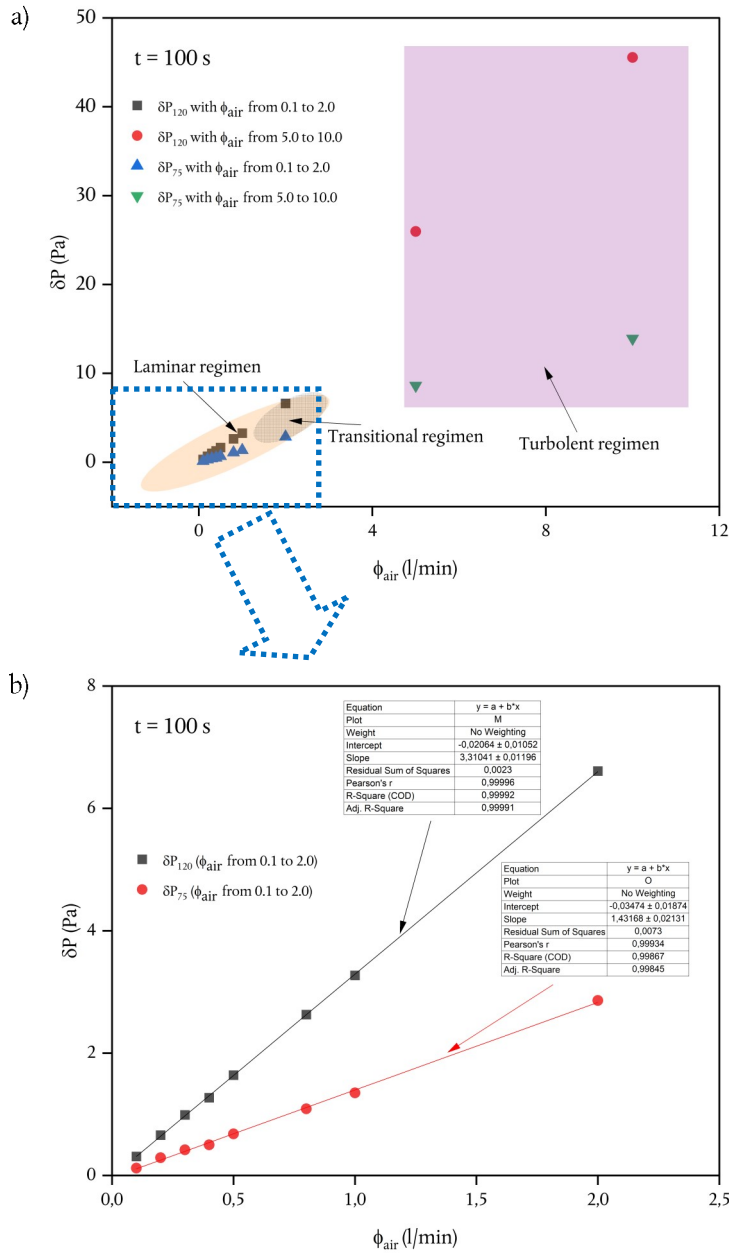
air fluxes ( $\phi_{air}$ ). Figures 4.12 and 4.13 show the diagrams “ $\delta P$  vs  $\phi_{air}$ ” and “ $\Delta_{(120-75)}$  vs  $\phi_{air}$ ”, respectively.

The values of  $\delta P_{120}$ ,  $\delta P_{75}$ , and  $\Delta_{(120-75)}$  for the flux of 0.2 l/min exhibit a significant linear correlation respect to the air flux ( $\phi_{air}$ ). Figures 4.12 and 4.13 show the Pearson correlation coefficients,  $R^2$ , and adjusted  $R^2$ .

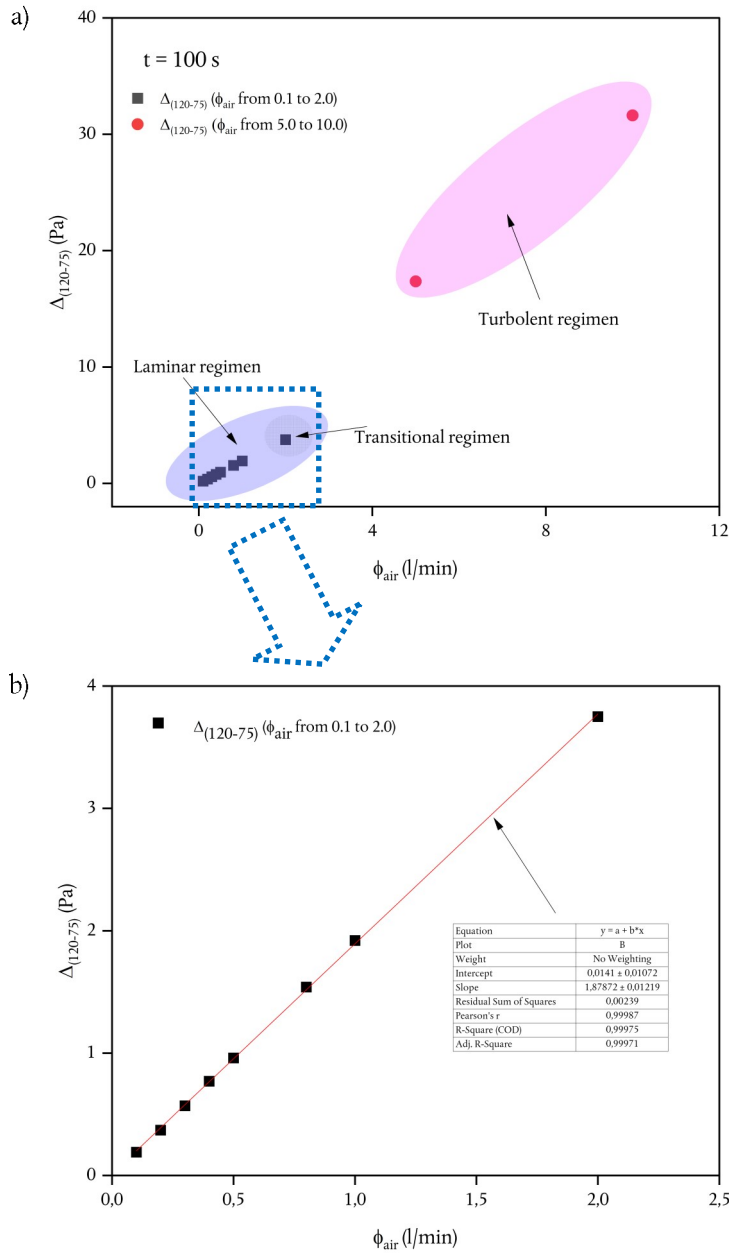
$\phi_{air}$ l/min	$\phi_{air}$ m <sup>3</sup> /s	$Re$ —
0.1	0.000001667	0.06
0.2	0.000003333	0.11
0.3	0.000005000	0.17
0.4	0.000006667	0.23
0.5	0.000008333	0.29
0.8	0.000013333	0.46
1.0	0.000016667	0.57
2.0	0.000033333	1.14
5.0	0.000083333	2.85
10.0	0.000166667	5.70

Table 4.2 – Reynolds numbers obtained at different air fluxes ( $\phi_{air}$ ).

A supplementary experimental section was carried out to identify disparities in the air fluxes ( $\phi_{air}$ ) at the inlet (as gauged by the fluxmeter) and outlet (as gauged at the level  $\emptyset$ ) of the "IEA". The soil CO<sub>2</sub> flux ( $\phi_{CO_2}$ ) measurement method, described by (Chiodini *et al.*, 1998; Giammanco *et al.*, 2007), and widely adopted in volcanic and geothermal areas, were employed for the investigation.



**Figure 4.12**— Diagram “ $\delta P$  vs  $\phi_{\text{air}}$ ” a). Close-up of the Diagram “ $\delta P$  vs  $\phi_{\text{air}}$ ” based on the different air fluxes ( $\phi_{\text{air}}$ ) from 0.1 l/min to 2.0 l/min b). The salmon-colored area in a) represents the air fluxes ( $\phi_{\text{air}}$ ) in laminar regimen. The purple-colored area in a) represents the air fluxes ( $\phi_{\text{air}}$ ) in turbulent regimen. The squared area within the salmon-colored area in a) represents the air fluxes ( $\phi_{\text{air}}$ ) in transitional regimen. For a detailed explanation, please refer to the accompanying text.



**Figure 4.13**—Diagram “ $\Delta_{(120-75)}$  vs  $\phi_{\text{air}}$ ” a). Close-up of the Diagram “ $\delta P$  vs  $\phi_{\text{air}}$ ” based on the different air fluxes ( $\phi_{\text{air}}$ ) from 0.1 l/min to 2.0 l/min b). The violet-colored area in a) represents the air fluxes ( $\phi_{\text{air}}$ ) in laminar regimen. The pink-colored area in a) represents the air fluxes ( $\phi_{\text{air}}$ ) in turbulent regimen. The squared area within the violet-colored area in a) represents the air fluxes ( $\phi_{\text{air}}$ ) in transitional regimen. For a detailed explanation, please refer to the accompanying text.

An air tank with a CO<sub>2</sub> concentration of 745 ppm was employed for this experimental section, which was conducted at a temperature of 20°C. The outlet CO<sub>2</sub> flux ( $\phi_{CO_2}$ ) were measured under conditions where the  $\delta P_{120}$  and  $\delta P_{75}$  readings exhibited steady – state patterns.

Table 4.3 shows the results where the outlet CO<sub>2</sub> fluxes ( $\phi_{CO_2}$ ) are in good agreement with the inlet CO<sub>2</sub> fluxes ( $\phi_{CO_2}$ ). The findings demonstrate that, for the analyzed air fluxes ( $\phi_{air}$ ), the inlet CO<sub>2</sub> fluxes ( $\phi_{CO_2}$ ) remain constant throughout the entire length of the "IEA".

		inlet			outlet	
$\phi_{air}$	$\phi_{air}$	$\phi_{air}$	$\phi_{CO_2}$	$\phi_{CO_2}$	$\phi_{CO_2}$	$\phi_{CO_2}$
l/min	g/m <sup>3</sup> h	g/m <sup>2</sup> d	g/m <sup>2</sup> h	gr/m <sup>2</sup> d	g/m <sup>2</sup> h	g/m <sup>2</sup> d
			<i>measured</i>	<i>measured</i>	<i>measured</i>	<i>measured</i>
0.5	463.67	11128.11	0.42	9.98	0.40	9.60
0.3	278.20	6676.87	0.25	5.99	0.24	5.76
0.1	185.47	4451.25	0.17	3.99	0.19	4.56

Table 4.3 – Outlet CO<sub>2</sub> fluxes ( $\phi_{CO_2}$ ) measured.

Upon verifying the initial hypotheses of isotropy and homogeneity of the ground basalt employed to fill the "IEA", we proceeded with the measurement of the intrinsic permeability.

As discussed in Chapter 2, the advective fluid transport in a natural porous medium is governed by Darcy's law. This highlights the relationship between gas Darcy velocity ( $\bar{u}_g$ ) of the fluid and the pressure gradient ( $\nabla P_g$ ):



$$\bar{u}_g = - \frac{k_g}{\mu_g} (\nabla P_g - \rho_g \bar{g})$$

Intrinsic permeability is primarily contingent upon the characteristics of the porous medium, with minimal reliance on the nature of the permeating fluid under ideal circumstances where there is no fluid-soil interaction. However, in instances involving interaction, particularly with water and other liquids, the properties of the fluid can considerably influence the intrinsic permeability of the medium (Druhan and Tournassat, 2019).

By combining Darcy's law with the continuity equation, one can derive the fundamental equation for gas transfer through porous media. Here,  $n$  represents the porosity of the porous medium (Bear, 1972):

$$\nabla \left( \rho \frac{k}{\mu} \nabla P \right) = n \frac{\delta \rho}{\delta t}, \text{ or}$$

$$\nabla^2 \rho P = 0 \text{ [eq. 4.1]}$$

if the system is under steady state conditions, at constant temperature ( $\mu = \text{constant}$ ) and the porous medium is homogeneous and isotropic ( $k = \text{constant}$ ). Moreover, assuming ideal behavior regarding the gas involved in the transfer process and constant temperature:

$$\rho = cP,$$

where  $c = M/RT$ ,  $M$  is the molecular weight of a generic gas,  $R$  is the universal gas constant and  $T$  is the absolute temperature. Substituting this expression in equation [eq. 4.1], Laplace's equation is obtained:

$$\nabla^2 \Omega = 0 \text{ [eq. 4.2]}$$

where  $\Omega = cP^2$ . Equation [eq. 4.2] can be used to determine the gas pressure spatial variation for any gas advection model.

Modeling a radial gas pressure distribution through a porous medium, it is useful to express Laplace's equation using the polar spherical coordinates  $r$ ,  $\theta$  and  $\gamma$  (Wang, 2017; Altland and von Delft, 2019; Weltner *et al.*, 2023). Recall that a point  $p \in \mathfrak{R}^3$  with position vector  $\mathbf{r}$  may be described in terms of polar coordinates ( $r$ ,  $\theta$  and  $\gamma$ ). The radial coordinate  $r = |\mathbf{r}|$  is the distance of point  $p$  from the origin. In particular  $r \geq 0$ . Whenever  $r > 0$  we define  $\theta$  to be the angle that  $\mathbf{r}$  makes with the (chosen) positive  $z$  axis, and take  $0 \leq \theta \leq \pi$ . Finally, whenever  $r > 0$  and  $0 \leq \theta \leq \pi$  we define  $\gamma$  to be the angle that the projection of  $\mathbf{r}$  into the plane  $z = 0$  makes with the positive  $x$  axis, measured counterclockwise. Thus  $0 \leq \gamma \leq 2\pi$ . It follows from the above that equation [eq. 4.2] in spherical coordinates is given by (Wang, 2017; Altland and von Delft, 2019; Weltner *et al.*, 2023):

$$\frac{1}{r^2} \frac{\delta}{\delta r} \left( r^2 \frac{\delta \Omega}{\delta r} \right) + \frac{1}{r \sin \theta} \frac{\delta}{\delta \theta} \left( \sin \theta \frac{\delta \Omega}{\delta \theta} \right) + \frac{1}{r^2 \sin^2 \theta} \frac{\delta}{\delta \gamma} \left( \frac{\delta^2 \Omega}{\delta \gamma^2} \right) = 0 \text{ [eq. 4.3]}$$

If  $\Omega$  is only a function of  $r$  (in which we do not consider the terms  $\theta$  and  $\gamma$ , in light of a hypothesis of a homogeneous and isotropic porous medium), then

$$\frac{\delta\Omega}{\partial\theta} = 0$$

and

$$\frac{\partial\Omega}{\partial\gamma} = 0$$

Therefore, Equation [eq. 4.3] can be rewritten as:

$$\frac{1}{r^2} \frac{\delta}{\delta r} \left( r^2 \frac{\delta\Omega}{\delta r} \right) = 0 \text{ [eq. 4.4]}$$

The solution  $\Omega$  of this second-order differential equation must satisfy the following first-order differential equation:

$$r^2 \frac{\delta\Omega}{\delta r} = a = \text{constant}$$

This differential equation can be rewritten as:

$$\frac{\delta\Omega}{\delta r} = \frac{a}{r^2}$$

The general solution of this first-order differential equation is:

$$\Omega(r) = -\frac{a}{r} + b$$

where  $b$  is a constant.

Following the similar approach adopted by (Marco Camarda, Gurrieri and Valenza, 2006), and considering two spherical shells with radii  $R_a$  ( $D - F_D$ ) and  $R_b$  ( $D - F_S$ ), which are concentric with origin at the base of the “IEA”, and assuming that the pressure of these two shells is equal to  $P_{120}$  and  $P_{75}$  respectively, the equation for the volumetric gas flux across a spherical shell of radius  $R_a$  is as follow:

$$\phi_{air}(120) = \frac{2\pi k_i R_a R_b (P_2^2 - P_1^2)}{\mu R_a - R_b P_1} \text{ [eq. 4.5]}$$

The intrinsic permeability ( $k_i$ ) is from equation [eq. 4.5]:

$$k_i = \frac{\mu \phi_{air}(120) R_a - R_b P_1}{2\pi R_a R_b (P_2^2 - P_1^2)} \text{ [eq. 4.6]}$$

Equation [eq. 4.6] can be rewritten as:

$$k_i = \frac{\mu \phi_{air}(120) \Delta H_{(120-75)}}{2\pi R_a R_b (P_2^2 - P_1^2)} \text{ [eq. 4.7]}$$

The parameter  $\frac{\Delta H_{(120-75)}}{R_1 R_2}$  depends on the geometrical configuration of the experimental apparatus and it is constant. This parameter can be defined as  $\Psi$ . “IEA” and “FEA” are built to have the same geometrical configuration.

$$\Psi_{IEA} = \Psi_{FEA}$$

Considering that the  $\phi_{air}$  is constant across the “IEA”, the equation [eq. 4.7] can be rewritten as:

$$k_i = \frac{\mu\phi_{air}}{2\pi} \Psi \frac{P_1}{(P_2^2 - P_1^2)} \text{ [eq. 4.8]}$$

Equation [eq. 4.8] is used to determinate the  $k_i$ .

$P_1$  (and also  $P_2$ ) could be also expressed in terms of gauge pressure:

$$P_1 = P_{atm} + \delta P_{120}$$

$$P_2 = P_{atm} + \delta P_{75}$$

Assuming that the values of  $\delta P \ll P_{atm}$ , equation [eq. 4.8] could be simplified as follows:

$$k_i = \frac{\mu\phi_{air}}{4\pi} \Psi \frac{1}{A_{(120-75)}} \text{ [eq. 4.9]}$$

Another simplification is to consider  $R_2$  at infinite distance ( $R_2 \Rightarrow \infty$ ) where air pressure in soil equals the barometric pressure  $P_{atm}$ . In this case, the intrinsic permeability ( $k_i$ ) will be (Qiu *et al.*, 2021):

$$k_i = \frac{\mu\phi_{air}}{2\pi} \frac{1}{R_1} \frac{P_1}{(P_1^2 - P_{atm}^2)} \text{ [eq. 4.10]}$$

Table 4.4 shows the values of  $k_i$  in the “IEA” determined by the equations [eq. 4.8], [eq. 4.9], and [eq. 4.10], respectively, by using the value of  $\Psi$  parameter of 0.020. The measurement has been conducted at a  $P_{atm}$  of 97,187 Pa and a temperature (T) of 35.0 °C. The values of  $k_i$  are calculated for each air flux ( $\phi_{air}$ ) used and by using the values of  $\delta P_{120}$  and  $\delta P_{75}$  sampled at 100 s.

$\phi_{\text{air}}$		[eq. 4.8]		[eq. 4.9]		[eq. 4.10]	
		$K_i$		$K_i$		$K_i$	
l/min	( $\text{cm}^3/\text{s}$ )	( $\mu\text{m}^2$ )	(darcys)	( $\mu\text{m}^2$ )	(darcys)	( $\mu\text{m}^2$ )	(darcys)
0.1	1.667	26.46	26.81	26.46	26.81	27.03	27.39
0.2	3.334	27.18	27.54	27.18	27.54	25.39	25.73
0.3	5.001	26.46	26.81	26.46	26.81	25.39	25.73
0.4	6.668	26.12	26.46	26.12	26.46	26.39	26.74
0.5	8.335	26.19	26.53	26.19	26.53	25.55	25.89
0.8	13.336	26.12	26.46	26.12	26.46	25.49	25.83
1.0	16.670	26.19	26.53	26.19	26.53	25.63	25.97
2.0	33.340	26.81	27.17	26.81	27.17	25.35	25.69
5.0	83.350	14.46	14.65	14.49	14.68	16.14	16.35
10.0	166.700	15.61	15.82	15.90	16.11	18.17	18.41

Table 4.4 – values of the intrinsic permeability ( $k_i$ ) of the “TEA” determined by the equations [eq. 4.8], [eq. 4.9], and [eq. 4.10].

$\phi_{\text{air}}$		[eq. 4.8]		[eq. 4.9]		[eq. 4.10]	
		$K_i$		$K_i$		$K_i$	
l/min	( $\text{cm}^3/\text{s}$ )	( $\mu\text{m}^2$ )	(darcys)	( $\mu\text{m}^2$ )	(darcys)	( $\mu\text{m}^2$ )	(darcys)
0.1	1.667	26.51	26.81	26.51	26.81	27.01	27.39
0.2	3.334	27.07	27.54	27.07	27.54	25.69	25.73
0.3	5.001	26.39	26.81	26.39	26.81	25.89	25.73
0.4	6.668	26.27	26.46	26.27	26.46	26.41	26.74
0.5	8.335	26.16	26.53	26.16	26.53	26.09	25.89
0.8	13.336	26.24	26.46	26.24	26.46	25.99	25.83
1.0	16.670	26.31	26.53	26.31	26.53	25.79	25.97
2.0	33.340	26.63	27.17	26.63	27.17	25.87	25.69
5.0	83.350	15.14	14.65	15.18	14.68	16.11	16.35
10.0	166.700	15.44	15.82	15.59	16.11	17.87	18.41

Table 4.5 – values of the intrinsic permeability ( $k_i$ ) of the “FEA” determined by the equations [eq. 4.8], [eq. 4.9], and [eq. 4.10].

Table 4.5 shows the values of  $k_i$  in the “FEA” determined by the equations [eq. 4.8], [eq. 4.9], and [eq. 4.10], respectively, by using the value of  $\Psi$  parameter of 0.020. The measurement has been conducted at a  $P_{atm}$  of 97,187 Pa and a temperature (T) of 35.0 °C. The values of  $k_i$  are calculated for each air flux ( $\phi_{air}$ ) used and by using the values of  $\delta P_{120}$  and  $\delta P_{75}$  sampled at 100 s.

Upon comparing the data presented in tables 4.4 and 4.5, it is evident that the values of the intrinsic permeability ( $k_i$ ) calculated for varying air fluxes ( $\phi_{air}$ ) are found to be consistent. Furthermore, the values of the intrinsic permeability ( $k_i$ ) for “IEA” and “FEA” are also within a comparable range. Notably, as previously posited in relation to turbulent flux, it is observed that the intrinsic permeability ( $k_i$ ) for air fluxes ( $\phi_{air}$ ) equal to 5.0 l/min and 10.0 l/min exhibit a substantial reduction in comparison to those at lower air fluxes ( $\phi_{air}$ ). This discrepancy signifies that the flows at 5.0 l/min and 10.0 l/min cannot be accurately represented by Darcy's law.

The experimental system's response to external air flux variations was also validated. In order to replicate these variations, the system was subjected to an air flux ( $\phi_{air}$ ) of 0.5 l/min for a duration of two minutes. Subsequently, the air flux ( $\phi_{air}$ ) was increased to 0.6 l/min for an additional two minutes.

Following this, the air flux ( $\phi_{air}$ ) was augmented to 1.0 l/min for another two minutes.

The experiment was concluded by resetting air flux ( $\phi_{air}$ ) of 0.6 l/min, and then to 0.5 l/min in subsequent intervals of two minutes for each step, until the air pump was deactivated.

Figure 4.14 shows the diagram “ $\delta P$  vs  $t$ ” for the above cited experiment. The diagram illustrates a consistent pattern where both  $\delta P_{120}$  and  $\delta P_{75}$  initially exhibit a transient phase, characterized by an increasing trend over time. Subsequently, a second phase is observed, wherein both  $\delta P_{120}$  and  $\delta P_{75}$  maintain a constant value as time progresses. This behavior is consistent with the information gained in Figures 4.1 to 4.10.

Upon completion of the experimental phases, it is evident that the prototype apparatuses promptly respond to pressure fluctuations induced by air fluxes ( $\phi_{air}$ ), with reaction times of less than one second. The prototype apparatuses have validated the initial hypotheses of homogeneity and isotropy, demonstrating their optimization for air fluxes ( $\phi_{air}$ ) within the range of 0.1 l/min to 2.0 l/min. Notably, the system achieves a steady-state within approximately ten seconds for air fluxes ( $\phi_{air}$ ) within the range of 0.1 l/min to 2.0 l/min, thus affirming its capacity to promptly acquire realistic parameters.



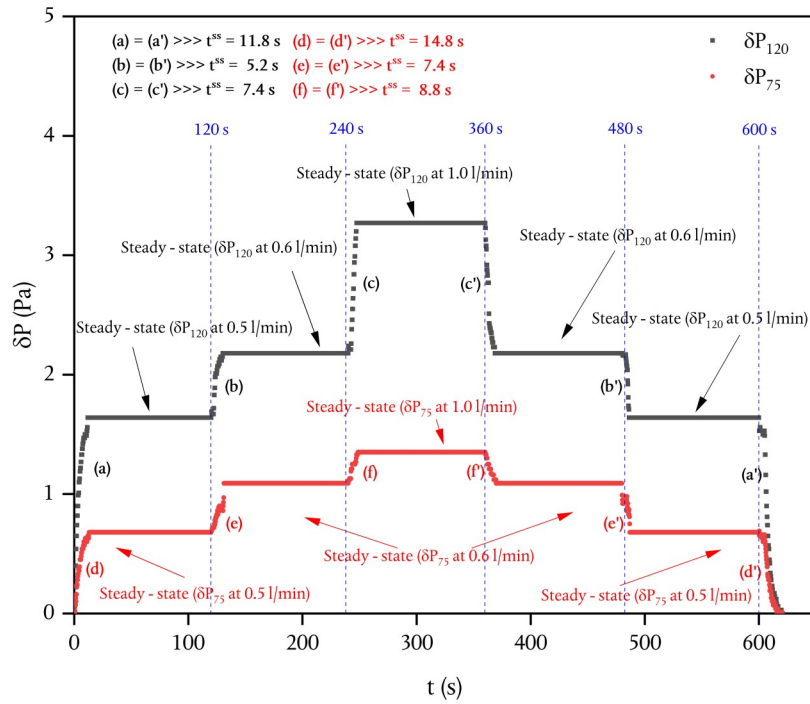


**Figure 4.14**— Diagram “ $\delta P$  vs  $t$ ” for the experiment related to the increase/decrease of the air flux ( $\phi_{air}$ ) in the system. The IEA was subjected to an air flux ( $\phi_{air}$ ) of 0.5 l/min for a duration of two minutes. Subsequently, the air flux ( $\phi_{air}$ ) was increased to 0.6 l/min for an additional two minutes. Following this, the air flux ( $\phi_{air}$ ) was augmented to 1.0 l/min for another two minutes. The experiment was concluded by resetting air flux ( $\phi_{air}$ ) of 0.6 l/min, and then to 0.5 l/min in subsequent intervals of two minutes for each step, until the air pump was deactivated. For a detailed explanation, please refer to the accompanying text.

## CHAPTER 5

### GEOCHEMICAL OBSERVATIONS ON DATA ANALYSIS

---

#### Introduction

The IEA utilized to replicate a natural degassing system, as delineated in Chapter 3, was also employed to execute several tests assessing the efficacy of the method for gauging gas pressure fluctuations in instances of CO<sub>2</sub> diffusion. The findings derived from these tests are expounded upon in the present chapter.

In the course of these experiments, a gas tank containing known concentrations (20% CO<sub>2</sub>, 300 ppm He, in an N<sub>2</sub> matrix) was utilized in conjunction with a spectrometer equipped with a Gascard II Plus card (manufactured by Edinburgh Instruments Ltd) specifically designed for CO<sub>2</sub> detection, featuring a detection range from 0% to 10%.

The aforementioned experiments were undertaken at a temperature of 25°C and a barometric pressure of 972.38 hPa. The inlet gas fluxes ( $\phi_{gas}$ ) in the system and the spectrophotometer are documented in Figures 5.1 to 5.15. The concentration of CO<sub>2</sub> was measured by employing a soil profile gas probe positioned perpendicularly to the base of the "IEA," with sampling tube depths (*compared to the level Ø of the IEA*) at 25, 50, 75, and 100 cm.

The system underwent pre-conditioning with a gas tank (CO<sub>2</sub> concentration of 20%) for approximately two hours followed by an additional three-hour pre-conditioning with an air tank (CO<sub>2</sub> concentration of 745 ppm). Subsequently, the experimental phase described below was initiated.

**Results and discussion**

Table 5.1 presents the CO<sub>2</sub> concentration values recorded at different time intervals and depths.

At the initial time point (t<sub>0</sub>) (Figure 5.1), corresponding to the system activation, there is a relatively higher CO<sub>2</sub> concentration at depths of 25 cm and 50 cm. This CO<sub>2</sub> concentration is considered residual from the gas tank (CO<sub>2</sub> concentration of 20%). Depths of 75 cm and 100 cm exhibit lower CO<sub>2</sub> concentrations. This potentially represents the residual CO<sub>2</sub> concentration of the conditioning phase above - mentioned.

At the time point t<sub>1</sub> (Figure 5.2), a marginal increase in CO<sub>2</sub> concentration is observed at the depth of 100 cm, while the CO<sub>2</sub> concentrations at other depths closely resemble those recorded at t<sub>0</sub>.

t (s)	0	420	900	1500	1800	2160	2280	2460	2520	2700	2880	3000	3180	3660	3900	6300
	t <sub>0</sub>	t <sub>1</sub>	t <sub>2</sub>	t <sub>3</sub>	t <sub>4</sub>	t <sub>5</sub>	t <sub>6</sub>	t <sub>7</sub>	t <sub>8</sub>	t <sub>9</sub>	t <sub>10</sub>	t <sub>11</sub>	t <sub>12</sub>	t <sub>13</sub>	t <sub>14</sub>	t <sub>15</sub>
Depth cm	[CO <sub>2</sub> ] %															
-25	0.17	0.18	0.19	0.18	0.22	0.31	0.24	0.18	0.29	0.30	0.35	0.30	0.40	0.23	0.33	0.69
-50	0.17	0.17	0.17	0.18	0.22	0.26	0.25	0.22	0.33	0.36	0.58	0.71	0.81	1.30	1.60	5.83
-75	0.13	0.14	0.27	1.57	2.02	2.50	3.06	3.62	4.26	4.83	5.38	5.98	6.45	7.67	8.15	14.09
-100	0.13	0.61	7.30	7.83	8.97	9.57	10.20	16.80	11.21	11.65	12.02	12.40	12.85	13.30	14.00	18.57

**Table 5.1** – Concentrations of CO<sub>2</sub> determined in spectrometry (Gascard II Plus) from t<sub>0</sub> to t<sub>15</sub>

This observation indicates that at  $t_1$  (420 seconds from system activation), the initial impact of the gas fluxes ( $\phi_{gas}$ ) with a CO<sub>2</sub> concentration of 20% is exclusively discernible at 100 cm depth.

At the time point  $t_2$  (Figure 5.3), a marginal increase in CO<sub>2</sub> concentration is observed at the depth of 75 cm. CO<sub>2</sub> concentration at 100 cm of depth is increased at 7.30%, while the CO<sub>2</sub> concentrations at other depths closely resemble those recorded at  $t_1$ . This observation indicates that at  $t_2$  (900 seconds from system activation), the initial impact of the gas fluxes ( $\phi_{gas}$ ) with a CO<sub>2</sub> concentration of 20% is slightly perceptible at 75 cm depth.

At the time points  $t_3$  to  $t_8$  (Figure 5.4 to 5.9), the CO<sub>2</sub> concentration at depths of 75 cm and 100 cm continuously increase, while the CO<sub>2</sub> concentrations at other depths show the residual CO<sub>2</sub> concentration of  $[\text{CO}_2]_{air}$ .

At the time point  $t_9$  (Figure 5.10), a marginal increase in CO<sub>2</sub> concentration is observed at the depth of 50 cm. This observation indicates that at  $t_9$  (2700 seconds from system activation), the initial impact of the gas fluxes ( $\phi_{gas}$ ) with a CO<sub>2</sub> concentration of 20% is slightly perceptible at the 50 cm depth.

At the time points  $t_{10}$  to  $t_{13}$  (Figure 5.11 to 5.14), the CO<sub>2</sub> concentration at depths of 50 cm, 75 cm, and 100 cm continuously

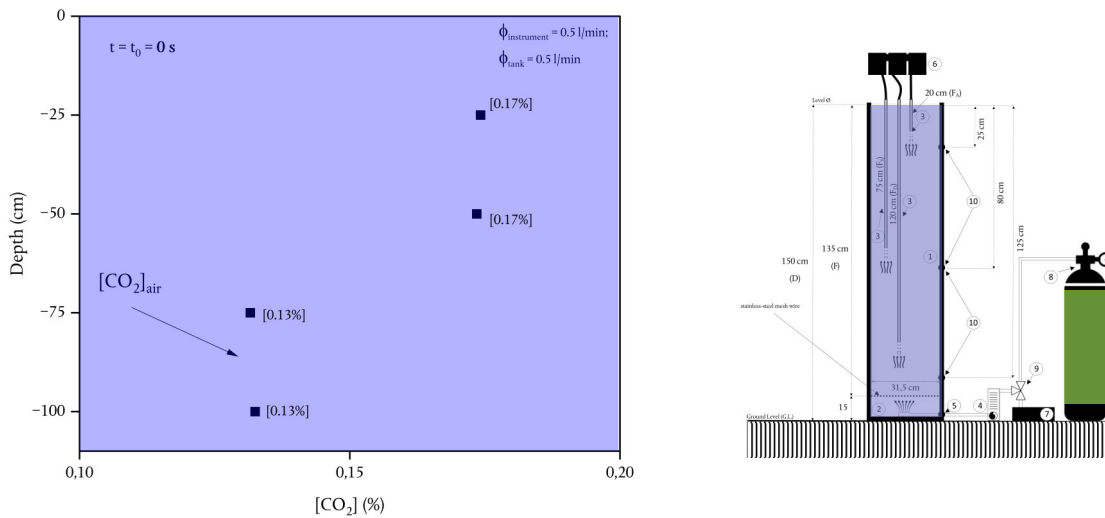


**Figure 5.1**— Diagram [CO<sub>2</sub>] vs Depth. This diagram depicts the upward propagation of a gas mixture enriched with CO<sub>2</sub> [20%]. The purple-colored area represents the CO<sub>2</sub> presence in the IEA (denoted in the Figure as [CO<sub>2</sub>]<sub>air</sub>), while the green-colored area signifies the CO<sub>2</sub> content in the gas tank (denoted in the Figure as [CO<sub>2</sub>]<sub>tank</sub>). The IEA is ideally positioned on the right side of the diagram. The gas propagates from the bottom to the top with a fixed gas flux. Figure 5.1 illustrates the system at  $t_0$ , corresponding to the moment of gas injection. The concentration values, expressed in percentages, are provided within square brackets in the figure. For a detailed explanation, please refer to the text.

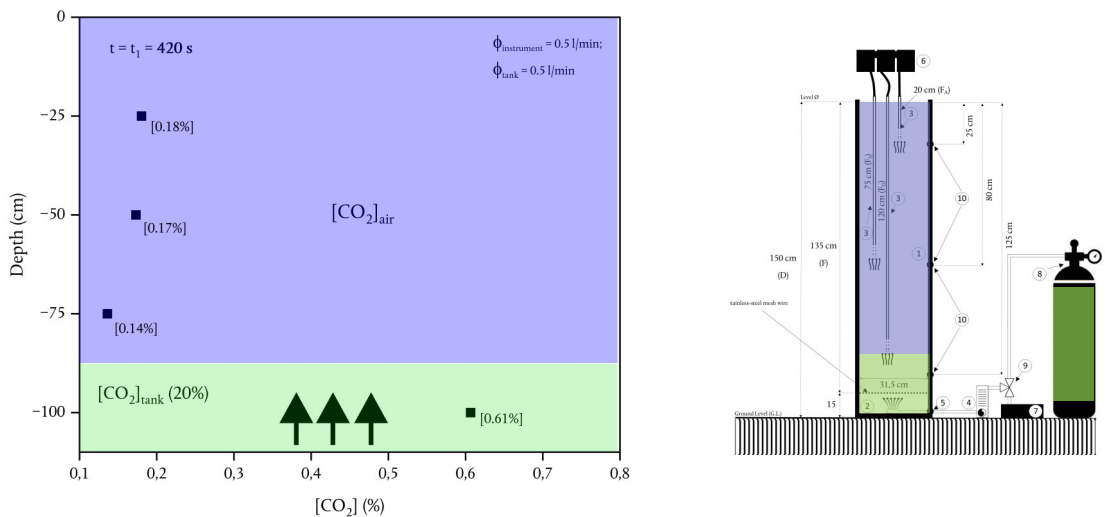


**Figure 5.2**— This diagram depicts the upward propagation of a gas mixture enriched with CO<sub>2</sub> [20%]. The purple-colored area represents the CO<sub>2</sub> presence in the IEA (denoted in the Figure as [CO<sub>2</sub>]<sub>air</sub>), while the green-colored area signifies the CO<sub>2</sub> content in the gas tank (denoted in the Figure as [CO<sub>2</sub>]<sub>tank</sub>). The IEA is ideally positioned on the right side of the diagram. The gas propagates from the bottom to the top with a fixed gas flux. Figure 5.2 illustrates the system at  $t_1$ , corresponding to a time of 420 seconds after the experiment started. The concentration values, expressed in percentages, are provided within square brackets in the figure. For a detailed explanation, please refer to the text.

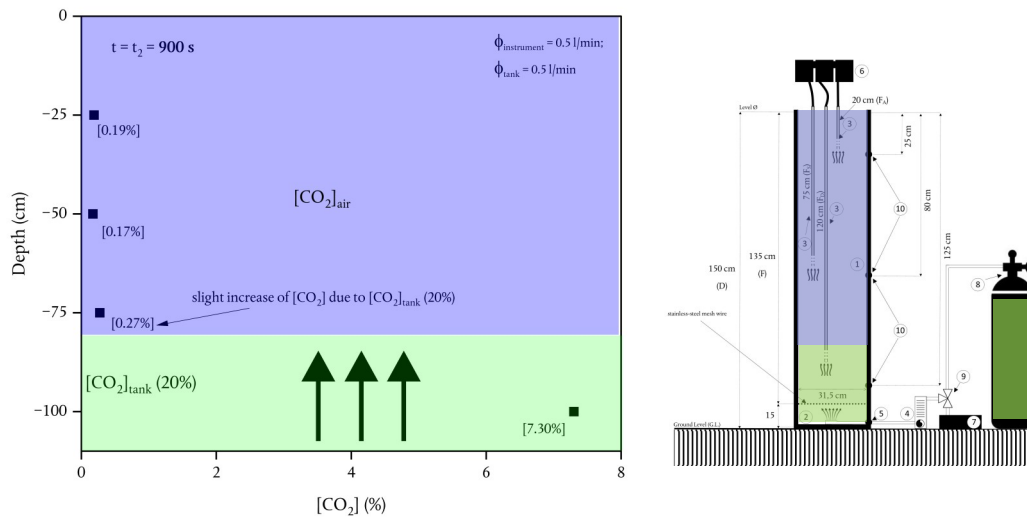


**Figure 5.3**— Diagram [CO<sub>2</sub>] vs Depth. This diagram depicts the upward propagation of a gas mixture enriched with CO<sub>2</sub> [20%]. The purple-colored area represents the CO<sub>2</sub> presence in the IEA (denoted in the Figure as [CO<sub>2</sub>]<sub>air</sub>), while the green-colored area signifies the CO<sub>2</sub> content in the gas tank (denoted in the Figure as [CO<sub>2</sub>]<sub>tank</sub>). The IEA is ideally positioned on the right side of the diagram. The gas propagates from the bottom to the top with a fixed gas flux. Figure 5.3 illustrates the system at  $t_2$ , corresponding to a time of 900 seconds after the experiment started. The concentration values, expressed in percentages, are provided within square brackets in the figure. For a detailed explanation, please refer to the text.

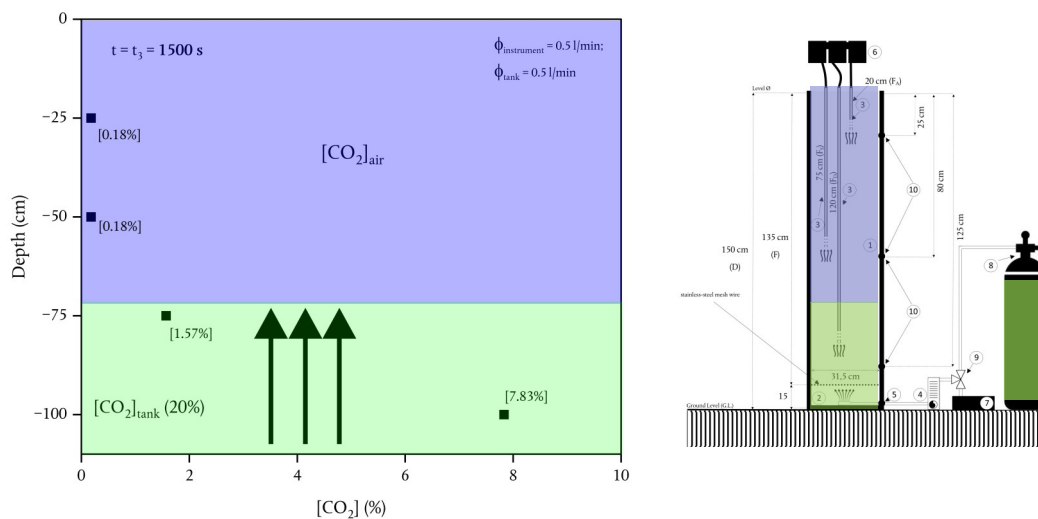


**Figure 5.4**— This diagram depicts the upward propagation of a gas mixture enriched with CO<sub>2</sub> [20%]. The purple-colored area represents the CO<sub>2</sub> presence in the IEA (denoted in the Figure as [CO<sub>2</sub>]<sub>air</sub>), while the green-colored area signifies the CO<sub>2</sub> content in the gas tank (denoted in the Figure as [CO<sub>2</sub>]<sub>tank</sub>). The IEA is ideally positioned on the right side of the diagram. The gas propagates from the bottom to the top with a fixed gas flux. Figure 5.4 illustrates the system at  $t_3$ , corresponding to a time of 1500 seconds after the experiment started. The concentration values, expressed in percentages, are provided within square brackets in the figure. For a detailed explanation, please refer to the text.

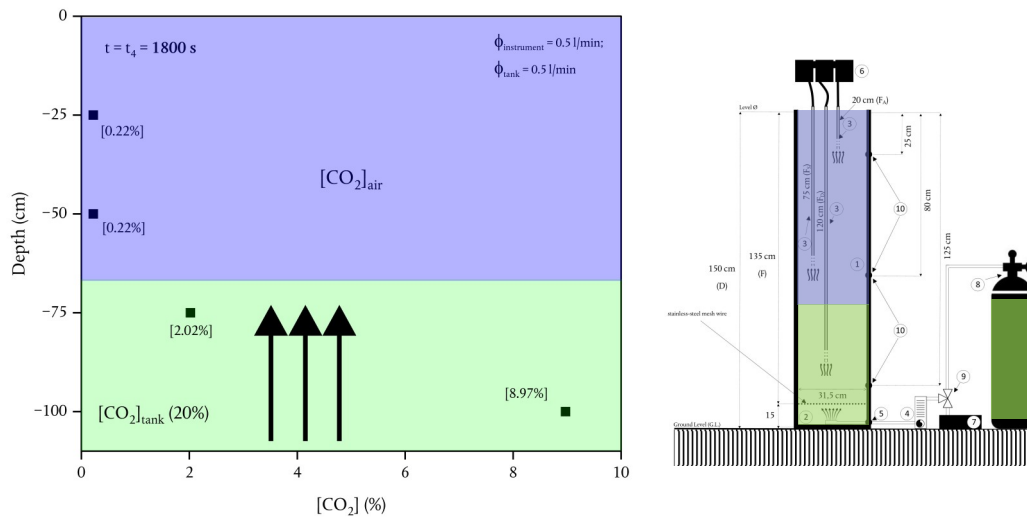


**Figure 5.5**— Diagram [CO<sub>2</sub>] vs Depth. This diagram depicts the upward propagation of a gas mixture enriched with CO<sub>2</sub> [20%]. The purple-colored area represents the CO<sub>2</sub> presence in the IEA (denoted in the Figure as [CO<sub>2</sub>]<sub>air</sub>), while the green-colored area signifies the CO<sub>2</sub> content in the gas tank (denoted in the Figure as [CO<sub>2</sub>]<sub>tank</sub>). The IEA is ideally positioned on the right side of the diagram. The gas propagates from the bottom to the top with a fixed gas flux. Figure 5.5 illustrates the system at  $t_4$ , corresponding to a time of 1800 seconds after the experiment started. The concentration values, expressed in percentages, are provided within square brackets in the figure. For a detailed explanation, please refer to the text.

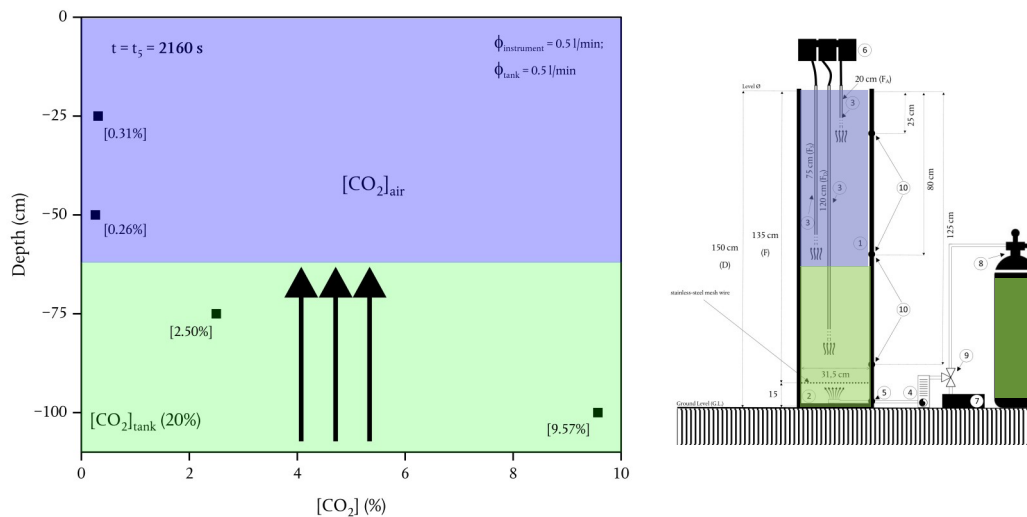


**Figure 5.6**— This diagram depicts the upward propagation of a gas mixture enriched with CO<sub>2</sub> [20%]. The purple-colored area represents the CO<sub>2</sub> presence in the IEA (denoted in the Figure as [CO<sub>2</sub>]<sub>air</sub>), while the green-colored area signifies the CO<sub>2</sub> content in the gas tank (denoted in the Figure as [CO<sub>2</sub>]<sub>tank</sub>). The IEA is ideally positioned on the right side of the diagram. The gas propagates from the bottom to the top with a fixed gas flux. Figure 5.6 illustrates the system at  $t_5$ , corresponding to a time of 2160 seconds after the experiment started. The concentration values, expressed in percentages, are provided within square brackets in the figure. For a detailed explanation, please refer to the text.

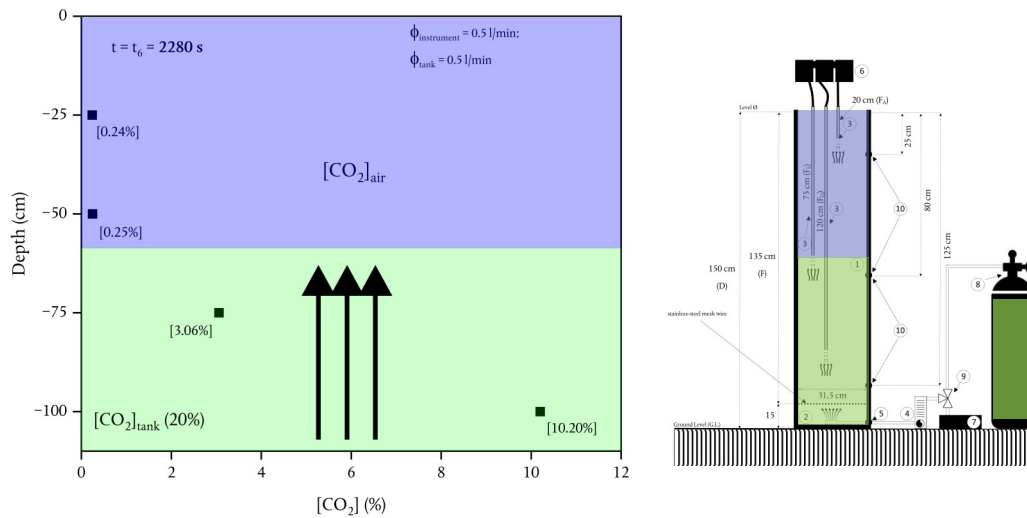


**Figure 5.7**— Diagram [CO<sub>2</sub>] vs Depth. This diagram depicts the upward propagation of a gas mixture enriched with CO<sub>2</sub> [20%]. The purple-colored area represents the CO<sub>2</sub> presence in the IEA (denoted in the Figure as [CO<sub>2</sub>]<sub>air</sub>), while the green-colored area signifies the CO<sub>2</sub> content in the gas tank (denoted in the Figure as [CO<sub>2</sub>]<sub>tank</sub>). The IEA is ideally positioned on the right side of the diagram. The gas propagates from the bottom to the top with a fixed gas flux. Figure 5.7 illustrates the system at  $t_6$ , corresponding to a time of 2280 seconds after the experiment started. The concentration values, expressed in percentages, are provided within square brackets in the figure. For a detailed explanation, please refer to the text.

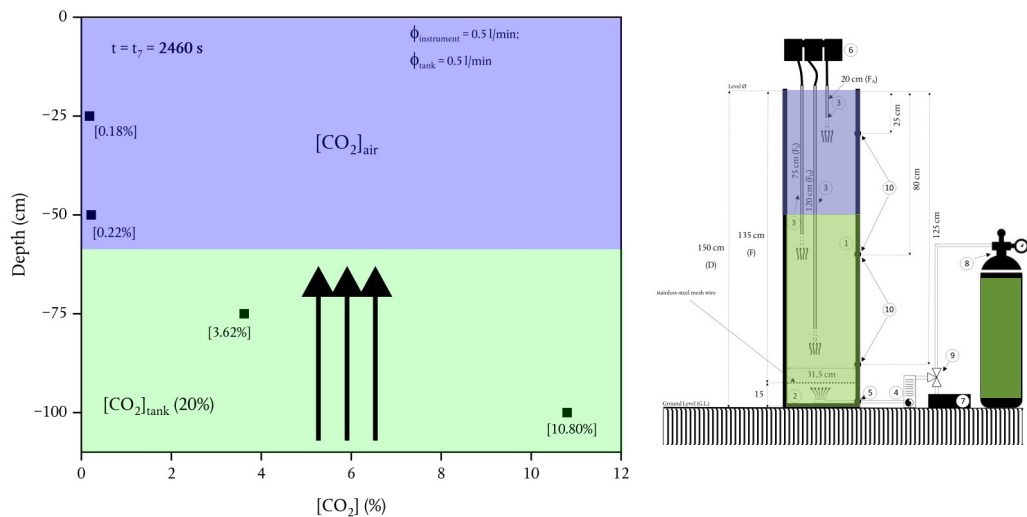


**Figure 5.8**— This diagram depicts the upward propagation of a gas mixture enriched with CO<sub>2</sub> [20%]. The purple-colored area represents the CO<sub>2</sub> presence in the IEA (denoted in the Figure as [CO<sub>2</sub>]<sub>air</sub>), while the green-colored area signifies the CO<sub>2</sub> content in the gas tank (denoted in the Figure as [CO<sub>2</sub>]<sub>tank</sub>). The IEA is ideally positioned on the right side of the diagram. The gas propagates from the bottom to the top with a fixed gas flux. Figure 5.8 illustrates the system at  $t_7$ , corresponding to a time of 2460 seconds after the experiment started. The concentration values, expressed in percentages, are provided within square brackets in the figure. For a detailed explanation, please refer to the text.



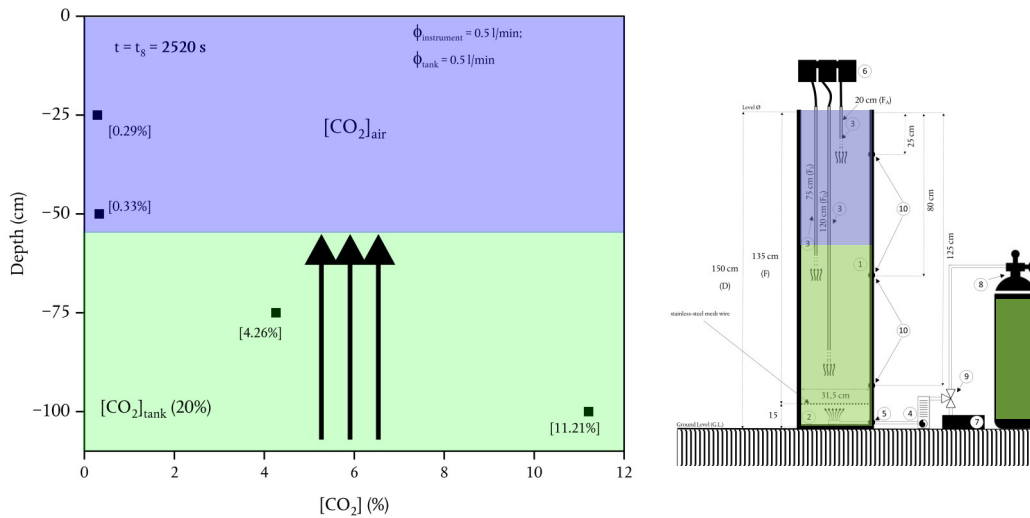


**Figure 5.9**— Diagram [CO<sub>2</sub>] vs Depth. This diagram depicts the upward propagation of a gas mixture enriched with CO<sub>2</sub> [20%]. The purple-colored area represents the CO<sub>2</sub> presence in the IEA (denoted in the Figure as [CO<sub>2</sub>]<sub>air</sub>), while the green-colored area signifies the CO<sub>2</sub> content in the gas tank (denoted in the Figure as [CO<sub>2</sub>]<sub>tank</sub>). The IEA is ideally positioned on the right side of the diagram. The gas propagates from the bottom to the top with a fixed gas flux. Figure 5.9 illustrates the system at  $t_8$ , corresponding to a time of 2520 seconds after the experiment started. The concentration values, expressed in percentages, are provided within square brackets in the figure. For a detailed explanation, please refer to the text.

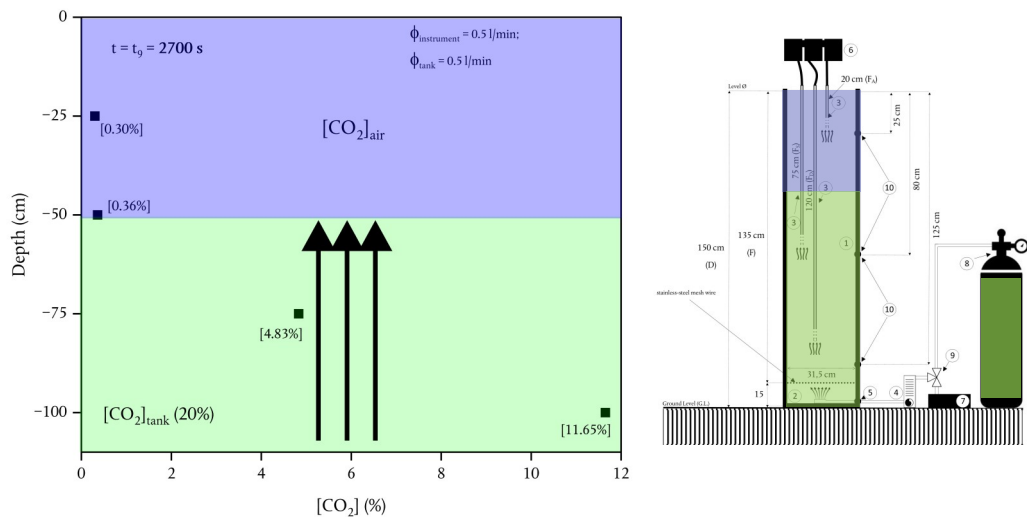


**Figure 5.10**— This diagram depicts the upward propagation of a gas mixture enriched with CO<sub>2</sub> [20%]. The purple-colored area represents the CO<sub>2</sub> presence in the IEA (denoted in the Figure as [CO<sub>2</sub>]<sub>air</sub>), while the green-colored area signifies the CO<sub>2</sub> content in the gas tank (denoted in the Figure as [CO<sub>2</sub>]<sub>tank</sub>). The IEA is ideally positioned on the right side of the diagram. The gas propagates from the bottom to the top with a fixed gas flux. Figure 5.10 illustrates the system at  $t_9$ , corresponding to a time of 2700 seconds after the experiment started. The concentration values, expressed in percentages, are provided within square brackets in the figure. For a detailed explanation, please refer to the text.

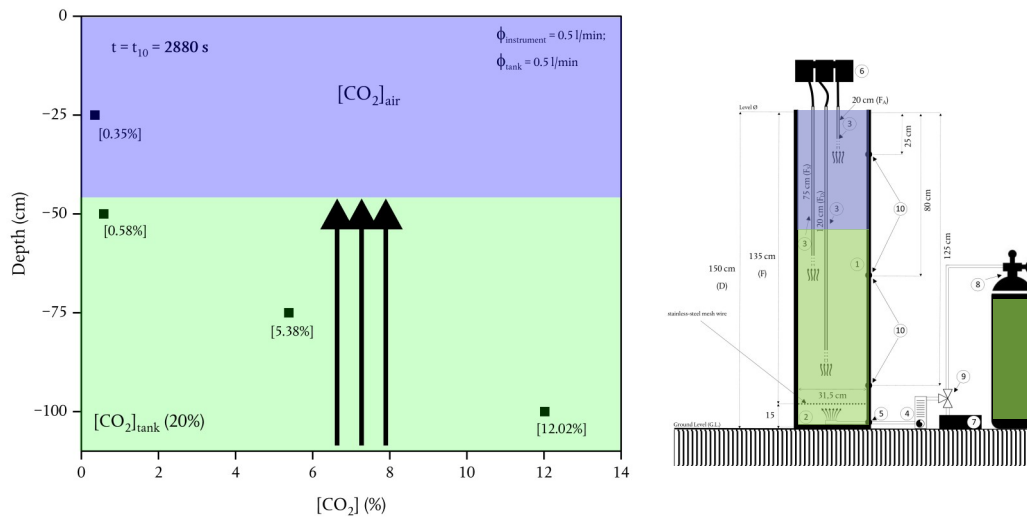


**Figure 5.11**— Diagram [CO<sub>2</sub>] vs Depth. This diagram depicts the upward propagation of a gas mixture enriched with CO<sub>2</sub> [20%]. The purple-colored area represents the CO<sub>2</sub> presence in the IEA (denoted in the Figure as [CO<sub>2</sub>]<sub>air</sub>), while the green-colored area signifies the CO<sub>2</sub> content in the gas tank (denoted in the Figure as [CO<sub>2</sub>]<sub>tank</sub>). The IEA is ideally positioned on the right side of the diagram. The gas propagates from the bottom to the top with a fixed gas flux. Figure 5.11 illustrates the system at  $t_{10}$ , corresponding to a time of 2880 seconds after the experiment started. The concentration values, expressed in percentages, are provided within square brackets in the figure. For a detailed explanation, please refer to the text.

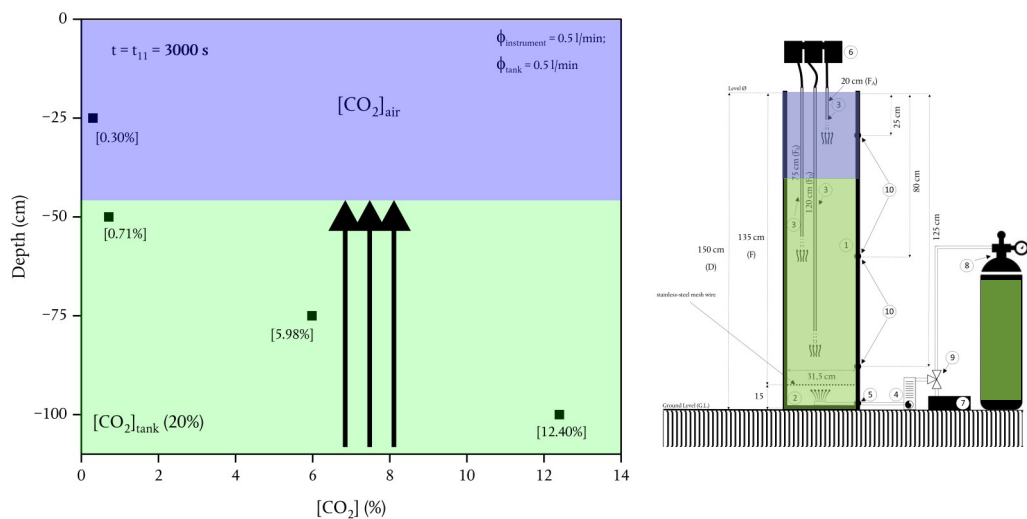


**Figure 5.12**— This diagram depicts the upward propagation of a gas mixture enriched with CO<sub>2</sub> [20%]. The purple-colored area represents the CO<sub>2</sub> presence in the IEA (denoted in the Figure as [CO<sub>2</sub>]<sub>air</sub>), while the green-colored area signifies the CO<sub>2</sub> content in the gas tank (denoted in the Figure as [CO<sub>2</sub>]<sub>tank</sub>). The IEA is ideally positioned on the right side of the diagram. The gas propagates from the bottom to the top with a fixed gas flux. Figure 5.12 illustrates the system at  $t_{11}$ , corresponding to a time of 3000 seconds after the experiment started. The concentration values, expressed in percentages, are provided within square brackets in the figure. For a detailed explanation, please refer to the text.

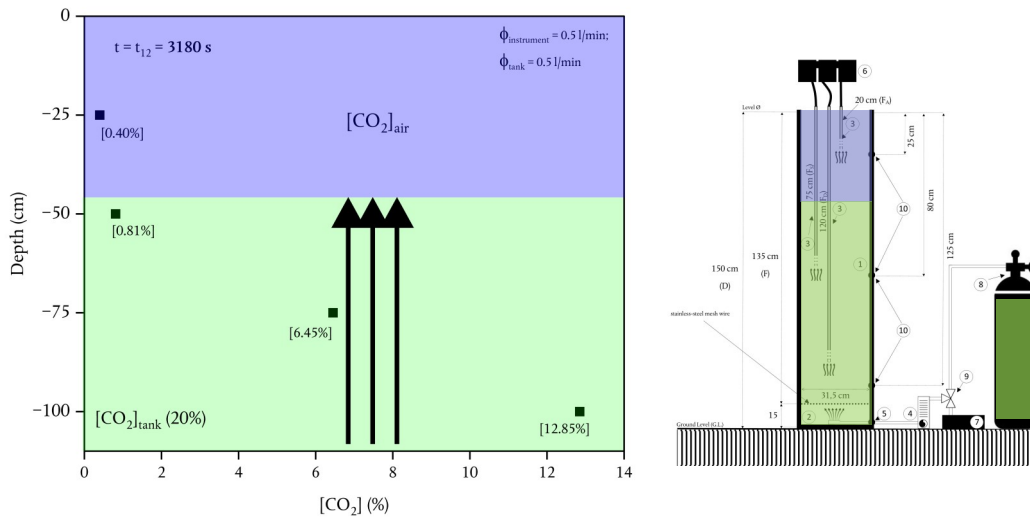


**Figure 5.13**— Diagram [CO<sub>2</sub>] vs Depth. This diagram depicts the upward propagation of a gas mixture enriched with CO<sub>2</sub> [20%]. The purple-colored area represents the CO<sub>2</sub> presence in the IEA (denoted in the Figure as [CO<sub>2</sub>]<sub>air</sub>), while the green-colored area signifies the CO<sub>2</sub> content in the gas tank (denoted in the Figure as [CO<sub>2</sub>]<sub>tank</sub>). The IEA is ideally positioned on the right side of the diagram. The gas propagates from the bottom to the top with a fixed gas flux. Figure 5.13 illustrates the system at  $t_{12}$ , corresponding to a time of 3180 seconds after the experiment started. The concentration values, expressed in percentages, are provided within square brackets in the figure. For a detailed explanation, please refer to the text.

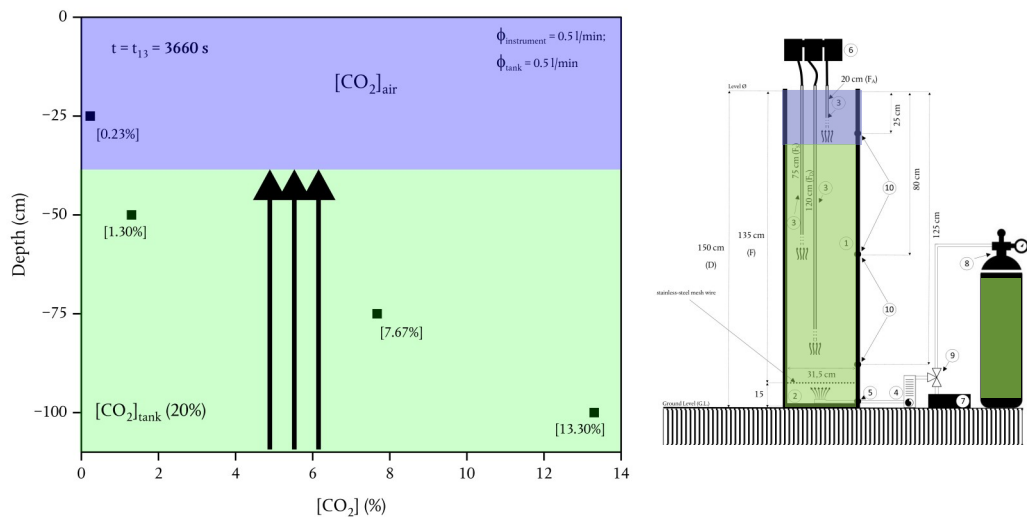


**Figure 5.14**— This diagram depicts the upward propagation of a gas mixture enriched with CO<sub>2</sub> [20%]. The purple-colored area represents the CO<sub>2</sub> presence in the IEA (denoted in the Figure as [CO<sub>2</sub>]<sub>air</sub>), while the green-colored area signifies the CO<sub>2</sub> content in the gas tank (denoted in the Figure as [CO<sub>2</sub>]<sub>tank</sub>). The IEA is ideally positioned on the right side of the diagram. The gas propagates from the bottom to the top with a fixed gas flux. Figure 5.14 illustrates the system at  $t_{13}$ , corresponding to a time of 3660 seconds after the experiment started. The concentration values, expressed in percentages, are provided within square brackets in the figure. For a detailed explanation, please refer to the text.

increases, while the CO<sub>2</sub> concentrations at 25 cm show the residual CO<sub>2</sub> concentration of [CO<sub>2</sub>]<sub>air</sub>.

At the time point  $t_{14}$  (Figure 5.15), a marginal increase in CO<sub>2</sub> concentration is observed at the depth of 25 cm. This observation indicates that at  $t_{14}$  (3900 seconds from system activation), the initial impact of the gas flux ( $\phi_{gas}$ ) with a CO<sub>2</sub> concentration of 20% is slightly perceptible at 25 cm depth.

At the time point  $t_{15}$  (Figure 5.16), the CO<sub>2</sub> concentrations at the depths of 25, 50, 75, and 100 cm are entirely influenced by gas fluxes ( $\phi_{gas}$ ) with a CO<sub>2</sub> concentration of 20%.

At the same time point  $t_{15}$ , it was conducted the collection of four samples at depths of 25, 50, 75, and 100 cm for the purpose of analyzing CO<sub>2</sub> and He concentrations through gas chromatography (gas chromatograph – Perkin Elmer Clarus 500 – equipped with a double detector (a thermal conductivity detector (TCD) and a flame ionization detector (FID), and Argon as the carrier gas).

The results of this analysis are documented in table 5.2. For enhanced elucidation of the increasing concentration patterns of CO<sub>2</sub> at various sampling depths, Figure 5.17 depicts the "[CO<sub>2</sub>] vs. t" relationships from  $t_0$  to  $t_{15}$ , with the concentrations at  $t_{15}$  denoting those analyzed via gas chromatography (table 5.2).

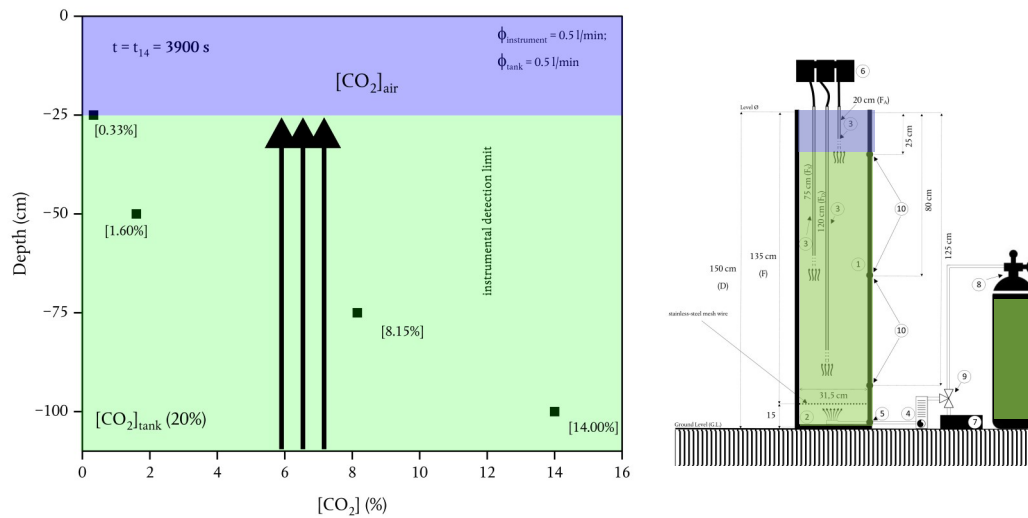


**Figure 5.15**— Diagram [CO<sub>2</sub>] vs. Depth. This diagram depicts the upward propagation of a gas mixture enriched with CO<sub>2</sub> [20%]. The purple-colored area represents the CO<sub>2</sub> presence in the IEA (denoted in the Figure as [CO<sub>2</sub>]<sub>air</sub>), while the green-colored area signifies the CO<sub>2</sub> content in the gas tank (denoted in the Figure as [CO<sub>2</sub>]<sub>tank</sub>). The IEA is ideally positioned on the right side of the diagram. The gas propagates from the bottom to the top with a fixed gas flux. Figure 5.15 illustrates the system at  $t_{14}$ , corresponding to a time of 3900 seconds after the experiment started. The concentration values, expressed in percentages, are provided within square brackets in the figure. For a detailed explanation, please refer to the text.

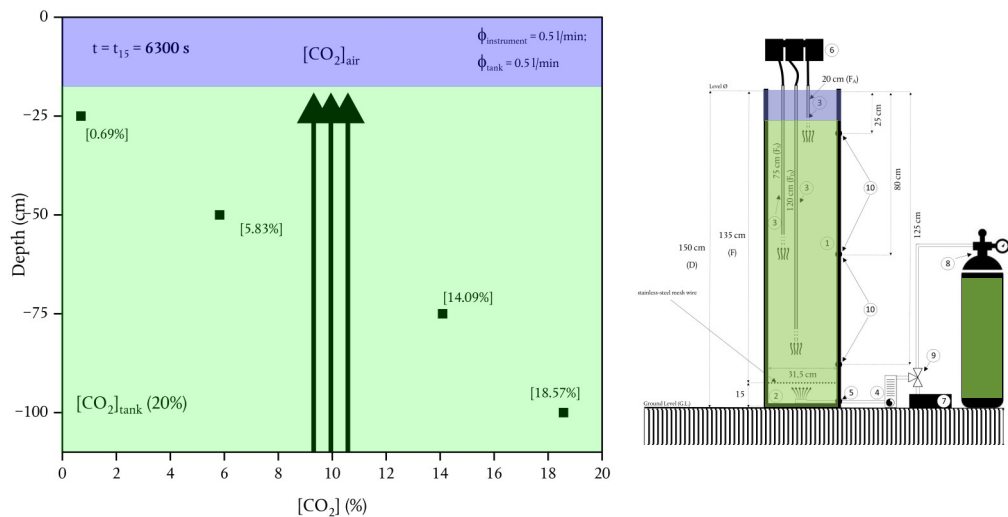


**Figure 5.16**— This diagram depicts the upward propagation of a gas mixture enriched with CO<sub>2</sub> [20%]. The purple-colored area represents the CO<sub>2</sub> presence in the IEA (denoted in the Figure as [CO<sub>2</sub>]<sub>air</sub>), while the green-colored area signifies the CO<sub>2</sub> content in the gas tank (denoted in the Figure as [CO<sub>2</sub>]<sub>tank</sub>). The IEA is ideally positioned on the right side of the diagram. The gas propagates from the bottom to the top with a fixed gas flux. Figure 5.16 illustrates the system at  $t_{15}$ , corresponding to a time of 6300 seconds after the experiment started. The concentration values, expressed in percentages, are provided within square brackets in the figure. For a detailed explanation, please refer to the text.

Additionally, Figure 5.18 provides a visual representation of the data in table 5.2, showing the typical diffusion path of CO<sub>2</sub> and He in porous media (Wu and Pruess, 2000; M. Camarda, Gurrieri and Valenza, 2006; Camarda *et al.*, 2007; Di Martino *et al.*, 2016).

Depth cm	[CO <sub>2</sub> ] %	[He] ppm
-25	0.72	58
-50	5.84	129
-75	14.50	192
-100	18.61	236

Table 5.2 – Concentrations of CO<sub>2</sub> and He determined in gas chromatography.

The diagram in Figure 5.19 illustrates the “ $\delta P$  vs  $t$ ” relationships from  $t_0$  to  $t_{15}$ , resembling the pattern depicted in Figure 4.15. It is evident that the pressure perturbations stem from the continuous gas flux ( $\phi_{gas}$ ) with a CO<sub>2</sub> concentration of 20%, set at 0.5 l/min, introduced into the system. The response time of both differential pressure sensors is less than one second, and the system reaches a steady-state at around 12 seconds ( $\delta P_{120}$ ) and 15 seconds ( $\delta P_{75}$ ).

The spectrometer detected variations in CO<sub>2</sub> concentration at approximately 420 seconds (100 cm depth), 900 seconds (75 cm depth), 2700 seconds (50 cm depth), and 3900 seconds (25 cm depth). The system exhibits an almost instantaneous response to pressure variations, while the classical geochemical monitoring system exhibits a longer response. In the hypothetical scenario of using toxic gas instead of CO<sub>2</sub>, it is evident how the experimental system's prompt

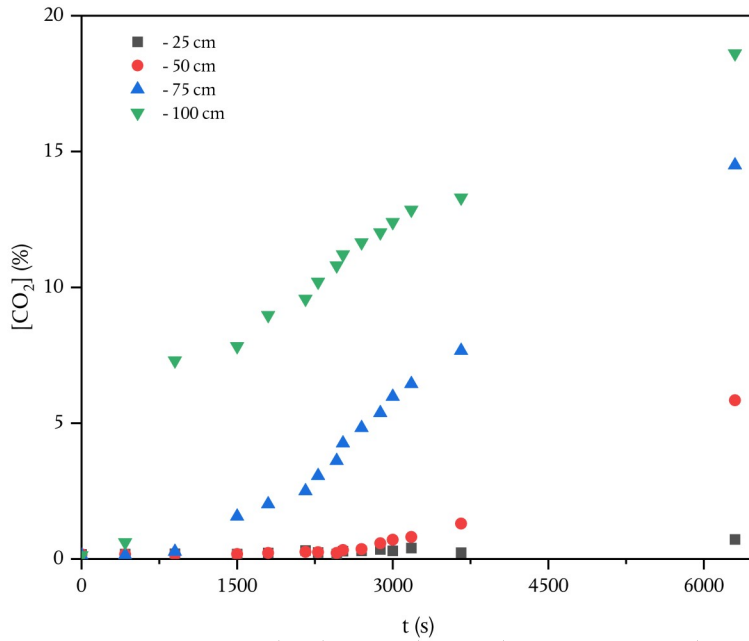


**Figure 5.17**— Diagram “[CO<sub>2</sub>] vs t”. This diagram depicts the “[CO<sub>2</sub>] vs. t” relationships from t<sub>0</sub> to t<sub>15</sub>, with the concentrations at t<sub>15</sub> denoting those analyzed via gas chromatography (table 5.2). For a detailed explanation, please refer to the text.

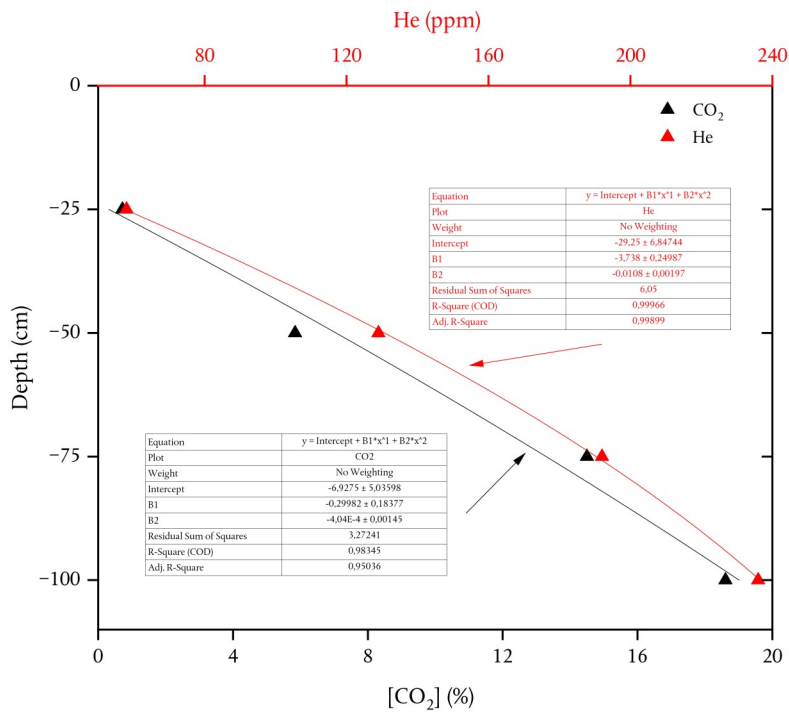


**Figure 5.18**— Double diagram [CO<sub>2</sub>]/[He] vs depth. Figure 5.18 provides a visual representation of the data in table 5.2, showing the typical diffusion path of CO<sub>2</sub> and He in porous media. For a detailed explanation, please refer to the text.

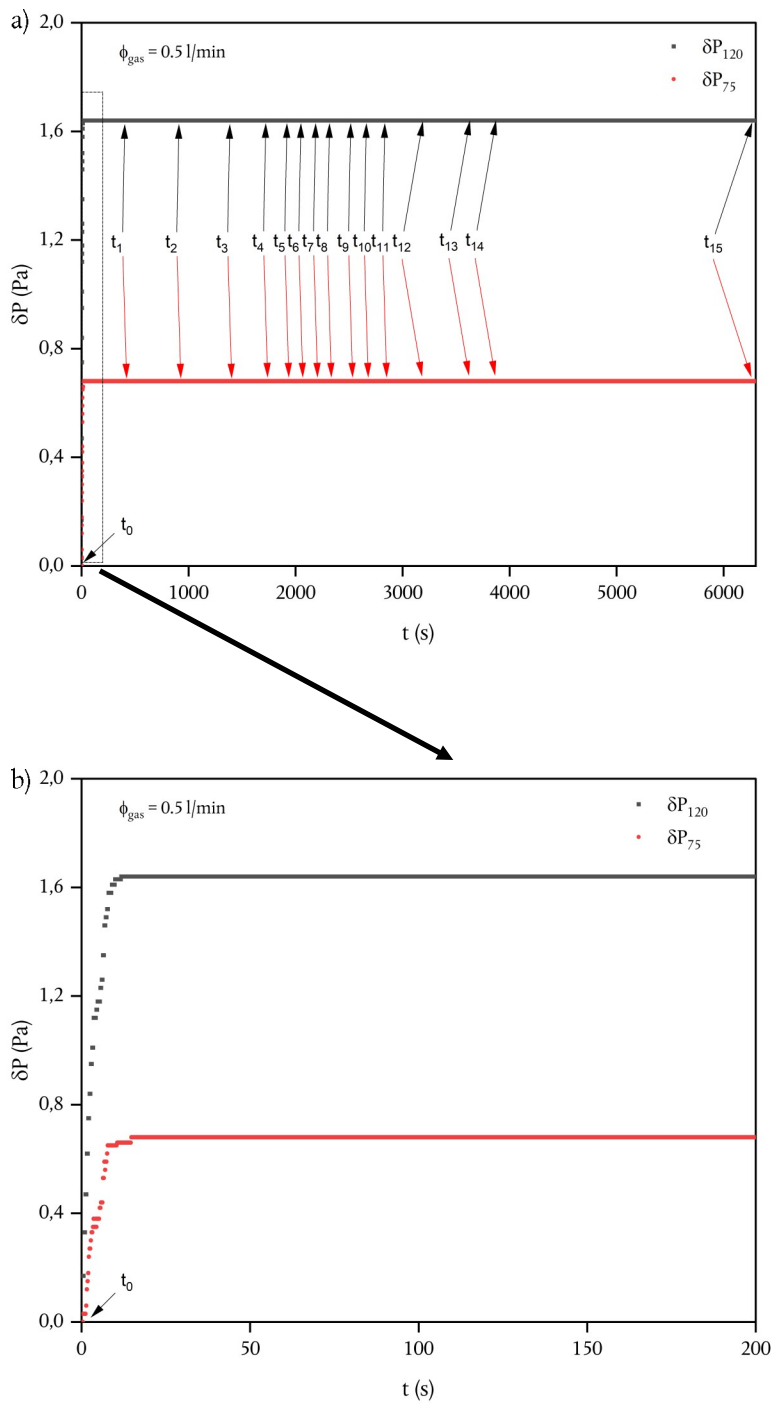


**Figure 5.19**— Diagram “ $\delta P$  vs  $t$ ” relationships from  $t_0$  to  $t_{15}$  a), This diagram illustrates the “ $\delta P$  vs  $t$ ” relationships from  $t_0$  to  $t_{15}$ , resembling the pattern depicted in Figure 4.15. It is evident that the pressure perturbations stem from the continuous gas flux ( $\phi_{\text{gas}}$ ) with a  $\text{CO}_2$  concentration of 20%, set at 0.5 l/min, introduced into the system. The response time of both differential pressure sensors is less than one second, and the system reaches a steady-state at around 12 seconds ( $\delta P_{120}$ ) and 15 seconds ( $\delta P_{75}$ ) b). For a detailed explanation, please refer to the text.



responsiveness could provide significant advantages in early warning applications.

The observable fluctuations in concentrations of volatile chemical species stem from intricate physical processes, as introduced in chapter 2, which exhibit relatively longer temporal scales than the pressure fluctuations under examination in this thesis. Deploying the experimental system in areas with well-defined degassing background would facilitate a comprehensive investigation of their temporal evolution. This can provide insights into the various mechanisms—such as seismogenic, volcanic, or others—that lead to the generation of these fluctuations.

## CHAPTER 6

### FIELD APPLICATIONS

---

#### Introduction

In this chapter, the results of soil-gas pressure fluctuations conducted using the FEA, introduced in the previous chapters, in a volcano-tectonics area of Sicily (Italy), will be discussed.

The FEA was deployed (Figure 6.1) along the terminating section of the so-called “1989 fissure” (Figure 6.2), situated at an elevation of around 1650 meters above sea level on the southern slope of Mount Etna (İçhedef *et al.*, 2020). This fissure, characteristic of a graben, was shaped by a shallow intrusion of magma during the flank eruption in September 1989.

Within this context, the FEA is positioned in a complex tectonic structure (Pezzo *et al.*, 2020) associated with volcano-tectonic (VT) seismicity and ground deformations on the upper part of the volcano (Neri, Acocella, *et al.*, 2011; Urlaub *et al.*, 2018).

#### Geological setting

Describing briefly the geological and geodynamical setting of the investigated site, it is worth noting that Mount Etna stands as one of the most active volcanoes globally. Currently, it presents four summit craters, namely Voragine (VOR), Northeast Crater (NEC), Bocca Nuova



Figure 6.1 - FEA installation.

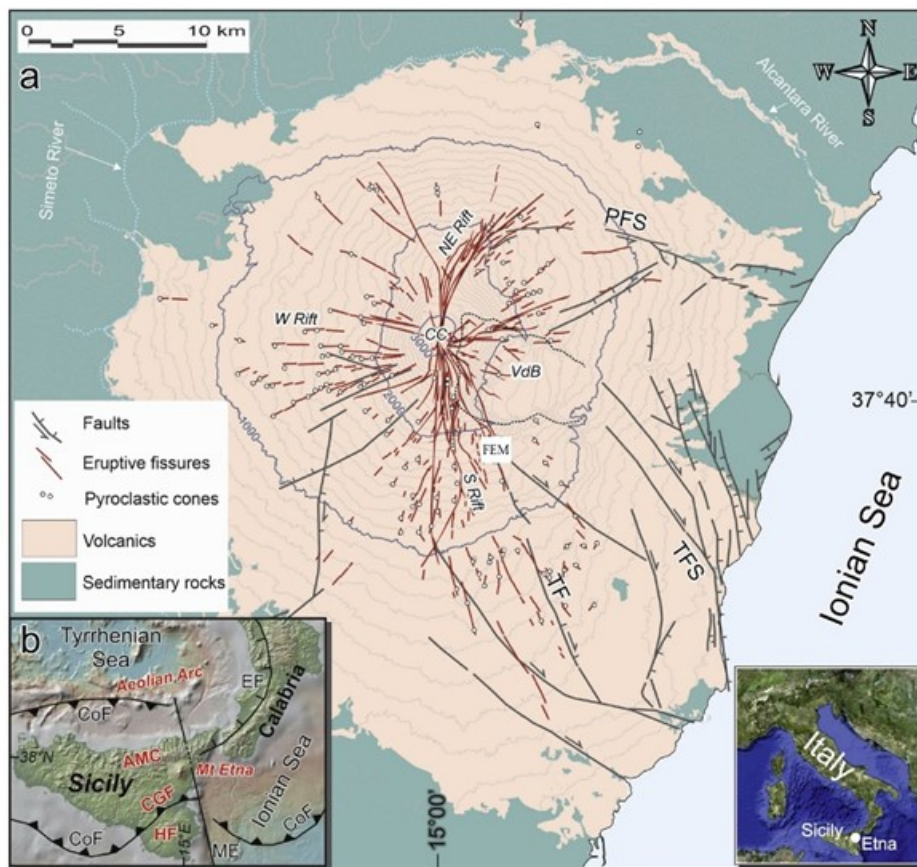


Figure 6.2 - Location of the FEA on Mt. Etna volcano: The main map (a) also shows the three main rift zones of the volcano (NE Rift, W Rift and S Rift, respectively) and the spatial distribution of main faults and eruptive fissures produced by flank eruptions in the last 2 ka. VB = Valle del Bove morphological depression. Regional tectonic context is shown in inset (b); AMC = Appennine-Maghrebian Chain; CGF = Gela-Catania foredeep; HF = Hyblean foreland; ME = Malta Escarpment; CoF = compressional front; EF = extensional front; Volcano-tectonic data of Mt. Etna modified from (İçhedef et al., 2020).

(BN), and Southeast Crater, the latter comprising an inactive cone (SEC) and an active cone established after 2011 (NSEC) (İçhedef *et al.*, 2020). Mount Etna consistently demonstrates high activity, characterized by a diverse range of volcanic phenomena occurring frequently throughout the year. Although it is nearly continuous, the summit activity does not pose a significant threat to human life and property (Cristi *et al.*, 2010). On the contrary, flank eruptions represent the most dangerous type of eruptive activity, since these occur closer to vulnerable areas, such as towns, villages, lifelines, and cultivated land (Cristi *et al.*, 2010). Etna is located at the edge of the Appenine-Maghrebian Chain, along the N-S trending extensional Malta escarpment, and it lies on Pliocene-Pleistocene foredeep deposits (Branca *et al.*, 2008; Groppelli and Norini, 2011; Azzaro *et al.*, 2012). Its tectonic setting is characterized by an overall E-W extension direction. Volcanism at Etna evolved from sporadic, predominantly subaerial and submarine, activity along fissures, with the development of several vents that are dispersed over a wide area (Branca *et al.*, 2008; Groppelli and Norini, 2011; Azzaro *et al.*, 2012). Finally, there was the construction of the present-day stratovolcano. Central stratovolcanoes like Etna are often characterized by summit and flank eruptions. Summit eruptions are the consequence of the ascent of magma from a reservoir through a central conduit (Branca *et al.*, 2008). Flank eruptions are commonly characterized by

multiple aligned vents that radiate from the summit of the volcano. Most of the observed flank eruptions at Etna originated from the central conduit: here, while the magma rises to often feed summit eruptions, at times it propagates laterally and downslope, to feed radial fissures and flank eruptions (Neri, Acocella, *et al.*, 2011). Sometimes, flank eruptions are not fed through the central conduit, but they are directly fed through new conduits from a reservoir beneath the volcano (Neri, Acocella, *et al.*, 2011). Volcanic flanks are capable of sliding due to internal and external forces. For instance, an unbalanced weight distribution of a volcanic structure and horizontal "pushing" caused by magma intrusions can induce flank spreading (Neri, Acocella, *et al.*, 2011). Unstable flanks can fail catastrophically, leading to massive landslides (Cristi *et al.*, 2010). There are several hypotheses regarding flank sliding at Mount Etna, including increased magma pressure, eruptive activity, repeated dyke intrusions, basement uplift, gravitational spreading, gravitational reorganization, gravity-driven instability accelerated by inflation and/or lateral intrusions, or combined magmatic inflation and continental margin instability. All these hypotheses are based on two fundamental processes that can trigger flank instability: horizontal pushing of rising magma intrusions or gravitational pull (Neri, Acocella, *et al.*, 2011; Urlaub *et al.*, 2018; Pezzo *et al.*, 2020).

The distribution of seismicity on Etna exhibits significant heterogeneity. As a general pattern, the hypocenter depth tends to increase from the east and east-southeast towards the northwest. Shallow seismic foci, with depths of less than 5 km, are common in the central part of the volcano, as well as on its eastern and southern slopes (Scarfi *et al.*, 2023). A similar pattern is observed for earthquakes with depths of approximately 5–10 km. Foci with depths ranging from 10 to 15 km are prevalent in the southwestern part of the area, as well as to the north and north-northeast of the summit craters, while deeper events (with depths in the range of 20–35 km) are located in the northwest section of the volcanic structure (Scarfi *et al.*, 2023). A discernible boundary between domains with shallow and deeper foci can be delineated, crossing the volcano from southwest to northeast and intersecting the summit region. The distribution of hypocenters reflects the interplay of local effects influenced by the volcano's dynamics and the broader tectonic framework of the region (Scarfi *et al.*, 2023). The extensive seismicity in the central sector suggests activity within the mid-shallow plumbing system, while the progressive increase in focal depth towards the northwest reflects crustal convergence beneath the thin volcanic covering. Specifically, beneath the volcano, there is evidence of northwestward subduction of the Hyblaean foreland crust below the fold and thrust system of the

southeast-verging Sicilian chain (Lavecchia *et al.*, 2007; Barreca *et al.*, 2014; De Guidi *et al.*, 2015; Scarfi *et al.*, 2023). Similarly, the abundance of hypocenters in the eastern sector mirrors the activation of the numerous faults characteristic of that flank, believed to be associated with a regional transtensional fault system extending offshore (Pezzo *et al.*, 2020; Scarfi *et al.*, 2023).

Prior to delving into the field results, it is essential to acknowledge that researches indicate how non-diffusive gas transport processes can significantly enhance diffusion-limited soil gas transport. In addition to the content conveyed in Chapter 3, air advection may be induced in highly porous surface layers by wind passing over rough surfaces (Hirsch, Trumbore and Goulden, 2004), particularly in regions with sparse vegetation where elevated wind speeds immediately above the ground may ensue. Additionally, advection may stem from the pressure-pumping effect (PPE) attributable to short-period atmospheric turbulence, protracted barometric alterations, and quasi-static pressure fields prompted by wind traversing uneven topography (Massman *et al.*, 1997). Barometric pressure-pumping customarily emanates from air pressure fluctuations of multiple tens of hectopascal (hPa) over a span of one to two days (Massman *et al.*, 1997; Stauffer *et al.*, 2019; Levintal *et al.*, 2020). Pressure-pumping due to pressure fields induced by wind traversing irregular topography has been observed

over a waste pile and terrain features comprising snow, such as dunes and ripples (Laemmel *et al.*, 2019). Moreover, pressure-pumping attributed to short-period atmospheric turbulence refers to air pressure oscillations with frequencies below 0.1 Hz that augment diffusion-limited soil gas transport (Massmann and Farrier, 1992; Mohr *et al.*, 2016).

The previously described phenomena do not conform to the typical degassing systems found in seismic or volcanic environments. Nonetheless, it is imperative to acknowledge that knowing and comprehending these phenomena is pivotal for accurately interpreting the acquired data. A comprehensive understanding of the environmental conditions at the sites where FEA-like devices could be installed is paramount for articulating numerical data with precision and meticulousness.

#### **Field experiments**

In the area where the FEA was installed, a CO<sub>2</sub> composition (at 50 cm depth) of approximately 2000 ppm was recorded, with a surface CO<sub>2</sub> flux of approximately 2.00 g/m<sup>2</sup>h. The soil CO<sub>2</sub> flux ( $\phi_{CO_2}$ ) measurement method, described by (Chiodini *et al.*, 1998; Giammanco *et al.*, 2007), were employed for the investigation by using an EGM-5 Portable CO<sub>2</sub> Gas Analyzer (PP Systems, Amesbury, USA).

Figures 6.3 to 6.5 depict three distinct representative sequences recorded during varying time spans, each characterized by differing



meteorological conditions. Unfortunately, there were no indications of specific seismic or explosive paroxysmal events during the observation periods. Figures 6.3 to 6.5 show the time series of atmospheric pressure,  $\delta P_{70}$  (the differential pressure ( $P_{70} - P_{\text{atm}}$ ) between the pressure recorded at a depth of 70 cm ( $P_{70}$ ) and the barometric pressure ( $P_{\text{atm}}$ )),  $\delta P_{25}$  (the differential pressure ( $P_{25} - P_{\text{atm}}$ ) between the pressure recorded at a depth of 25 cm ( $P_{25}$ ) and the barometric pressure ( $P_{\text{atm}}$ )), and  $\Delta_{(70-25)}$  (the difference between  $\delta P_{70}$  and  $\delta P_{25}$ ).

The initial sequence, featured as Figure 6.3 in this chapter, delineates a measurement conducted on August 30, 2024. The measurement recorded an average temperature of 30.4 °C and an average relative humidity of 38%. Figure 6.3 b) illustrates a pronounced negativity in  $\Delta_{(70-25)}$ , corresponding to a marked negativity in the  $\delta P_{70}$  (Figure 6.3 d)), while the  $\delta P_{25}$  (Figure 6.3 c)) exhibits maximum positivity. This observed behavior appears to be contingent upon the atmospheric pressure trend (see the salmon-colored area in Figure 6.3 a), b), c), and d)). As the temporal analysis progresses, the  $\Delta_{(70-25)}$  exhibits a progressive increase, occasionally resulting in a gradient inversion (see red arrows in Figure 6.3 b)). Despite the relatively modest magnitudes of these values, the green colored area in Figure 6.3 a), b), c), and d) appears to remain affected by the variation of the atmospheric pressure, punctuated by intermittent, likely biologically-induced

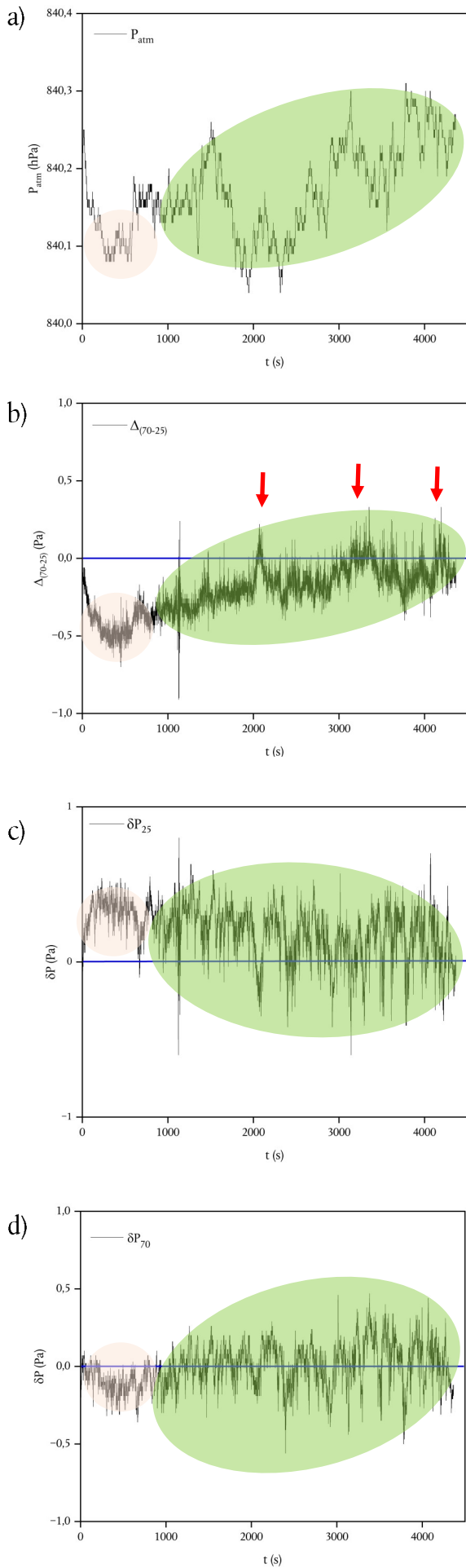
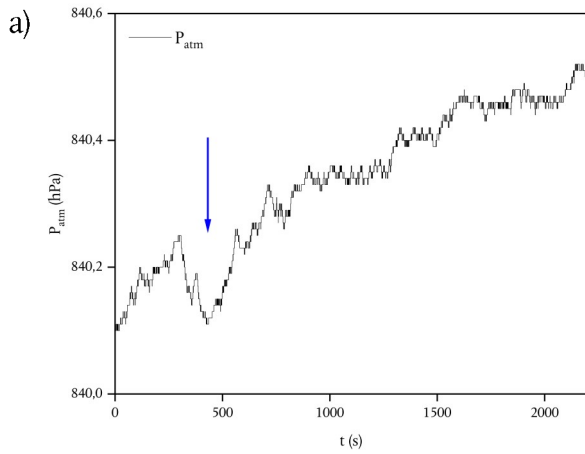


**Figure 6.3**— Field measurements conducted on August 30, 2024. Time series of atmospheric pressure (a),  $\Delta_{(70-25)}$  (b),  $\delta P_{25}$  (c),  $\delta P_{70}$  (d). The horizontal blue lines in b), c), and d) represent the hypothetical value 0 of  $\Delta_{(70-25)}$ ,  $\delta P_{25}$ , and  $\delta P_{70}$ , respectively. The sequence lasts approximately 4500 seconds. A salmon-colored area in a) represents a local minimum of atmospheric pressure that clearly influences the patterns of  $\Delta_{(70-25)}$  (b),  $\delta P_{25}$  (c), and  $\delta P_{70}$  (d). There is also a green-colored area indicating a slight increase in  $\Delta_{(70-25)}$  (refer to b)) that appears to be influenced by the general pattern of atmospheric pressure (refer to a)). Additionally, red arrows (refer to b)) indicate the positivity of  $\Delta_{(70-25)}$ . For a detailed explanation, please refer to the text.

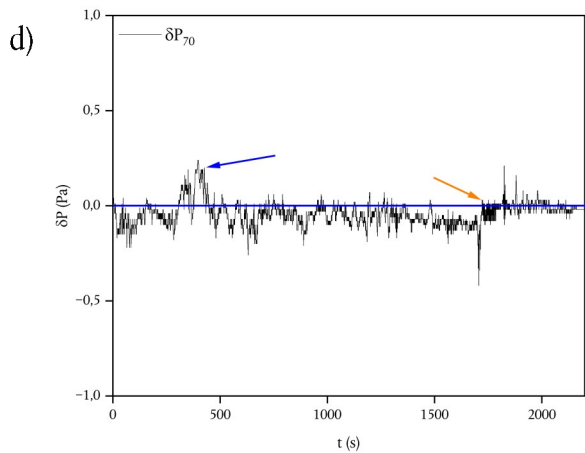
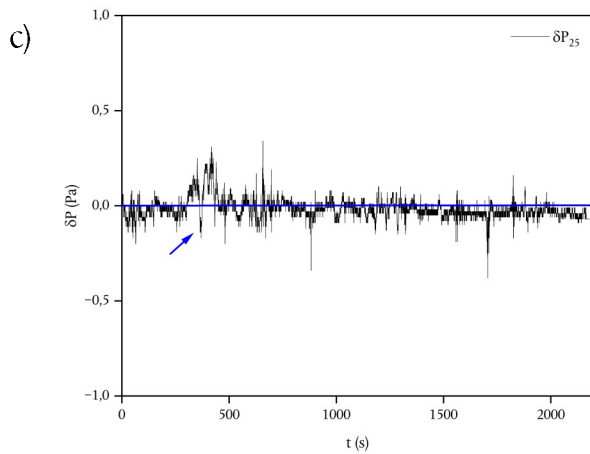
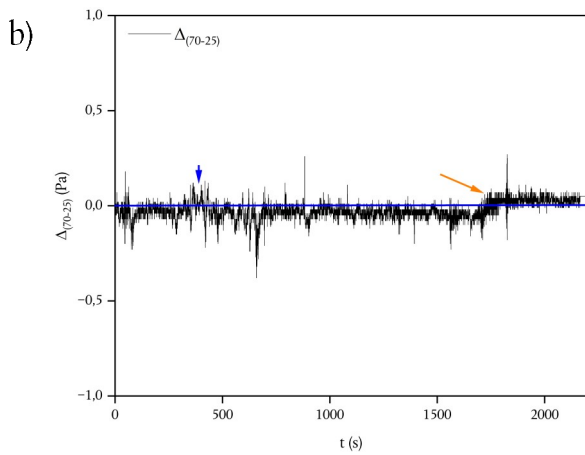
degassing events or atmospheric phenomena rather than those of tectonic or volcanic origin.

The sequence, featured as Figure 6.4 in this chapter, delineates a measurement conducted on August 31, 2024. The measurement recorded an average temperature of 26.8 °C and an average relative humidity of 58%. The measurements were conducted subsequent to the occurrence of rainfall, which resulted in a noteworthy decrease in soil permeability within the area. Apart from a slight positive peak in  $\Delta_{(70-25)}$  (indicated by the blue arrows in Figure 6.4 a), b), c), and d)), which corresponds to a minimum atmospheric pressure, the values appear to remain constant, suggesting a limitation in gas propagation due to the reduced soil permeability. The orange arrows in Figure 6.4 b) and d) denotes a sudden increase in the  $\delta P_{70}$ , resulting in a positive  $\Delta_{(70-25)}$ . Once again, it seems that the environmental conditions during the measurement recording do not facilitate the differentiation of various degassing phenomena.

The sequence, featured as Figure 6.5 in this chapter, delineates a measurement conducted on September 2, 2024. The measurement recorded an average temperature of 28.2 °C and an average relative humidity of 28.5%. Data gleaned from this series of measurements prove to be particularly intriguing. Continuously low values, similar to those observed in prior measurements, provide an opportunity to



**Figure 6.4**— Field measurements conducted on August 31, 2024. Time series of atmospheric pressure a),  $\Delta_{(70-25)}$  b),  $\delta P_{25}$  c),  $\delta P_{70}$  d). The horizontal blue lines in b), c), and d) represent the hypothetical value 0 of  $\Delta_{(70-25)}$ ,  $\delta P_{25}$ , and  $\delta P_{70}$ , respectively. The sequence lasts approximately 2300 seconds. Blue arrows (refer to a), b), c), and d)) indicate the influence of the atmospheric pressure to  $\Delta_{(70-25)}$  b),  $\delta P_{25}$  c),  $\delta P_{70}$  d). Orange arrows (refer to b) and d)) indicate a sudden increase of  $\Delta_{(70-25)}$  related to a synchronous increase of  $\delta P_{70}$ . For a detailed explanation, please refer to the text.



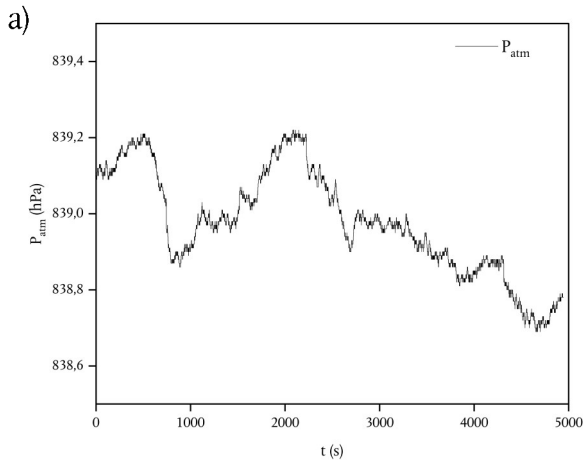
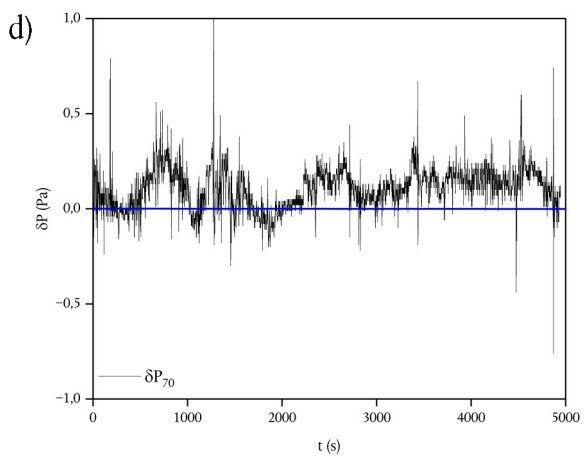
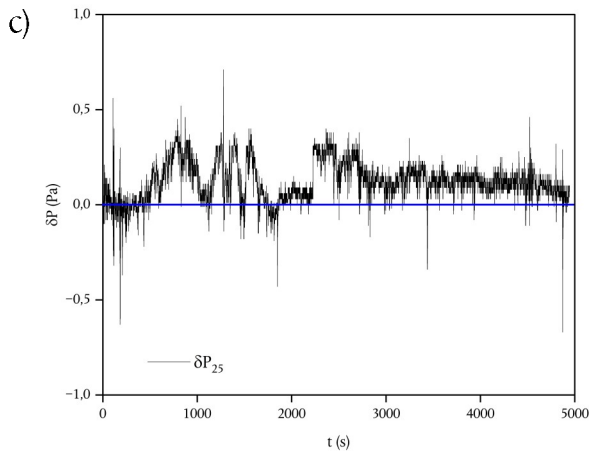
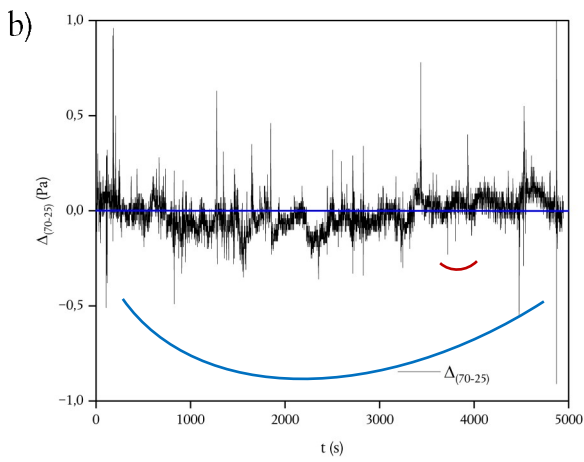


**Figure 6.5**— Field measurements conducted on September 2, 2024. Time series of atmospheric pressure (a),  $\Delta_{(70-25)}$  (b),  $\delta P_{25}$  (c),  $\delta P_{70}$  (d). The horizontal blue lines in b), c), and d) represent the hypothetical value 0 of  $\Delta_{(70-25)}$ ,  $\delta P_{25}$ , and  $\delta P_{70}$ , respectively. The sequence lasts approximately 5000 seconds. The blue curve (refer to b)) represents a hypothetical cyclicity of  $\Delta_{(70-25)}$ . The red curve (refer to b)) represents a hypothetical series of cyclicities of  $\Delta_{(70-25)}$ . For a detailed explanation, please refer to the text.



elucidate the FEA's capacity to discern minor fluctuations and emphasize recurring patterns undetectable by lower frequency sampling methods.

Figure 6.5 b) showcases the presence of two distinct cyclic trends in " $\Delta_{(70-25)}$  vs  $t$ " system. With a period of approximately 4500 seconds, a broader cycle (depicted by the blue curve in figure 6.5 b)) is discernible, alongside minor cycles featuring an average period of roughly 450 seconds (depicted by the purple areas in figure 6.5 b)). Although the broader cycle seems to concur with the overarching atmospheric pressure trend, minor cycles appear to operate independently of atmospheric pressure trends upon initial inspection. Notably, the current investigative phase abstains from ascertaining the origin of this cyclic behavior, and thus defers any conclusive determinations concerning its causation.

Given the synchronicity of the measurements of the differential pressure sensors, an assessment was conducted regarding the system's timeliness in responding to atmospheric pressure fluctuations. Specifically, a time interval from 1200 seconds to 1800 seconds of the sequence on August 30, 2024, was selected as illustrated in Figure 6.6. The parameters  $\delta P_{25}$  and  $\delta P_{70}$  were compared with atmospheric pressure, and blue dotted lines were used to correlate local maxima and minima of atmospheric pressure with the values of  $\delta P_{25}$  and  $\delta P_{70}$ . It was

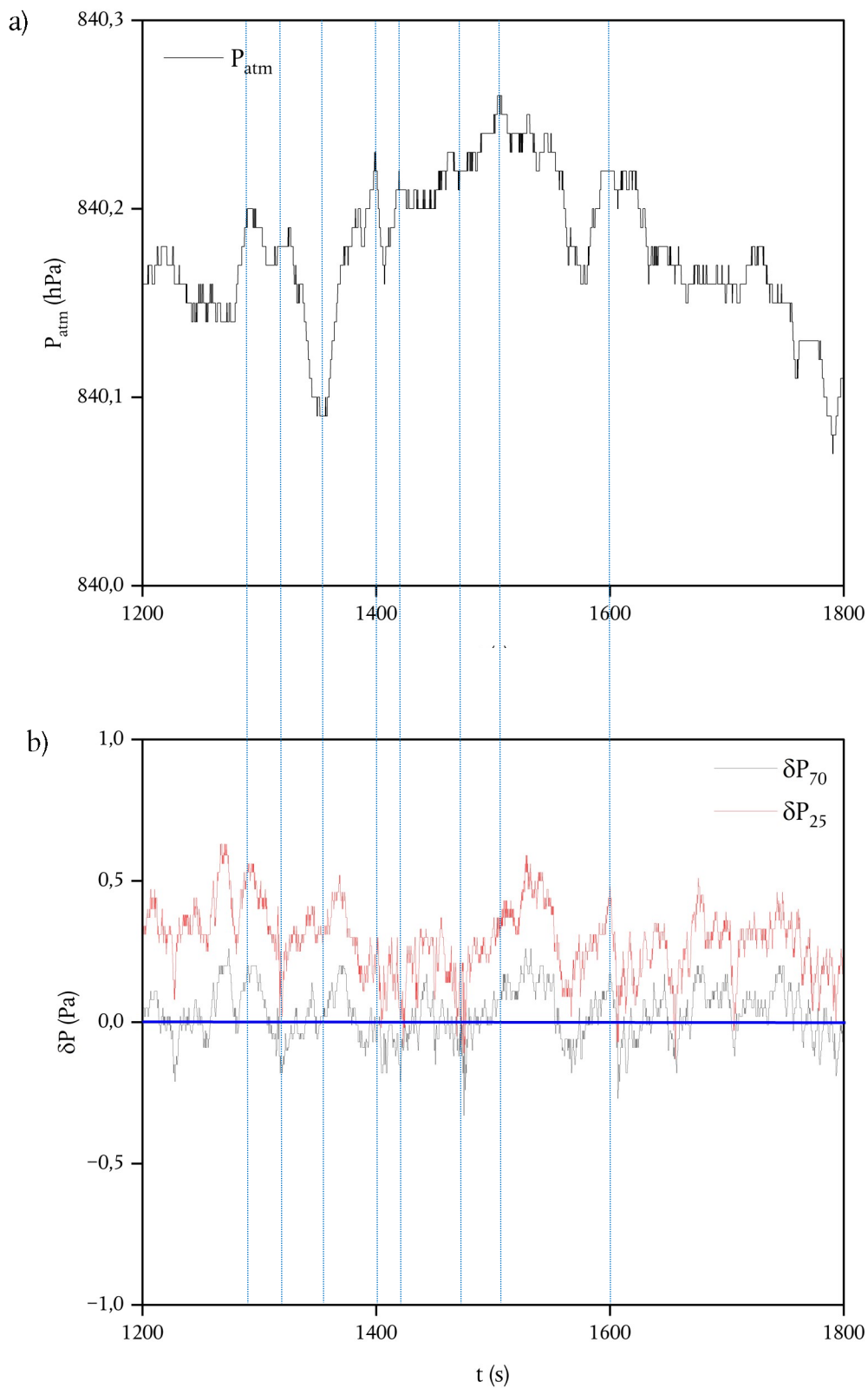


**Figure 6.6**— Particular of the field measurements conducted on August 30, 2024 in the time span between 1200 seconds and 1800 seconds. Time series of atmospheric pressure a) and  $\delta P_{25} / \delta P_{70}$  b). The horizontal blue line in b) represents the hypothetical value 0 of  $\delta P_{25}$  and  $\delta P_{70}$ . The blue dotted lines compare the local maxima and minima of atmospheric pressure with  $\delta P_{25}$  and  $\delta P_{70}$ . For a detailed explanation, please refer to the text.

observed that the fluctuations in the values of  $\delta P_{25}$  and  $\delta P_{70}$  appeared to be slightly advanced in time relative to the local maxima and minima of atmospheric pressure. This indicates that the FEA requires a certain amount of time to reach a steady state, aligning with the experimental laboratory data outlined in chapter 4.

FEA has demonstrated exceptional sensitivity in field tests, enabling the identification of short-term gas movement cycles. This capability is of paramount importance for interpreting geochemical data with significantly larger sampling intervals than the device used in this doctoral thesis. The initial goal of achieving precision comparable to seismological measurement methods appears to have been attained. However, analogous to seismological systems, the FEA is confronted with background noise issues. Understanding the site-specific nature of such noise is critical, as the measurements depend primarily on wind and on cultural noise, although the movement of water may also contribute. Notably, even in scenarios characterized by low permeability, the FEA has been observed to capture brief gas movement peaks — a phenomenon undetectable by traditional geochemical sampling methods.



## CHAPTER 7

### MITIGATING THE EFFECTS OF WIND ON THE MEASUREMENTS OF SOIL – GAS PRESSURE FLUCTUATIONS

---

#### Introduction

The preceding chapters have demonstrated how the heightened sensitivity of the experimental apparatuses outlined in this doctoral thesis effectively captures not only natural degassing occurrences but also other phenomena that have the potential to influence, if not overshadow, the measurements and observations being conducted.

Soil diffuse degassing constitutes a significant component of gas emissions from seismogenetic and volcanic systems (Allard *et al.*, 1991). According to literature data (Carapezza *et al.*, 2011; Lewicki and Hilley, 2014; Laiolo *et al.*, 2016; Boudoire *et al.*, 2017; Maier, Mayer and Laemmel, 2019; Morita *et al.*, 2019; J. Jiang, Hu, *et al.*, 2023), soil gas emissions are profoundly influenced by environmental parameters, including barometric pressure, air temperature, air humidity, soil temperature, soil humidity, rainfall, wind speed, and wind direction. Recent studies have revealed that, for instance, soil CO<sub>2</sub> flux variations are significantly influenced by soil conditions (such as soil temperature, soil humidity, and rainfall), as well as by air temperature and barometric

pressure (Boudoire *et al.*, 2017). Additionally, local wind conditions around the monitoring site can also impact soil CO<sub>2</sub> flux (Maier, Mayer and Laemmel, 2019; J. Jiang, Hu, *et al.*, 2023). It is also important to emphasize that the maximum distance at which pressure fluctuations produced by the wind action can transmit their influence within a soil column is directly linked to the physical properties of the soil and is highly correlated with soil permeability (J. Jiang, Gu, *et al.*, 2023).

**Differential  
pressure sensors**

Commencing from these essential premises and seeking to identify the seismic or volcanic phenomena influencing natural degassing, the inquiry arose as to whether it was feasible to mitigate the influence of environmental parameters by employing only a minimal set of external instruments and sensors not integral to the experimental apparatus under study.



Figure 7.1 – Connectors of the differential pressure sensors (D6F-PH0505AD3).

Each of the measurements conducted thus far occurs at the level of the differential pressure sensors (D6F-PH0505AD3). The differential pressure sensors comprise two connectors (see Figure 7.1), with one connected, via a silicone tube, to the capillary tube, providing pressure information at a specific depth, while the second connector registers atmospheric pressure. If the capillary tube is positioned at a depth denoted as D, the differential pressure measured is:

$$\delta P_D = P_D - P_{\text{atm}}$$

Through the utilization of a second differential pressure sensors connected to another capillary tube located at depth S ( $S < D$ ), the differential pressure measured is:

$$\delta P_S = P_S - P_{\text{atm}}$$

Through the process of data analysis, as introduced in Chapter 4, the parameter  $\Delta_{(D-S)}$  is determined by the difference between the measured values of  $\delta P_D$  and  $\delta P_S$ :

$$\Delta_{(D-S)} = \delta P_D - \delta P_S \text{ [Eq. 7.1]}$$

The parameter  $\Delta_{(D-S)}$  represents a calculated value derived from the measurements of  $\delta P_D$  and  $\delta P_S$ . Consequently, equation [Eq. 7.1] can be restated as follows:

$$\Delta_{(D-S)}^C = \delta P_D - \delta P_S \text{ [Eq. 7.2]}$$

It is clear that the connectors of the differential pressure sensors used for continuous measurement of atmospheric pressure are significantly influenced by natural phenomena related to wind action or variations in atmospheric pressure, such as the Venturi effect and increase/decrease of pressure gradients.

The utilization of cases to shield the differential pressure sensors from environmental influences is not feasible as it may lead to discrepancies in the continuous measurements of atmospheric pressure when compared to actual readings.

Returning to the simplified equation [eq. 4.9],

$$k_i = \frac{\mu\phi_{air}}{4\pi} \Psi \frac{1}{\Delta_{(120-75)}}$$

the intrinsic permeability is a function of  $\Delta_{(D-S)}$ , assuming that  $\delta P \ll P_{atm}$ . Therefore, the sole parameter requiring measurement is  $\Delta_{(D-S)}$ .

It is feasible to directly measure the value of  $\Delta_{(D-S)}$ . This can be achieved by utilizing a third differential pressure sensor (D6F-PH0505AD3) and connecting a second couple of capillary tubes to the two connectors, enabling the acquisition of a measured value for  $\Delta_{(D-S)}$ , denoted as  $\Delta_{(D-S)}^M$ .

In instances where surface environmental phenomena that impact atmospheric pressure are absent, and the presence of deep non-

volcanic or seismogenic environmental phenomena are neglectable, both the measured and calculated values are found to be equivalent.

$$\Delta_{(D-S)}^M = \Delta_{(D-S)}^C$$

On the contrary,

$$\Delta_{(D-S)}^M \neq \Delta_{(D-S)}^C$$

**Field experiment** On September 10, 2024, a field experiment was executed to validate the earlier discourse. The designated site for this experiment differed from the location specified in the preceding chapter 6. The new site, situated in the “North-East rift” of Mount Etna (refer to Figure 7.2), has geographical coordinates of 37° 46' 52.0 N and 15° 00' 32.5 E. This location is positioned within an eruptive fissure and still exhibits significant water vapor emissions and heightened CO<sub>2</sub> fluxes. The site is situated at an elevation of approximately 2500 meters and is characterized by frequent winds. Furthermore, the site is devoid of CO<sub>2</sub> of biological origin. Throughout the experiment, the recorded temperature was 13°C, accompanied by a relative humidity of around 70%. The soil was found to be wet.

**Geological setting** The NE-Rift is a significant area of volcanic activity on Mount Etna. It consists of a network of eruptive fissures running from 42°E to 47°E and with dispersion axes ranging from 15°E to 62°E (Branca, Carbone and Greco, 2003). These fissures are clustered in a restricted

area about 2 km wide, extending from 2500 m down to 1700 m above sea level. In the upper part of the volcano, this fissure system runs north and is almost entirely covered by historic lava flows originating from the North-East Crater (NEC) (Branca, Carbone and Greco, 2003).

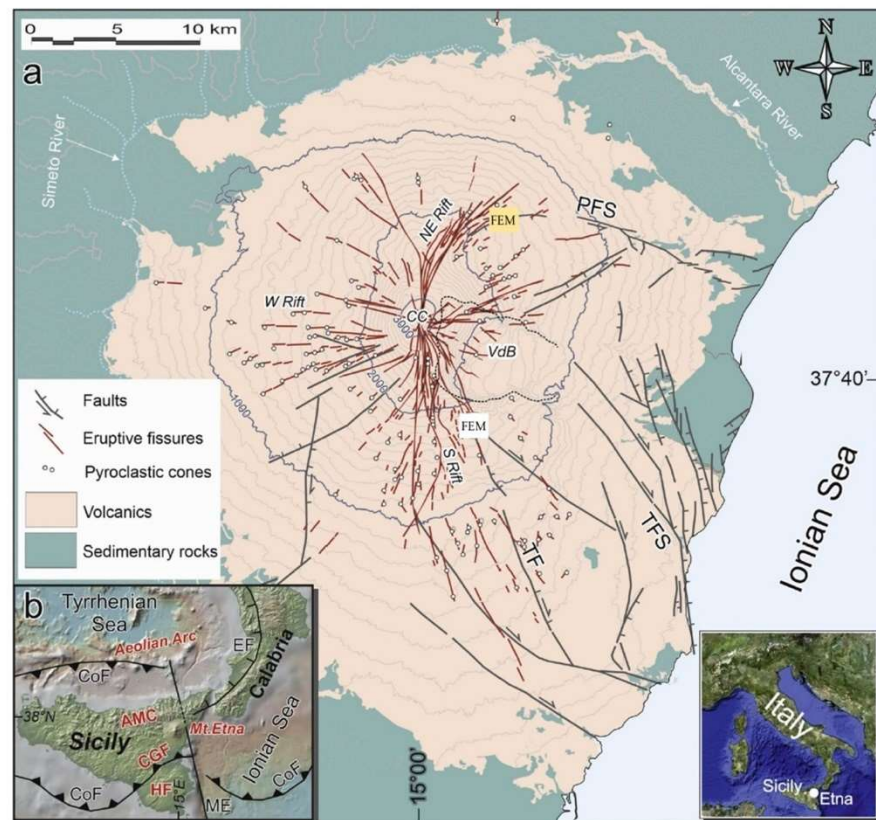
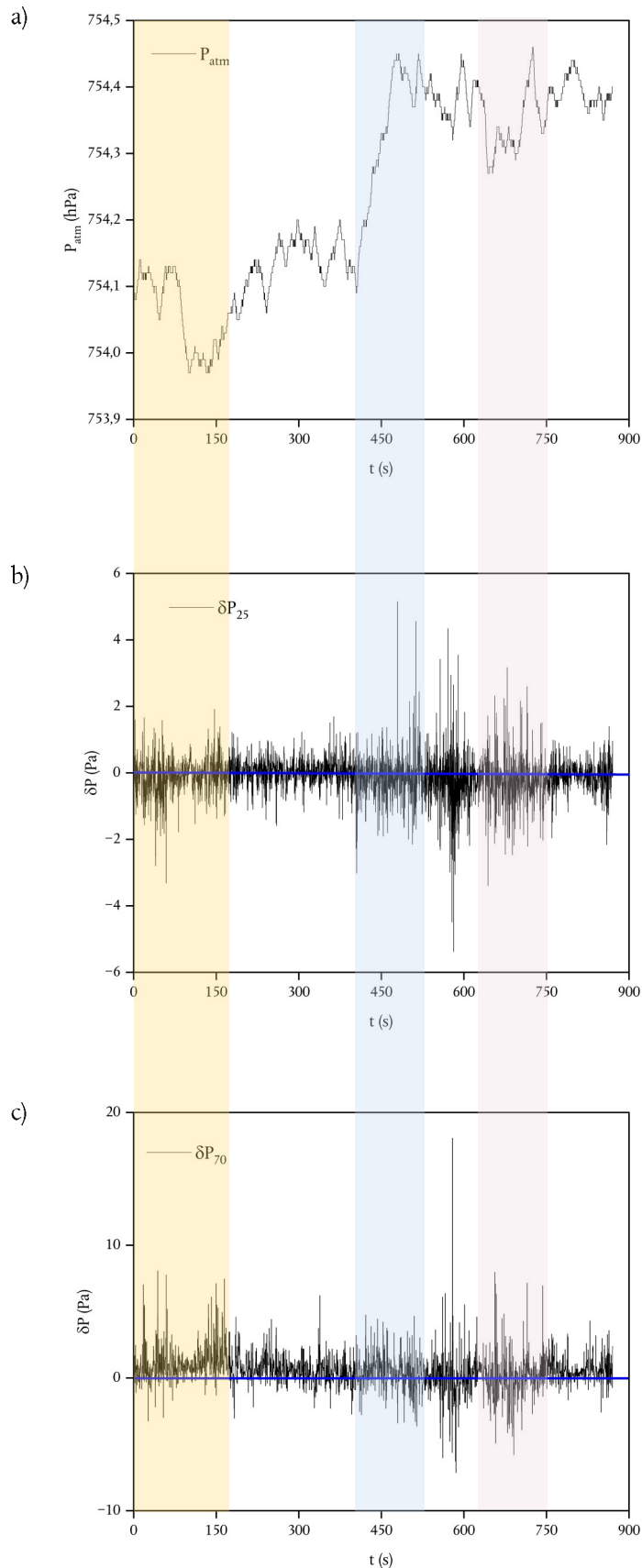


Figure 7.2 - Location of the FEMs on Mt. Etna volcano: The main map (a) also shows the three main rift zones of the volcano (NE Rift, W Rift and S Rift, respectively) and the spatial distribution of main faults and eruptive fissures produced by flank eruptions in the last 2 ka. The white—colored rectangular denoted as FEM is the site where the measurement made on August 30, August 31, and September 2, 2024 is located. The yellow—colored rectangular denoted as FEM is the site where the measurement made on September 10, 2024 is located. VB = Valle del Bove morphological depression. Regional tectonic context is shown in inset (b); AMC = Appennine-Maghrebian Chain; CGF = Gela-Catania foredeep; HF = Hyblean foreland; ME = Malta Escarpment; CoF = compressional front; EF = extensional front; Volcano-tectonic data of Mt. Etna modified from (İçhedef et al., 2020).

The NE-Rift is affected by strong extensional tectonics and is bordered to the east by the Provenzana fault and the Pernicana fault system (Branca, Carbone and Greco, 2003). They are considered discrete segments of a nearly continuous left-lateral shear zone dissecting the northeast flank of the volcano. Several authors have suggested that this significant extension is controlled by the gravitational collapse toward the southeast, involving the eastern flank of Etna (Branca, Carbone and Greco, 2003; Monaco *et al.*, 2005). Eruptive events along the NE-Rift over the last 300 years are characterized by short duration and relatively low volume of erupted lava. The onset of eruptions is preceded by seismic sequences, marking the opening of several kilometers-long fissure systems that develop from the base of the summit craters down to the NE-Rift zone. Typically, a high effusion rate characterizes the early phase of eruptions, allowing the lava flow to reach its maximum length in just a few days. Following this, the gradual decrease in the effusion rate mainly produces superimposition processes of the lava flow and minor movement of the lava front. Consequently, a lava flow field with a low width/length ratio is formed (Branca, Carbone and Greco, 2003).

#### Results and discussion

Figure 7.3 depicts the sequence recorded during field experiment introduced in this chapter. In particular, Figure 7.3 shows the time series of atmospheric pressure,  $\delta P_{70}$  (the differential pressure ( $P_{70} - P_{atm}$ ))



**Figure 7.3**— Field measurements conducted on September 10, 2024. The time series data includes atmospheric pressure a),  $\delta P_{25}$  b), and  $\delta P_{70}$  c). The horizontal blue lines in b) and c) represent the hypothetical value 0 of  $\delta P_{25}$  and  $\delta P_{70}$ , respectively. The sequence lasts approximately 900 seconds. The atmospheric pressure ranges between 753.9 hPa and 754.5 hPa. It is noticeable that the atmospheric pressure suddenly increases around 450 seconds into the time sequence. The yellow-colored rectangular area is the close-up reported in Figure 7.4. The azure-colored rectangular area is the close-up reported in Figure 7.5. The pink-colored rectangular area is the close-up reported in Figure 7.6. For a detailed explanation, please refer to the accompanying text.



between the pressure recorded at a depth of 70 cm ( $P_{70}$ ) and the barometric pressure ( $P_{\text{atm}}$ ),  $\delta P_{25}$  (the differential pressure ( $P_{25} - P_{\text{atm}}$ )) between the pressure recorded at a depth of 25 cm ( $P_{120}$ ) and the barometric pressure ( $P_{\text{atm}}$ ), as introduced in this chapter.

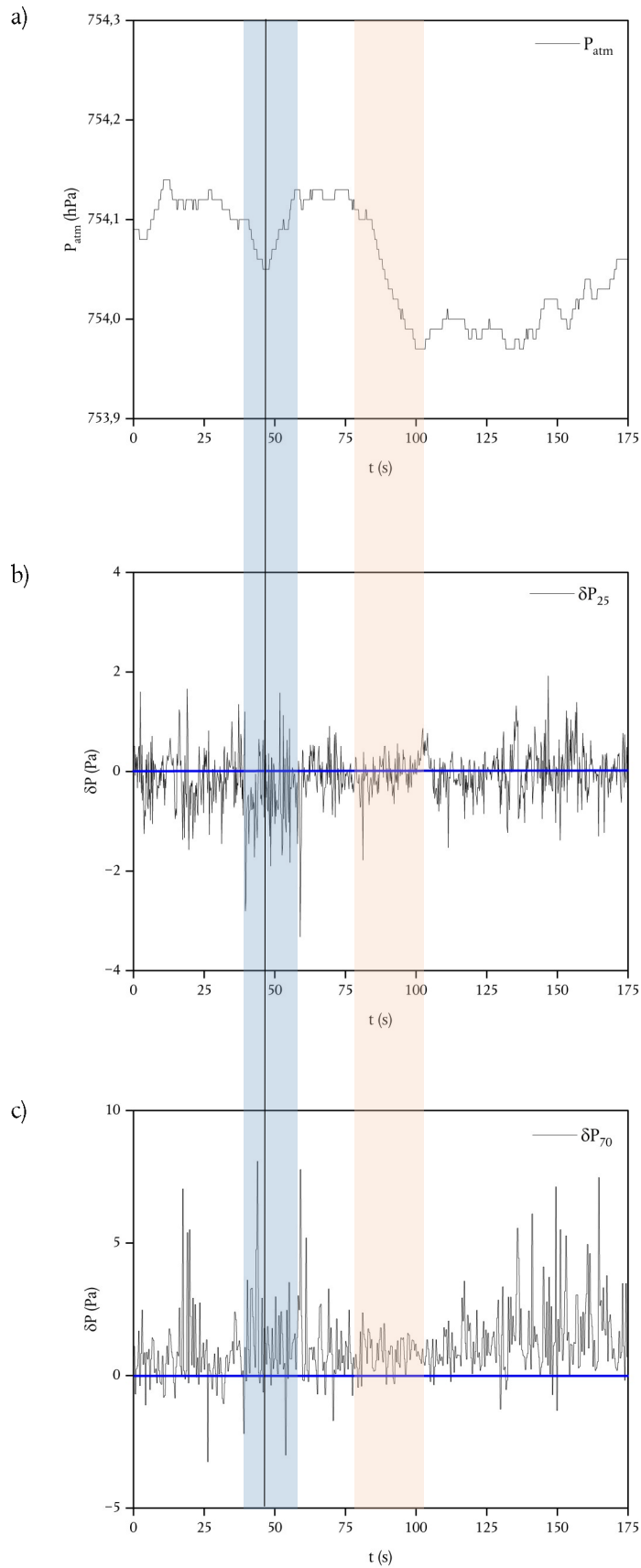
As already repeated in other parts of this doctoral thesis, it is pertinent to highlight that atmospheric pressure is typically quantified in hectopascals (hPa), while differential pressure parameters ( $\Delta_{(D-S)}^C$ ,  $\Delta_{(D-S)}^M$ ,  $\delta P_{25}$ , and  $\delta P_{70}$ ) are expressed in pascals (Pa). Even minute changes as small as hundredths of a pascal are routinely measured by the differential pressure sensors. Therefore, variations in atmospheric pressure of tens of a pascal are translated to fluctuations of hundredths of a pascal in the differential pressure parameters that the sensors can accurately discern. As a result, graphic representations do not always effectively convey the impact of factors, such as meteorological conditions, on differential pressure parameters.

Upon initial review, the graphs in Figures 7.3 b) and c) appear to exhibit no discernible correlation with atmospheric pressure variations in Figure 7.3 a). This apparent absence of correlation can be ascribed, in part, to the predominant influence of wind action on the parameters  $\delta P_{25}$  and  $\delta P_{70}$ . Nonetheless, by selectively close – ups into specific reference areas and conducting comparative analyses of distinct parameters, it becomes possible to delineate certain specific

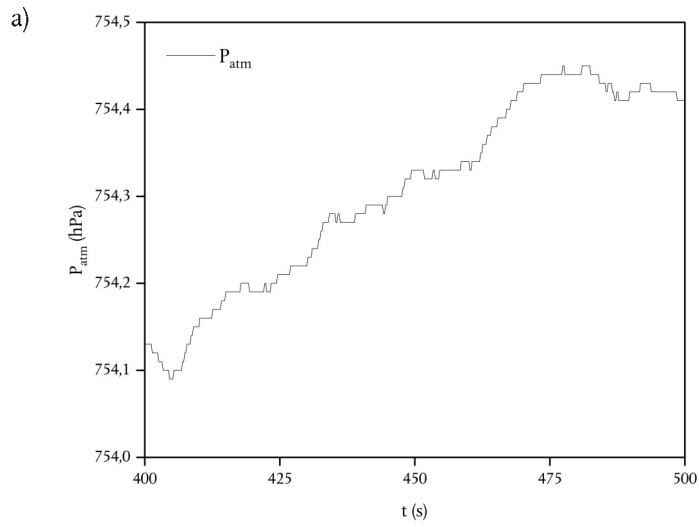
correlations. These insightful observations are explicated in Figures 7.4, 7.5, and 7.6.

Figure 7.4 depicts the close-up of the time span 0 – 175 seconds reported in the yellow—colored rectangular area in Figure 7.3. Two areas are being highlighted. The first area, indicated by the light blue – colored rectangle, shows a local minimum of atmospheric pressure (Figure 7.4 a)). However, this does not cause significant variations in the parameters  $\delta P_{25}$  and  $\delta P_{70}$  (Figure 7.4 b) and c)). The black line also shows that the local minimum does not correspond to any particular peaks, whether negative or positive, in the aforementioned parameters. The second area, indicated by the salmon – colored rectangle, highlights a sudden drop in atmospheric pressure of about 20 pascals (Figure 7.4 a)), which does not correspond to any variation in the patterns of  $\delta P_{25}$  and  $\delta P_{70}$  (Figure 7.4 b) and c)). The saw-shaped trend of the parameters  $\delta P_{25}$  and  $\delta P_{70}$  (Figure 7.4 b) and c)) is most likely linked to the influence of the wind and the Venturi effect.

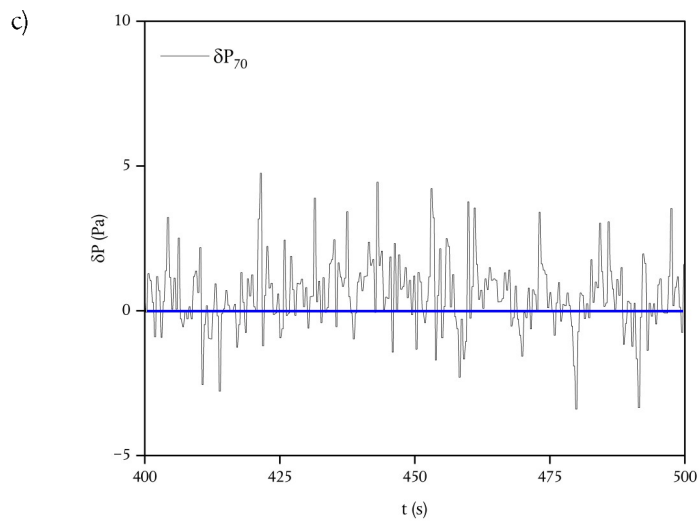
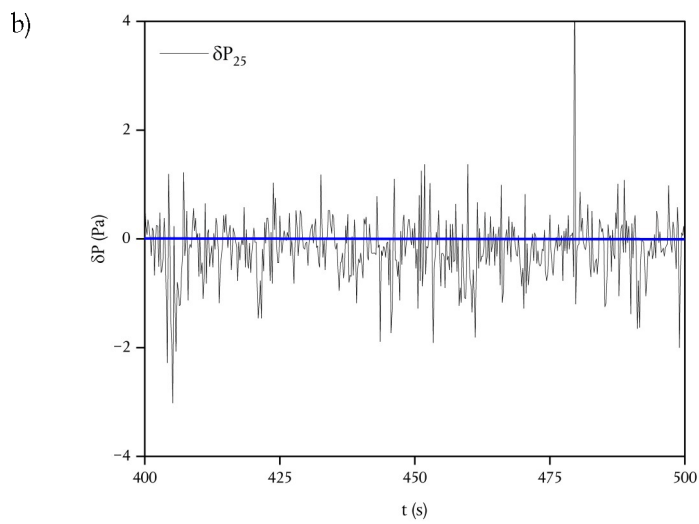
Figure 7.5 depicts the close-up of the time span 400 – 500 seconds reported in the azure—colored rectangular area in Figure 7.3. In the presence of an approximate 30 Pascal increase in atmospheric pressure (Figure 7.5a), parameters  $\delta P_{25}$  and  $\delta P_{70}$  (Figure 7.5 b) and c)) exhibit a sustained constancy over time. Furthermore, the periodic nature of the parameters  $\delta P_{25}$  and  $\delta P_{70}$  appears to stem from the influence of wind or,



**Figure 7.4**— Field measurements conducted on September 10, 2024. The time series data includes atmospheric pressure a),  $\delta P_{25}$  b), and  $\delta P_{70}$  c) in the time span of 0-175 seconds. The horizontal blue lines in b) and c) represent the hypothetical value 0 of  $\delta P_{25}$  and  $\delta P_{70}$ , respectively. The light blue—colored rectangular area show a local minimum of atmospheric pressure compared with the value of  $\delta P_{25}$  and  $\delta P_{70}$ . The salmon—colored rectangular area show a sudden drop (around 20 Pa) of atmospheric pressure compared with the value of  $\delta P_{25}$  and  $\delta P_{70}$ . For a detailed explanation, please refer to the accompanying text.



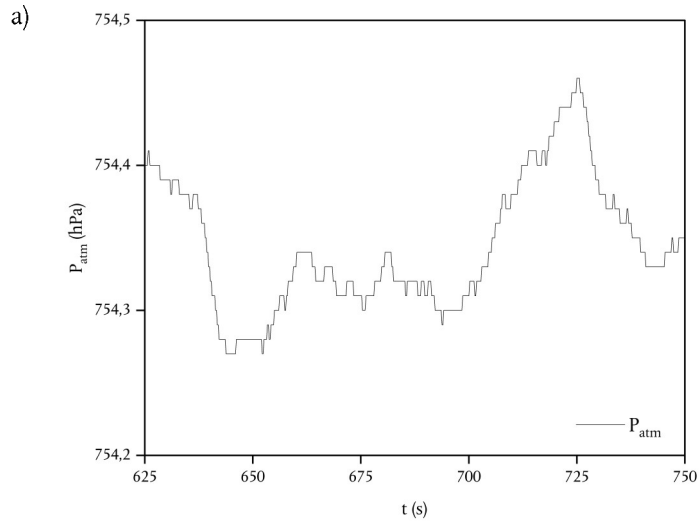
**Figure 7.5**— Field measurements conducted on September 10, 2024. The time series data includes atmospheric pressure a),  $\delta P_{25}$  b), and  $\delta P_{70}$  c) in the time span of 400-500 seconds. The horizontal blue lines in b) and c) represent the hypothetical value 0 of  $\delta P_{25}$  and  $\delta P_{70}$ , respectively. For a detailed explanation, please refer to the accompanying text.



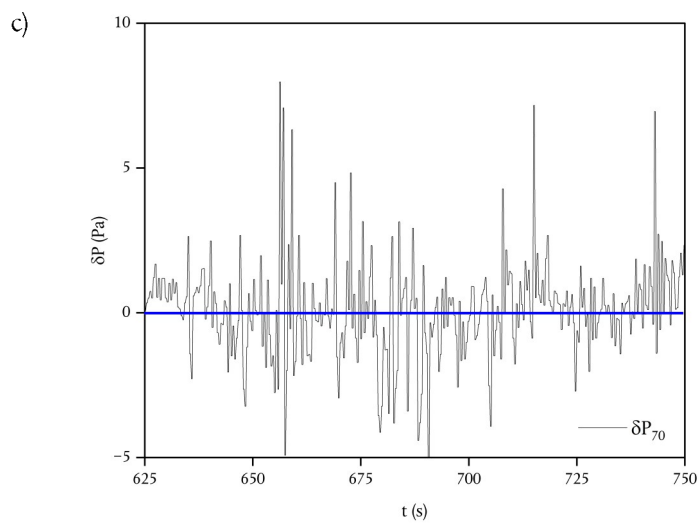
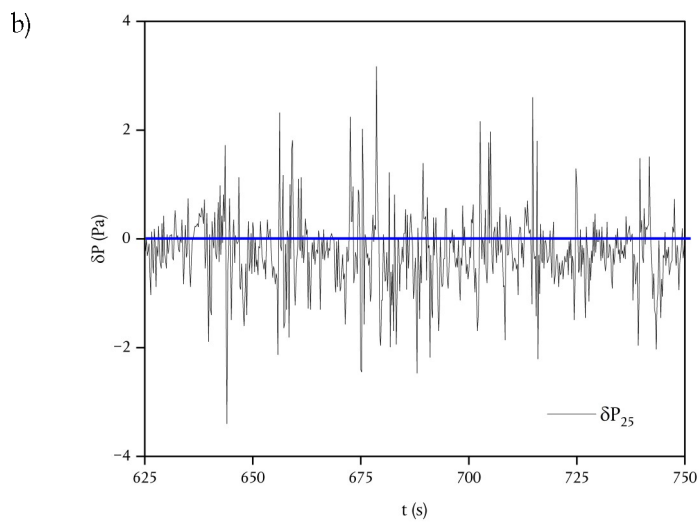
in instances where the parameters closely approach the sensors' threshold value of 0.01 Pa, from instrumental discrepancies.

Figure 7.6 depicts the close-up of the time span 625 – 750 seconds reported in the pink—colored rectangular area in Figure 7.3. During the specified time span, parameters  $\delta P_{25}$  and  $\delta P_{70}$  (Figure 7.6 b) and c)) demonstrate a densely fluctuating saw-shaped pattern, occasionally reaching peak values of approximately 5 Pa and -5 Pa for parameter  $\delta P_{70}$ . These peaks, regardless of their polarity, endure for approximately 3 seconds. However, this fluctuation does not appear to be associated with the pressure trend, which remains relatively constant despite pressure oscillations of approximately 10 Pa. Again, on this occasion, the observation is markedly more apparent, the periodic nature of the parameters  $\delta P_{25}$  and  $\delta P_{70}$  appears to stem from the influence of wind or, in instances where the parameters closely approach the sensors' threshold value of 0.01 Pa, from instrumental discrepancies.

The just observed data sequences underscore the impact of wind action and the subsequent rapid fluctuations in pressure on data seemingly unrelated to natural degassing processes and from atmospheric pressure variations. In light of this, the initial discourse on parameters  $\Delta_{(D-S)}^M$  and  $\Delta_{(D-S)}^C$  in the early section of this chapter can be applied to the discussed sequences. This approach will enable an



**Figure 7.6**— Field measurements conducted on September 10, 2024. The time series data includes atmospheric pressure a),  $\delta P_{25}$  b), and  $\delta P_{70}$  c) in the time span of 625-750 seconds. The horizontal blue lines in b) and c) represent the hypothetical value 0 of  $\delta P_{25}$  and  $\delta P_{70}$ , respectively. For a detailed explanation, please refer to the accompanying text.



ascertainment of the validity of the earlier deductions pertaining to themes related to the Figures 7.3, 7.4, 7.5, and 7.6.

Figure 7.7 shows the time series of the parameters  $\Delta_{(D-S)}^C$  (referred to as “ $\Delta_{(70-25)}$  calculated” in the Figure 7.7) and  $\Delta_{(D-S)}^M$  (referred to as “ $\Delta_{(70-25)}$  measured” in the Figure 7.7). The findings clearly display markedly diverse patterns for the parameters  $\Delta_{(D-S)}^M$  and  $\Delta_{(D-S)}^C$ . The saw-shaped pattern of parameter  $\Delta_{(D-S)}^C$  (Figure 7.7 a)) appears to confirm the findings for parameters  $\delta P_{25}$  and  $\delta P_{70}$ , which seem strongly influenced by the wind action.

In Figure 7.7 b), the parameter  $\Delta_{(D-S)}^M$  shows consistently positive values (indicating  $\delta P_{70} > \delta P_{25}$ ) of around 0.2 Pa, which corresponds to an upward pressure gradient. The magnitudes of the parameters  $\Delta_{(D-S)}^C$  and  $\Delta_{(D-S)}^M$  are also quite significant. It is clear that the parameter  $\Delta_{(D-S)}^C$  is one or two orders of magnitude larger than the parameter  $\Delta_{(D-S)}^M$ . The results align well with the data found in the literature (Laiolo *et al.*, 2016; Morita *et al.*, 2019). The diminished signal magnitude is likely attributed to the decreased permeability resulting from the preceding hours’ rainfall, as evidenced by the elevated relative humidity observed in the site.

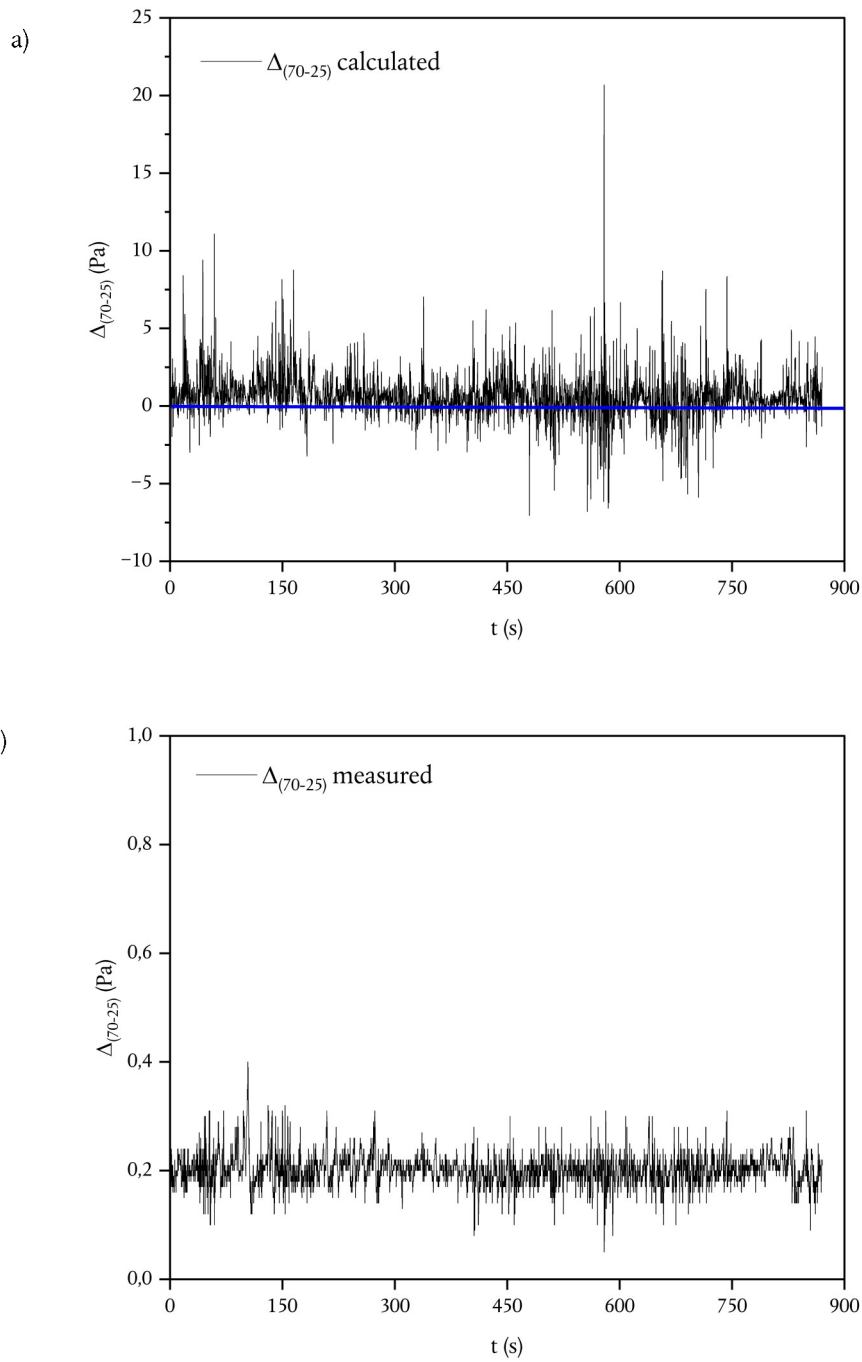


**Figure 7.7**— Field measurements conducted on September 10, 2024. The time series data includes  $\Delta_{(70-25)}$  calculated a), and  $\Delta_{(70-25)}$  measured b). The horizontal blue line in a) represents the hypothetical value 0 of  $\Delta_{(70-25)}$  calculated. The parameter  $\Delta_{(70-25)}$  measured remains almost constant at a value of around 0.2 Pa over a sequence lasting approximately 900 seconds. For a detailed explanation, please refer to the accompanying text.



The data pertaining to parameter  $\Delta_{(D-S)}^M$  plausibly signifies the real trend of natural degassing associated with volcano-tectonic activity at the specific investigated site.

The co-occurrence of the  $\Delta_{(D-S)}^M$  and  $\Delta_{(D-S)}^C$  implies the influence of environmental phenomena on surface pressure values. It is evident that the dual system expounded in this chapter has the potential to yield insights into the quality of surface measurements and contribute to the comprehension of the frequency and way in which environmental phenomena impact the system.

Hence, it is feasible to assert that, despite its limited time span presented in this chapter, the differences in parameters  $\Delta_{(D-S)}^M$  and  $\Delta_{(D-S)}^C$  can effectively delineate the influence of pressure differentials resulting from sudden pressure fluctuations associated with wind actions.

The test results exemplify the substantial adaptability achievable through the FEA. A comparison of parameters  $\Delta_{(D-S)}^M$  and  $\Delta_{(D-S)}^C$  distinctly reveals the influence of wind action on surface measurements and its resultant impact on soil gas fluxes. While these experimental data are still embryonal, they undoubtedly necessitate further investigation and, however, promptly indicate the intricacy of

obtaining qualitatively realistic measurements in complex natural systems.

The ability to isolate natural degassing processes through continuous measurements as described in this chapter presents an opportunity for meticulous examination of the deep-seated mechanisms that give rise to such processes. Concurrently, the experimental apparatus affords the prospect of gaining a more comprehensive understanding of how non-diffusive effects linked to meteorological phenomena impact, and occasionally obscure or potentially amplify, natural processes originating from profound sources.

## CHAPTER 8

### CONCLUSIONS

---

The initial objective of this doctoral thesis was to develop and operate an apparatus with the capability to measure the pressure fluctuations inherent in natural degassing systems. It can be asserted that the first objective was to construct a cost-effective apparatus that could deliver performance on par with established methods in seismology, while also offering integration with traditional geochemical investigation methods.

A series of laboratory and field tests have systematically evaluated the performance of the experimental apparatus under study. The laboratory data has revealed the apparatus's pronounced sensitivity to induced pressure fluctuations resulting from controlled and consistent air or gas fluxes within the experimental setup. The system demonstrated to reach the steady – state in less than ten seconds, affording, thus, an enormous measurement versatility. Experimental apparatus's functional limits were defined through the verification of Darcy's law applicability to the studied system. The system's optimization is geared toward accommodating fluxes consistent with those encountered in seismogenic and low-enthalpy volcanic

environments. The system configuration allows for a constant sampling frequency of 0.2 seconds.

Laboratory data has conclusively shown the feasibility of constructing an experimental apparatus using cost-effective and, in some instances, recyclable materials. The pursuit of this objective, while also necessitated by the limited availability of financial resources for this doctoral project, creates the opportunity to expand the project concept comprehensively.

The positive results obtained from the laboratory tests have enabled to develop an improved version of the experimental apparatus tailored for field measurements. Subsequent experimental tests were conducted on both the field and laboratory experimental apparatuses, yielding congruent parameters and physical behaviors.

Upon conclusion of the scientific tests, the field apparatus was employed to gather field data. Despite the inability to reconcile field measurements with geochemical data, the system yielded the following findings:

- ✓ Confirmation of its high sensitivity in detecting soil – gas pressure fluctuations.
- ✓ Demonstration of its capacity to conduct measurements in environments with diminished permeability.

- ✓ Manifestation of its capability to differentiate pressure fluctuation cycles of varying periods.
- ✓ Emphasis on the significance of high measurement frequencies for detecting diverse degassing processes and atmospheric phenomena.

The outcomes acquired are deemed satisfactory and promising for the further advancement of the project concept. It is evident that the field measurement phases, briefly referenced in this doctoral thesis, necessitates implementation across diverse natural degassing environments. Based on the preliminary data from this doctoral thesis, it is evident that the experimental apparatus presents extensive potential applications, particularly in the realm of atmospheric physics applied to natural degassing processes. Further, the field analyses must be integrated with geochemical, seismological, and meteorological investigations to effectively interpret the acquired data and comprehend the underlying processes driving natural degassing. The elevated sampling frequencies employed by the experimental apparatus under study enable the observation of individual micro-cyclic events that would otherwise remain imperceptible using alternative investigative approaches.

Securing funding for further experimental apparatus development could facilitate the establishment of a network of

apparatuses for monitoring seismogenic environments. Additionally, employing more advanced electronic components could facilitate remote data acquisition.

It can be concluded that the main objectives of this doctoral thesis have been achieved. It is important to consider that the experimental apparatus presented in this doctoral thesis holds scientific implications across various scientific disciplinary fields, including geophysics, volcanology, geochemistry, soil physics, and atmospheric physics.

## REFERENCES

---

Alam, A. *et al.* (2020) 'Implication of Radon Monitoring for Earthquake Surveillance Using Statistical Techniques: A Case Study of Wenchuan Earthquake', *Geofluids*, 2020. Available at: <https://doi.org/10.1155/2020/2429165>.

Ali YalIm, H. *et al.* (2012) 'Determination of the relationship between radon anomalies and earthquakes in well waters on the Akşehir-Simav Fault System in Afyonkarahisar province, Turkey', *Journal of Environmental Radioactivity*, 110. Available at: <https://doi.org/10.1016/j.jenvrad.2012.01.015>.

Allard, P. *et al.* (1991) 'Eruptive and diffuse emissions of CO<sub>2</sub> from Mount Etna', *Nature*, 351(6325). Available at: <https://doi.org/10.1038/351387a0>.

Allard, P. *et al.* (2014) 'Steam and gas emission rate from La Soufriere volcano, Guadeloupe (Lesser Antilles): Implications for the magmatic supply during degassing unrest', *Chemical Geology*, 384. Available at: <https://doi.org/10.1016/j.chemgeo.2014.06.019>.

Altland, A. and von Delft, J. (2019) *Mathematics for Physicists, Mathematics for Physicists*. Available at: <https://doi.org/10.1017/9781108557917>.

Attanasio, A. and Maravalle, M. (2016) 'Some considerations between radon and earthquakes in the crater of L'Aquila', *Natural Hazards*, 81(3). Available at: <https://doi.org/10.1007/s11069-016-2169-4>.

Azzaro, R. *et al.* (2012) 'The volcano-tectonic map of Etna volcano, 1:100.000 scale: An integrated approach based on a morphotectonic analysis from high-resolution DEM constrained by geologic, active faulting and seismotectonic data', *Italian Journal of Geosciences*, 131(1). Available at: <https://doi.org/10.3301/IJG.2011.29>.

Baehr, A.L. and Hult, M.F. (1991) 'Evaluation of Unsaturated Zone Air Permeability Through Pneumatic Tests', *Water Resources Research*, 27(10). Available at: <https://doi.org/10.1029/91WR01655>.

Baehr, A.L. and Joss, C.J. (1995) 'An Updated Model of Induced Airflow in the Unsaturated Zone', *Water Resources Research*, 31(2). Available at: <https://doi.org/10.1029/94WR02423>.

Barkat, A. *et al.* (2017) 'Radon as an earthquake precursor in and around northern Pakistan: A case study', *Geochemical Journal*, 51(4). Available at: <https://doi.org/10.2343/geochemj.2.0473>.

Barreca, G. *et al.* (2014) 'Geodetic and geological evidence of active tectonics in south-western Sicily (Italy)', *Journal of Geodynamics*, 82. Available at: <https://doi.org/10.1016/j.jog.2014.03.004>.

Bear, J. (1972) *Dynamics of fluids in porous media*. New York: Dover Publications, Inc.

Boudoire, G. *et al.* (2017) 'New perspectives on volcano monitoring in a tropical environment: Continuous measurements of soil CO<sub>2</sub> flux at Piton de la Fournaise (La Réunion Island, France)', *Geophysical Research Letters*, 44(16). Available at: <https://doi.org/10.1002/2017GL074237>.

Branca, S. *et al.* (2008) 'Geological evolution of Mount Etna volcano (Italy) from earliest products until the first central volcanism (between 500 and 100 ka ago) inferred from geochronological and stratigraphic data', *International Journal of Earth Sciences*. Available at: <https://doi.org/10.1007/s00531-006-0152-0>.

Branca, S., Carbone, D. and Greco, F. (2003) 'Intrusive mechanism of the 2002 NE-Rift eruption at Mt. Etna (Italy) inferred through continuous microgravity data and volcanological evidences', *Geophysical Research Letters*, 30(20). Available at: <https://doi.org/10.1029/2003GL018250>.

Bruno, N. *et al.* (2001) 'Degassing of SO<sub>2</sub> and CO<sub>2</sub> at Mount Etna (Sicily) as an indicator of pre-eruptive ascent and shallow emplacement of magma', *Journal of Volcanology and Geothermal Research*, 110(1–2). Available at: [https://doi.org/10.1016/S0377-0273\(01\)00201-3](https://doi.org/10.1016/S0377-0273(01)00201-3).

Buttitta, D. *et al.* (2020) 'Continental degassing of helium in an active tectonic setting (northern Italy): the role of seismicity', *Scientific Reports*, 10(1). Available at: <https://doi.org/10.1038/s41598-019-55678-7>.



Camarda, M. *et al.* (2007) 'Evaluation of carbon isotope fractionation of soil CO<sub>2</sub> under an advective-diffusive regimen: A tool for computing the isotopic composition of unfractionated deep source', *Geochimica et Cosmochimica Acta*, 71(12). Available at: <https://doi.org/10.1016/j.gca.2007.04.002>.

Camarda, M., Gurrieri, S. and Valenza, M. (2006) 'CO<sub>2</sub> flux measurements in volcanic areas using the dynamic concentration method: Influence of soil permeability', *Journal of Geophysical Research: Solid Earth*, 111(5). Available at: <https://doi.org/10.1029/2005JB003898>.

Camarda, Marco, Gurrieri, S. and Valenza, M. (2006) 'In situ permeability measurements based on a radial gas advection model: Relationships between soil permeability and diffuse CO<sub>2</sub> degassing in volcanic areas', *Pure and Applied Geophysics*, 163(4). Available at: <https://doi.org/10.1007/s00024-006-0045-y>.

Caracausi, A. *et al.* (2022) 'Earthquakes control the impulsive nature of crustal helium degassing to the atmosphere', *Communications Earth and Environment*, 3(1). Available at: <https://doi.org/10.1038/s43247-022-00549-9>.

Carapezza, M.L. *et al.* (2011) 'Diffuse CO<sub>2</sub> soil degassing and CO<sub>2</sub> and H<sub>2</sub>S concentrations in air and related hazards at Vulcano Island (Aeolian arc, Italy)', *Journal of Volcanology and Geothermal Research*, 207(3–4). Available at: <https://doi.org/10.1016/j.jvolgeores.2011.06.010>.

Carapezza, M.L. *et al.* (2023) 'Health impact of natural gas emission at Cava dei Selci residential zone (metropolitan city of Rome, Italy)', *Environmental Geochemistry and Health*, 45(3). Available at: <https://doi.org/10.1007/s10653-022-01244-6>.

Cardellini, C. *et al.* (2017) 'Monitoring diffuse volcanic degassing during volcanic unrests: The case of Campi Flegrei (Italy)', *Scientific Reports*, 7(1). Available at: <https://doi.org/10.1038/s41598-017-06941-2>.

Chen, Z. *et al.* (2019) 'Evidence of Multiple Sources of Soil Gas in the Tangshan Fault Zone, North China', *Geofluids*, 2019. Available at: <https://doi.org/10.1155/2019/1945450>.

Chicco, J.M., Giammanco, S. and Mandrone, G. (2020) 'Multidisciplinary study of the "salinelle" of paternò mud volcanoes:

Characteristics of the fluids and possible correlations with the activity of mt. etna', *Annals of Geophysics*, 63. Available at: <https://doi.org/10.4401/ag-8523>.

Chiodini, G. *et al.* (1998) 'Soil CO<sub>2</sub> flux measurements in volcanic and geothermal areas', *Applied Geochemistry*, 13(5). Available at: [https://doi.org/10.1016/S0883-2927\(97\)00076-0](https://doi.org/10.1016/S0883-2927(97)00076-0).

Chiodini, G. *et al.* (2004) 'Carbon dioxide Earth degassing and seismogenesis in central and southern Italy', *Geophysical Research Letters*, 31(7). Available at: <https://doi.org/10.1029/2004GL019480>.

Chiodini, Giovanni *et al.* (2004) 'Fumarolic and diffuse soil degassing west of Mount Epomeo, Ischia, Italy', *Journal of Volcanology and Geothermal Research*, 133(1–4). Available at: [https://doi.org/10.1016/S0377-0273\(03\)00403-7](https://doi.org/10.1016/S0377-0273(03)00403-7).

Chiodini, G. *et al.* (2020) 'Correlation between tectonic CO<sub>2</sub> Earth degassing and seismicity is revealed by a 10-year record in the Apennines, Italy', *Science Advances*, 6(35). Available at: <https://doi.org/10.1126/sciadv.abc2938>.

Choi, J.W. and Smith, J.A. (2005) 'Geoenvironmental factors affecting organic vapor advection and diffusion fluxes from the unsaturated zone to the atmosphere under natural conditions', *Environmental Engineering Science*, 22(1). Available at: <https://doi.org/10.1089/ees.2005.22.95>.

Cicerone, R.D., Ebel, J.E. and Britton, J. (2009) 'A systematic compilation of earthquake precursors', *Tectonophysics*. Available at: <https://doi.org/10.1016/j.tecto.2009.06.008>.

Collignon, M. *et al.* (2021) 'Carbon dioxide diffuse emission at the Tolhuaca hydrothermal system (Chile) controlled by tectonics and topography', *Journal of Volcanology and Geothermal Research*, 417. Available at: <https://doi.org/10.1016/j.jvolgeores.2021.107316>.

Conti, L., Picozza, P. and Sotgiu, A. (2021) 'A Critical Review of Ground Based Observations of Earthquake Precursors', *Frontiers in Earth Science*. Available at: <https://doi.org/10.3389/feart.2021.676766>.

Cristi, G.M. *et al.* (2010) 'Predicting the impact of lava flows at Mount Etna, Italy', *Journal of Geophysical Research: Solid Earth*, 115(4). Available at: <https://doi.org/10.1029/2009JB006431>.

Cui, Y. *et al.* (2024) 'CO Emissions Associated with Three Major Earthquakes Occurring in Diverse Tectonic Environments', *Remote Sensing*, 16(3). Available at: <https://doi.org/10.3390/rs16030480>.

Druhan, J. and Tournassat, C. (2019) *Reactive Transport in Natural and Engineered Systems, Reactive Transport in Natural and Engineered Systems*. Edited by J. Druhan and C. Tournassat. Available at: <https://doi.org/10.1515/9781501512001>.

Falta, R.W. (1996) 'Program for analyzing transient and steady-state soil gas pump tests', *Ground Water*, 34(4). Available at: <https://doi.org/10.1111/j.1745-6584.1996.tb02064.x>.

Favara, R. *et al.* (2001) 'Preliminary estimate of CO<sub>2</sub> output from Pantelleria Island volcano (Sicily, Italy): Evidence of active mantle degassing', *Applied Geochemistry*, 16(7–8). Available at: [https://doi.org/10.1016/S0883-2927\(00\)00055-X](https://doi.org/10.1016/S0883-2927(00)00055-X).

Finizola, A. *et al.* (2002) 'Fluid circulation at Stromboli volcano (Aeolian Islands, Italy) from self-potential and CO<sub>2</sub> surveys', *Journal of Volcanology and Geothermal Research*, 116(1–2). Available at: [https://doi.org/10.1016/S0377-0273\(01\)00327-4](https://doi.org/10.1016/S0377-0273(01)00327-4).

Freund, F. *et al.* (2021) 'Earthquake precursors in the light of peroxy defects theory: Critical review of systematic observations', *European Physical Journal: Special Topics*. Available at: <https://doi.org/10.1140/epjst/e2020-000243-x>.

Fron dini, F. *et al.* (2019) 'Measuring and interpreting CO<sub>2</sub> fluxes at regional scale: The case of the Apennines, Italy', *Journal of the Geological Society*, 176(2). Available at: <https://doi.org/10.1144/jgs2017-169>.

Fu, C.C. *et al.* (2017) 'Preseismic anomalies in soil-gas radon associated with 2016 M6.6 Meinong earthquake, Southern Taiwan', *Terrestrial, Atmospheric and Oceanic Sciences*, 28(5). Available at: <https://doi.org/10.3319/TAO.2017.03.22.01>.

Geersen, J. *et al.* (2016) 'Fault zone controlled seafloor methane seepage in the rupture area of the 2010 Maule earthquake, Central Chile', *Geochemistry, Geophysics, Geosystems*, 17(11). Available at: <https://doi.org/10.1002/2016GC006498>.

Gerlach, T.M. *et al.* (2001) 'Soil efflux and total emission rates of magmatic CO<sub>2</sub> at the horseshoe lake tree kill, mammoth mountain,

California, 1995-1999', *Chemical Geology*, 177(1-2). Available at: [https://doi.org/10.1016/S0009-2541\(00\)00385-5](https://doi.org/10.1016/S0009-2541(00)00385-5).

Ghosh, D., Deb, A. and Sengupta, R. (2009) 'Anomalous radon emission as precursor of earthquake', *Journal of Applied Geophysics*. Available at: <https://doi.org/10.1016/j.jappgeo.2009.06.001>.

Giammanco, S. *et al.* (2007) 'Focused and diffuse effluxes of CO<sub>2</sub> from mud volcanoes and mofettes south of Mt. Etna (Italy)', *Journal of Volcanology and Geothermal Research*, 165(1-2). Available at: <https://doi.org/10.1016/j.jvolgeores.2007.04.010>.

Giammanco, S. *et al.* (2010) 'Statistical analysis reveals spatial and temporal anomalies of soil CO<sub>2</sub> efflux on Mount Etna volcano (Italy)', *Journal of Volcanology and Geothermal Research*, 194(1-3). Available at: <https://doi.org/10.1016/j.jvolgeores.2010.04.006>.

Giammanco, S. *et al.* (2013) 'Evidence for a recent change in the shallow plumbing system of Mt. Etna (Italy): Gas geochemistry and structural data during 2001-2005', *Journal of Volcanology and Geothermal Research*, 251. Available at: <https://doi.org/10.1016/j.jvolgeores.2012.06.001>.

Giammanco, S., Bonfanti, P. and Neri, M. (2023) 'Radon on Mt. Etna (Italy): a useful tracer of geodynamic processes and a potential health hazard to populations', *Frontiers in Earth Science*. Available at: <https://doi.org/10.3389/feart.2023.1176051>.

Giammanco, S., Gurrieri, S. and Valenza, M. (1997) 'Soil CO<sub>2</sub> degassing along tectonic structures of Mount Etna (Sicily): The Pernicana fault', *Applied Geochemistry*, 12(4). Available at: [https://doi.org/10.1016/S0883-2927\(97\)00011-5](https://doi.org/10.1016/S0883-2927(97)00011-5).

Giammanco, S., Gurrieri, S. and Valenza, M. (1998) 'Anomalous soil CO<sub>2</sub> degassing in relation to faults and eruptive fissures on Mount Etna (Sicily, Italy)', *Bulletin of Volcanology*, 60(4). Available at: <https://doi.org/10.1007/s004450050231>.

Giammanco, S., Gurrieri, S. and Valenza, M. (1999) 'Geochemical investigations applied to active fault detection in a volcanic area: The North-East Rift on Mt. Etna (Sicily, Italy)', *Geophysical Research Letters*, 26(13). Available at: <https://doi.org/10.1029/1999GL900396>.

Groppelli, G. and Norini, G. (2011) 'Geology and tectonics of the southwestern boundary of the unstable sector of Mt. Etna (Italy)',

*Journal of Volcanology and Geothermal Research*, 208(1–2). Available at: <https://doi.org/10.1016/j.jvolgeores.2011.08.006>.

Gudjónsdóttir, S.R. *et al.* (2020) ‘Gas emissions and crustal deformation from the Krýsuvík high temperature geothermal system, Iceland’, *Journal of Volcanology and Geothermal Research*, 391. Available at: <https://doi.org/10.1016/j.jvolgeores.2018.04.007>.

De Guidi, G. *et al.* (2015) ‘Geological, seismological and geodetic evidence of active thrusting and folding south of Mt. Etna (eastern Sicily): Reevaluation of “seismic efficiency” of the Sicilian Basal Thrust’, *Journal of Geodynamics*, 90. Available at: <https://doi.org/10.1016/j.jog.2015.06.001>.

Gurrieri, S. *et al.* (2023) ‘Monitoring CO<sub>2</sub> Hazards of Volcanic Origin: A Case Study at the Island of Vulcano (Italy) during 2021–2022’, *Geosciences (Switzerland)*, 13(9). Available at: <https://doi.org/10.3390/geosciences13090266>.

Haider, T. *et al.* (2021) ‘Identification of radon anomalies induced by earthquake activity using intelligent systems’, *Journal of Geochemical Exploration*, 222. Available at: <https://doi.org/10.1016/j.gexplo.2020.106709>.

Hauksson, E. and Goddard, J.G. (1981) ‘Radon earthquake precursor studies in Iceland.’, *Journal of Geophysical Research*, 86(B8). Available at: <https://doi.org/10.1029/JB086iB08p07037>.

Hirsch, A.I., Trumbore, S.E. and Goulden, M.L. (2004) ‘The surface CO<sub>2</sub> gradient and pore-space storage flux in a high-porosity litter layer’, *Tellus, Series B: Chemical and Physical Meteorology*, 56(4). Available at: <https://doi.org/10.1111/j.1600-0889.2004.00113.x>.

Ho, C.K. and Webb, S.W. (2010) *Gas Transport in Porous Media*. Springer.

Holzer, L. *et al.* (2023) ‘Review of Theories and a New Classification of Tortuosity Types’, in *Springer Series in Materials Science*. Available at: [https://doi.org/10.1007/978-3-031-30477-4\\_2](https://doi.org/10.1007/978-3-031-30477-4_2).

Huang, P. *et al.* (2024) ‘Earthquake precursors: A review of key factors influencing radon concentration’, *Journal of Environmental Radioactivity*. Available at: <https://doi.org/10.1016/j.jenvrad.2023.107310>.

İçhedef, M. *et al.* (2020) 'In soil radon anomalies and volcanic activity on Mt. Etna (Italy)', *Journal of Environmental Radioactivity*, 218. Available at: <https://doi.org/10.1016/j.jenvrad.2020.106267>.

Inguaggiato, S. *et al.* (2023) 'Sulfur origin and flux variations in fumarolic fluids of Vulcano Island, Italy', *Frontiers in Earth Science*, 11. Available at: <https://doi.org/10.3389/feart.2023.1197796>.

Iwata, D. *et al.* (2018) 'Non-parametric detection of atmospheric radon concentration anomalies related to earthquakes', *Scientific Reports*, 8(1). Available at: <https://doi.org/10.1038/s41598-018-31341-5>.

Jain, S.R., Paradkar, B.S. and Chitre, S.M. (2023) *A Primer on Fluid Mechanics with Applications, A Primer on Fluid Mechanics with Applications*. Available at: <https://doi.org/10.1007/978-3-031-20487-6>.

Jiang, J., Gu, K., *et al.* (2023) 'Effect of Barometric Pressure Fluctuations on Gas Transport over Soil Surfaces', *Land*, 12(1). Available at: <https://doi.org/10.3390/land12010161>.

Jiang, J., Hu, J., *et al.* (2023) 'Effect of near-surface winds on the measurement of forest soil CO<sub>2</sub> fluxes using closed air chambers', *Frontiers in Ecology and Evolution*, 11. Available at: <https://doi.org/10.3389/fevo.2023.1163704>.

Jiang, Y.H. *et al.* (2023) 'STATUS OF RESEARCH AND OBSERVATION ON UNDERGROUND FLUID HYDROGEN IN SEISMIC FAULT ZONES IN CHINA', *Dizhen Dizhi*, 45(3). Available at: <https://doi.org/10.3969/j.issn.0253-4967.2023.03.002>.

Kambe, T. (2007) *Elementary fluid mechanics, Elementary Fluid Mechanics*. Available at: <https://doi.org/10.1142/5895>.

Kim, J.W. *et al.* (2018) 'Investigation of the relationship between earthquakes and indoor radon concentrations at a building in Gyeongju, Korea', *Nuclear Engineering and Technology*, 50(3). Available at: <https://doi.org/10.1016/j.net.2017.12.010>.

Knappett, J.A. and Craig, R.F. (2012) *Craig's Soil Mechanics, Eighth edition, Craig's Soil Mechanics, Eighth Edition*. Available at: <https://doi.org/10.1201/b12841>.

Kyriakopoulos, G.K. (2017) 'Natural degassing of carbon dioxide and hydrogen sulphide and its environmental impact at milos island,

greece', *Bulletin of the Geological Society of Greece*, 43(5). Available at: <https://doi.org/10.12681/bgsg.11636>.

Laemmel, T. *et al.* (2019) 'From above the forest into the soil – How wind affects soil gas transport through air pressure fluctuations', *Agricultural and Forest Meteorology*, 265. Available at: <https://doi.org/10.1016/j.agrformet.2018.11.007>.

Laiolo, M. *et al.* (2016) 'The effects of environmental parameters on diffuse degassing at Stromboli volcano: Insights from joint monitoring of soil CO<sub>2</sub> flux and radon activity', *Journal of Volcanology and Geothermal Research*, 315. Available at: <https://doi.org/10.1016/j.jvolgeores.2016.02.004>.

Lavecchia, G. *et al.* (2007) 'Active thrusting as a possible seismogenic source in Sicily (Southern Italy): Some insights from integrated structural-kinematic and seismological data', *Tectonophysics*, 445(3–4). Available at: <https://doi.org/10.1016/j.tecto.2007.07.007>.

Levintal, E. *et al.* (2020) 'The role of atmospheric conditions in CO<sub>2</sub> and radon emissions from an abandoned water well', *Science of the Total Environment*, 722. Available at: <https://doi.org/10.1016/j.scitotenv.2020.137857>.

Lewicki, J.L. and Hilley, G.E. (2014) 'Multi-scale observations of the variability of magmatic CO<sub>2</sub> emissions, Mammoth Mountain, CA, USA', *Journal of Volcanology and Geothermal Research*, 284. Available at: <https://doi.org/10.1016/j.jvolgeores.2014.07.011>.

Li, J.Y. *et al.* (2023) 'Geochemical Characteristics of Soil Hydrogen Gas of the Main Seismogenic Structures of Songliao Basin', *Earthquake*, 43(1). Available at: <https://doi.org/10.12196/j.issn.1000.3274.2023.01.012>.

Li Vigni, L. *et al.* (2022) 'Duvalo "Volcano" (North Macedonia): A Purely Tectonic-Related CO<sub>2</sub> Degassing System', *Geochemistry, Geophysics, Geosystems*, 23(4). Available at: <https://doi.org/10.1029/2021GC010198>.

Liu, W. *et al.* (2023) 'Hydrothermal He and CO<sub>2</sub> degassing from a Y-shaped active fault system in eastern Tibetan Plateau with implications for seismogenic processes', *Journal of Hydrology*, 620. Available at: <https://doi.org/10.1016/j.jhydrol.2023.129482>.

Madonia, P. *et al.* (2022) 'Atmospheric CO<sub>2</sub> Concentrations in Caves Protected as Nature Reserves and Related Gas Hazard', *Atmosphere*, 13(11). Available at: <https://doi.org/10.3390/atmos13111760>.

Maier, M., Mayer, S. and Laemmel, T. (2019) 'Rain and wind affect chamber measurements', *Agricultural and Forest Meteorology*, 279. Available at: <https://doi.org/10.1016/j.agrformet.2019.107754>.

Di Martino, R.M.R. *et al.* (2016) 'Asynchronous changes of CO<sub>2</sub>, H<sub>2</sub>, and He concentrations in soil gases: A theoretical model and experimental results', *Journal of Geophysical Research: Solid Earth*, 121(3). Available at: <https://doi.org/10.1002/2015JB012600>.

Di Martino, R.M.R. and Gurrieri, S. (2023) 'Quantification of the Volcanic Carbon Dioxide in the Air of Vulcano Porto by Stable Isotope Surveys', *Journal of Geophysical Research: Atmospheres*, 128(15). Available at: <https://doi.org/10.1029/2022JD037706>.

Massman, W.J. *et al.* (1997) 'A model investigation of turbulence-driven pressure-pumping effects on the rate of diffusion of CO<sub>2</sub>, N<sub>2</sub>O, and CH<sub>4</sub> through layered snowpacks', *Journal of Geophysical Research Atmospheres*, 102(15). Available at: <https://doi.org/10.1029/97jd00844>.

Massmann, J. and Farrier, D.F. (1992) 'Effects of atmospheric pressures on gas transport in the vadose zone', *Water Resources Research*, 28(3). Available at: <https://doi.org/10.1029/91WR02766>.

Maucourant, S. *et al.* (2014) 'Geophysical and geochemical methods applied to investigate fissure-related hydrothermal systems on the summit area of Mt. Etna volcano (Italy)', *Journal of Volcanology and Geothermal Research*, 280. Available at: <https://doi.org/10.1016/j.jvolgeores.2014.05.014>.

Meng, Q. and Zhang, Y. (2021) 'Discovery of spatial-temporal causal interactions between thermal and methane anomalies associated with the Wenchuan earthquake', *European Physical Journal: Special Topics*, 230(1). Available at: <https://doi.org/10.1140/epjst/e2020-000252-9>.

Mohr, M. *et al.* (2016) 'Analysis of air pressure fluctuations and topsoil gas concentrations within a scots pine forest', *Atmosphere*, 7(10). Available at: <https://doi.org/10.3390/atmos7100125>.



Monaco, C. *et al.* (2005) 'Tectonic control on the eruptive dynamics at Mt. Etna Volcano (Sicily) during the 2001 and 2002-2003 eruptions', *Journal of Volcanology and Geothermal Research*, 144(1-4 SPEC. ISS.). Available at: <https://doi.org/10.1016/j.jvolgeores.2004.11.024>.

Morita, M. *et al.* (2019) 'Continuous monitoring of soil CO<sub>2</sub> flux at Aso volcano, Japan: the influence of environmental parameters on diffuse degassing', *Earth, Planets and Space*, 71(1). Available at: <https://doi.org/10.1186/s40623-018-0980-8>.

Muto, J. *et al.* (2021) 'Preseismic atmospheric radon anomaly associated with 2018 Northern Osaka earthquake', *Scientific Reports*, 11(1). Available at: <https://doi.org/10.1038/s41598-021-86777-z>.

Neeper, D.A. (2003) 'Harmonic analysis of flow in open boreholes due to barometric pressure cycles', *Journal of Contaminant Hydrology*, 60(3-4). Available at: [https://doi.org/10.1016/S0169-7722\(02\)00086-4](https://doi.org/10.1016/S0169-7722(02)00086-4).

Neri, M., Giammanco, S., *et al.* (2011) 'Spatial distribution of soil radon as a tool to recognize active faulting on an active volcano: The example of Mt. Etna (Italy)', *Journal of Environmental Radioactivity*, 102(9). Available at: <https://doi.org/10.1016/j.jenvrad.2011.05.002>.

Neri, M., Acocella, V., *et al.* (2011) 'Structural analysis of the eruptive fissures at Mount Etna (Italy)', *Annals of Geophysics*, 54(5). Available at: <https://doi.org/10.4401/ag-5332>.

Neri, M. *et al.* (2016) 'Soil radon measurements as a potential tracer of tectonic and volcanic activity', *Scientific Reports*, 6. Available at: <https://doi.org/10.1038/srep24581>.

Neri, M., Giammanco, S. and Leonardi, A. (2019) 'Preliminary indoor radon measurements near faults crossing urban areas of Mt. Etna volcano (Italy)', *Frontiers in Public Health*, 7(APR). Available at: <https://doi.org/10.3389/fpubh.2019.00105>.

Pezzo, G. *et al.* (2020) 'Flank sliding: A valve and a sentinel for paroxysmal eruptions and magma ascent at Mount Etna, Italy', *Geology*, 48(11). Available at: <https://doi.org/10.1130/G47656.1>.

Planinić, J., Radolić, V. and Vuković, B. (2004) 'Radon as an earthquake precursor', *Nuclear Instruments and Methods in Physics Research, Section A: Accelerators, Spectrometers, Detectors and*

*Associated Equipment*, 530(3). Available at: <https://doi.org/10.1016/j.nima.2004.04.209>.

Qiu, Q.W. *et al.* (2021) 'A new method and apparatus for measuring in situ air permeability of unsaturated soil', *Canadian Geotechnical Journal*, 58(4). Available at: <https://doi.org/10.1139/cgj-2019-0733>.

Ristuccia, G.M., Bonfanti, P. and Giammanco, S. (2021) 'A hydrogeochemical approach to the characterization of low-enthalpy geothermal systems: the Scordia – Lentini graben (Sicily, Italy)', *Annals of Geophysics*, 64(4). Available at: <https://doi.org/10.4401/AG-8536>.

Rouf, M.A. *et al.* (2016) 'Gas permeability of partially hydrated geosynthetic clay liner under two stress conditions', *Environmental Geotechnics*, 3(5). Available at: <https://doi.org/10.1680/envgeo.14.00009>.

Sano, Y. *et al.* (1998) 'Helium degassing related to the Kobe earthquake', *Chemical Geology*, 150(1–2). Available at: [https://doi.org/10.1016/S0009-2541\(98\)00055-2](https://doi.org/10.1016/S0009-2541(98)00055-2).

Scarfi, L. *et al.* (2023) 'Observing Etna volcano dynamics through seismic and deformation patterns', *Scientific Reports*, 13(1). Available at: <https://doi.org/10.1038/s41598-023-39639-9>.

Semenov, R.M., Lopatin, M.N. and Chechelnitsky, V. V. (2020) 'The study of dissolved helium and radon concentrations in groundwaters of southern Pribaikalie in connection with seismic processes', *Geodynamics and Tectonophysics*, 11(1). Available at: <https://doi.org/10.5800/GT-2020-11-1-0463>.

Sergio Calabrese *et al.* (2021a) 'Annex 1 to: Passive Degassing at Nyiragongo (D.R. Congo) and Etna (Italy) Volcanoes.', *Annals of Geophysics*, 57. Available at: <https://doi.org/10.4401/ag-6757>.

Sergio Calabrese *et al.* (2021b) 'Annex 2 to: Passive Degassing at Nyiragongo (D.R. Congo) and Etna (Italy) Volcanoes.', *Annals of Geophysics*, 57. Available at: <https://doi.org/10.4401/ag-6758>.

Singh, R.P. *et al.* (2010) 'Satellite detection of carbon monoxide emission prior to the Gujarat earthquake of 26 January 2001', *Applied Geochemistry*, 25(4). Available at: <https://doi.org/10.1016/j.apgeochem.2010.01.014>.

Sortino, F. *et al.* (2022) 'Stress-induced changes in hydrothermal gas discharges along active faults near Mt. Etna volcano (Sicily, Italy)', *Tectonophysics*, 836. Available at: <https://doi.org/10.1016/j.tecto.2022.229388>.

Stauffer, P.H. *et al.* (2019) 'Evidence for High Rates of Gas Transport in the Deep Subsurface', *Geophysical Research Letters*, 46(7). Available at: <https://doi.org/10.1029/2019GL082394>.

Stylianos, S. and Alexandra, I. (2023) 'Time-series analysis of radon monitoring in soil gas in association with earthquakes in Stivos faulting, at Lagadas basin, North Greece', *Journal of Radioanalytical and Nuclear Chemistry*, 332(11). Available at: <https://doi.org/10.1007/s10967-023-09170-2>.

Sun, Y. *et al.* (2021) 'Soil Degassing From the Xianshuihe–Xiaojiang Fault System at the Eastern Boundary of the Chuan–Dian Rhombic Block, Southwest China', *Frontiers in Earth Science*, 9. Available at: <https://doi.org/10.3389/feart.2021.635178>.

Terray, L. *et al.* (2020) 'Radon Activity in Volcanic Gases of Mt. Etna by Passive Dosimetry', *Journal of Geophysical Research: Solid Earth*, 125(9). Available at: <https://doi.org/10.1029/2019JB019149>.

Thomas, D. (1988) 'Geochemical precursors to seismic activity', *Pure and Applied Geophysics PAGEOPH*, 126(2–4). Available at: <https://doi.org/10.1007/BF00878998>.

Turk, L.J. (1975) 'Diurnal fluctuations of water tables induced by atmospheric pressure changes', *Journal of Hydrology*, 26(1–2). Available at: [https://doi.org/10.1016/0022-1694\(75\)90121-3](https://doi.org/10.1016/0022-1694(75)90121-3).

Umeda, K., Asamori, K. and Kusano, T. (2013) 'Release of mantle and crustal helium from a fault following an inland earthquake', *Applied Geochemistry*, 37. Available at: <https://doi.org/10.1016/j.apgeochem.2013.07.018>.

Urlaub, M. *et al.* (2018) 'Gravitational collapse of Mount Etna's southeastern flank', *Science Advances*, 4(10). Available at: <https://doi.org/10.1126/sciadv.aat9700>.

Vaupotič, J., Žvab, P. and Giammanco, S. (2010) 'Radon in outdoor air in the Mt. Etna area, Italy', *Nukleonika*, 55(4).

Vimercati, L. *et al.* (2021) 'Relationships among indoor radon, earthquake magnitude data and lung cancer risks in a residential

building of an apulian town (Southern italy)', *Atmosphere*, 12(10). Available at: <https://doi.org/10.3390/atmos12101342>.

Viveiros, F. *et al.* (2008) 'Environmental influences on soil CO<sub>2</sub> degassing at Furnas and Fogo volcanoes (São Miguel Island, Azores archipelago)', *Journal of Volcanology and Geothermal Research*, 177(4). Available at: <https://doi.org/10.1016/j.jvolgeores.2008.07.005>.

Wang, H. (2017) *Mathematics for Physicists, Mathematics for Physicists*. Available at: <https://doi.org/10.1142/10191>.

Wang, J. *et al.* (2013) 'Anomalies of temperature increase and methane release before Lushan earthquake(MS 7.0)', *Earth Science Frontiers*, 20(6).

Wang, X. *et al.* (2023) 'Feasibility exploration of methane seismic monitoring in local areas of Sichuan and Yunnan : Taking the M6.0 earthquake in Luxian, Sichuan in september 2021 as an example', *National Remote Sensing Bulletin*, 27(7). Available at: <https://doi.org/10.11834/jrs.20232301>.

Weltner, K. *et al.* (2023) *Mathematics for Physicists and Engineers, Mathematics for Physicists and Engineers*. Available at: <https://doi.org/10.1007/978-3-662-66068-3>.

Woith, H. (2015) 'Radon earthquake precursor: A short review', *European Physical Journal: Special Topics*. Available at: <https://doi.org/10.1140/epjst/e2015-02395-9>.

Wu, Y.S. and Pruess, K. (2000) 'Integral solutions for transient fluid flow through a porous medium with pressure-dependent permeability', in *International Journal of Rock Mechanics and Mining Sciences*. Available at: [https://doi.org/10.1016/s1365-1609\(99\)00091-x](https://doi.org/10.1016/s1365-1609(99)00091-x).

You, K. and Zhan, H. (2012) 'Can atmospheric pressure and water table fluctuations be neglected in soil vapor extraction?', *Advances in Water Resources*, 35. Available at: <https://doi.org/10.1016/j.advwatres.2011.10.008>.

Zgonnik, V. (2020) 'The occurrence and geoscience of natural hydrogen: A comprehensive review', *Earth-Science Reviews*. Available at: <https://doi.org/10.1016/j.earscirev.2020.103140>.

Zhang, L. *et al.* (2020) 'Continuous monitoring of hydrogen and oxygen stable isotopes in a hot spring: Significance for distant

earthquakes', *Applied Geochemistry*, 112. Available at: <https://doi.org/10.1016/j.apgeochem.2019.104488>.

Zhang, M. *et al.* (2024) 'Hydrothermal Degassing Through the Karakoram Fault, Western Tibet: Insights Into Active Deformation Driven by Continental Strike-Slip Faulting', *Geophysical Research Letters*, 51(4). Available at: <https://doi.org/10.1029/2023GL106647>.

Zhong, J. *et al.* (2021) 'Dynamic characteristics of fault hydrogen concentration in Aksu and its earthquake reflecting efficiency', *Acta Seismologica Sinica*, 43(5). Available at: <https://doi.org/10.11939/jass.20210007>.

Zimmerman, R.W. and Paluszny, A. (2023) *Fluid Flow in Fractured Rocks*. Wiley.